Soft Colloids from p(NIPAm-co-AAc): Packing Dynamics and Structure

Thesis advisor

David A Weitz

Author

Melaku Muluneh

Soft Colloids from p(NIPAm-co-AAc): Packing dynamics and structure

Abstract

Traditionally, the experimental model of choice for studying the structure and dynamics of glasses or crystals are hard-sphere colloids. An analogy with molecular or atomic materials is often drawn, in which each colloidal particle represents an atom or a molecule. Making the individual particles deformable allows an even wider range of phenomena to be observed. In this thesis, I report the three-dimensional confocal microscopic study of the structure and dynamics of aqueous suspensions of fluorescently labeled poly(N-Isopropylacrylamide)-co-(Acrylic Acid), or p(NIPAm-co-AAc), microgel particles of hydrodynamic diameter 1.0 - 1.5 μm. Image analysis techniques and particle tracking algorithms are used to quantify the particle dynamics and the suspension structure.

The phase behavior of the suspensions is dependent on a number of factors including pH, temperature, and concentration. By adjusting the pH, the interactions between the microgel particles can be tuned from purely repulsive near neutral pH, to weakly attractive at low pH. At low pH and low concentration, dynamic arrest results mainly from crystallization driven by the attraction between particles; crystal nucleation occurs homogeneously throughout the sample. The dynamics is nucleation

limited where fast crystallization follows a delay time. At low pH and high concentration, relaxation of the suspension is constrained and it evolves only slightly to form a disordered solid. At neutral pH, the dynamics are a function of the particle number concentration only; a high concentration leads to the formation of a disordered soft glassy solid.

Additionally, the three-dimensional image stacks are studied to determine crystal structure by calculating pair correlation functions, $g(r)$, bond order parameters, and structure factors, $s(q)$. The results show that crystal structure is independent of concentration, charge, size, and stiffness of particles remaining FCC under all conditions. At low concentrations and low pH, the structures formed are polycrystalline solids. Moreover, the ability of the particles to compress enables the suspensions to maintain their crystal structure when subjected to external stress.

The results help us better understand the relationship between dynamics and structure in soft colloidal suspensions, enhance our ability to use the colloids to model materials, and improve applications of the colloids in industrial products.

Contents

Citations to Previously Published Work

Chapters 5 and 6 have appeared in the following two papers respectively:

"Direct visulaization of pH-dependent evolution of structure and dynamics in microgel suspensions", M Muluneh, J Sprakel, H M Wyss, J Mattsson and D A Weitz
J. Phys.:Condens. Matter **23**, 505101(2011)

"Direct visualization of three-dimensional crystallization behavior in microgels", Melaku Muluneh and David A. Weitz
Phy. Rev. E. **85**, 02145 (2012)

Acknowledgments

I thank my supervisor, Professor David Weitz, for the opportunity to work in his lab and for fully supporting my studies. I am thankful for the support of the staff and faculty of the Physics department of Harvard University. I especially thank Sheila Ferguson for her assistance when requiring official letters. Special regard to my mother, Zenebech Ashenafi, for her unconditional care, concern, and devotion. I also thank my family and friends for their encouragement, advice, and companionship during my graduate studies.

Chapter 1

Introduction

1.1 Colloids

Colloidal particles are defined in broad terms as particles that are big enough to be seen under an ordinary optical microscope but are small enough to execute random motion in solution, called Brownian motion. Their size ranges between 1 nm and 10 μm in diameter. They have also been termed as "big molecules" since they exhibit thermal fluctuations analogous to the motion of molecules. Pollen grains in water were observed by Robert Brown to move randomly; these are a good example of colloidal particles.

Colloidal solutions exhibit dynamical and structural characterstics that are a function of particle concentration. They undergo liquid-solid transitions, where the transitions are defined by the dynamics of the individual particles. A colloidal liquid is characterized by unconstrained movement of the particles. A typical self diffusion time for colloidal particles in liquid is in the order of mili-seconds. By contrast,

particles in a solidified colloidal system show no movement except perhaps vibration.

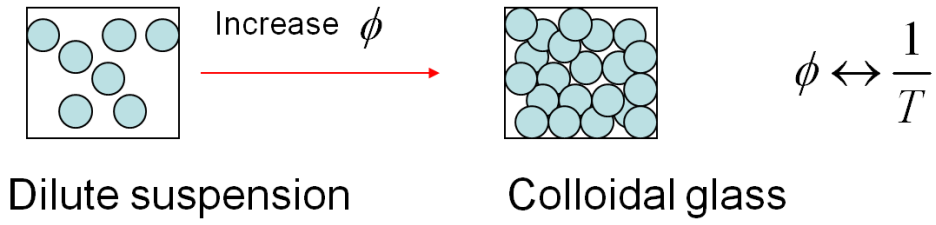

Figure 1.1: Colloidal glass formation

In atomic and molecular systems, a change in temperature generally causes a phase transition. In a similar fashion, when the concentration of a colloidal system is increased, the solution solidifies; in other words, the particles jam. Hence a direct parallel exists between the concentration of colloidal solutions and the inverse temperature of atomic and molecular materials as illustrated in figure 1.1.

1.1.1 Why colloids?

Colloidal systems are frequently used in experiments to model atomic and molecular liquids and solids because of their relative accessibility to laboratory techniques. The colloids, having a size on the scale of a micron, are observable under an ordinary microscope. By contrast, atoms and molecules are visible only by employing techniques such as scanning tunneling microscopy. In addition to the length-scale, the time-scale involved differs significantly. Attaining a time resolution sufficient to directly observe the movement of atoms and molecules is extremely challenging. The diffusion constant for particles in solution is given as:

$$D = \frac{k_B T}{6\pi\eta a} \tag{1.1}$$

where k_B is the Boltzmann constant, T is the temperature, η is the viscosity of the suspending fluid and a is the radius associated with the diffusing particles. The diffusion constant is related to the mean square displacement (MSD) as

$$\langle \Delta r^2 \rangle = 6Dt \tag{1.2}$$

where t is time. From these equations it can be shown that the time scale of diffusion for colloidal particles is 10^9 times bigger than that of atoms and molecules. This makes it possible to use ordinary laboratory techniques to conduct structural and dynamical measurements on the colloidal suspensions.

So colloids provide an elegant and simple way to model the dynamics and structure of atomic and molecular systems in a laboratory setting; the experiments are relatively straightforward to do and can be repeated as many times as one deems necessary. A range of experimental methods can be devised relatively easily to extract the relevant information in the experimental models. An analogy with molecular or atomic systems is often drawn in which each colloidal particle in the suspension represents an atom or a molecule; the parallel is then used in the attempt to understand the fundamental physics governing the phase behavior of materials.

1.1.2 Types of colloids

Colloids can vary in shape, size, chemical composition, particle internal structure, mechanical and electronic properties. A major class are hard-sphere colloids, which interact through volume exclusion only; these have been used extensively to model crystallization and glass formation in materials [2, 10, 20, 21, 33, 40, 41, 52, 53, 55, 73]. Core-shell particle types are also widely used and offer an advantage in imaging as

the particles in a densely packed suspensions are clearly optically separated. Soft colloids are interesting because their deformability allows a wider variety of packing behavior to be observed [39]. Hard-spheres jam at random close packing; by contrast, soft spheres can move even when they are squeezed. Nonspherical colloids can modify properties of liquid crystals, and can be used to better mimic materials [31, 22].

In addition to the morphology of particles, their charge and hence the interaction potential between them can be tuned allowing a wide array of suspension behaviors to be observed; examples are attraction induced gelation and tunable interactions between microgel particles [36, 8]. Stiffness of particles can be controlled by changing the ratio of constituent monomers: simply increasing the cross-linker content of particles can make them stiffer [62]. Such flexibility in the types of the colloids allows a robust set of experiments to be performed, as can be attested by the extensive publication in the area of colloidal science.

1.1.3 pNIPAm based colloids

Experiments suggest that making the colloidal particles deformable allows a wider range of phenomena to be observed [4, 39, 29]. Microgel particles, which are made from a cross-linked and solvent-swollen polymer gel, can be used to achieve deformability. A frequently used microgel system is that synthesized from N-isopropyl acrylamide (NIPAm) and acrylic acid (AAc) resulting in a copolymer, poly(n-isopropylacrylamide)-co-(acrylic acid), or p(NIPAm-co-AAc) [2, 49, 42, 43, 45, 46, 76]. The polymer composition can be varied to control sensitivity to chemicals; for example, the AAc content can be manipulated to tune sensitivity to pH level

[30, 23, 63]. The lower critical solution temperature (LCST) of pNIPAm allows control of the size of the microgel particles and hence the volume fraction of the colloidal suspension. This property provides a straightforward way to induce phase transitions; a closer look at transitions in and out of jammed states is thus possible due to this finer control [75, 80, 56]. Quenching into glassy states can be achieved by lowering the temperature of the suspension from above the LCST which causes swelling of particles [46, 80, 79, 2]. Varying stiffness has enabled a wider glass forming behavior to be observed; the softer the particles the less fragile the glass they form [39]. In comparison, hard-sphere colloids can be used to model only fragile glass formers. The full potential of soft-sphere colloids in the study of glass formation remains to be unlocked.

1.2 Applications of colloids

In addition to serving as model systems in the study of a plethora of phenomena including glass formation, crystallization, sedimentation, clogging, and drying of complex mixtures [1, 77, 78], colloids are also widely used as additives in cosmetics, paints, inks and foods, where they modify the properties of the products [5, 13, 67, 66]. Colloidal particles improve the adhering property of car paints; their usage and careful balance gives the smooth and lustrous finish brand new cars posses [67]. Silver-colloids have been applied for printing [27]. In oil extraction, polymer colloids are used as flooding agents to flush trapped oil; there is an ongoing research to create new type of smart particles that would encapsulate trapped oil to later release it, acting like micro-transport agents. The chemical- and bio-responsivity of

colloids can be expolited for drug delivery [71]. They can be designed to incorporate drugs for targeted and fast release [7]. Such a wide range of current and potential application of colloids has continued to invigorate research in colloidal science.

1.3 Experimental techniques

The wide range of research in colloid science has meant employing a diverse set of techniques in the experiments. Rheological measurements are used to characterize the mechanical and dynamical properties of dense colloidal suspensions thereby helping us to understand the physics of glass formation and ageing [9, 10]. Both bright-field and confocal microscopy combined with image analysis techniques provide direct information on the packing structure, the jamming transition, the ageing dynamics, the effect of colloid-colloid interaction, phase separation, gellation, and numerous other phenomena that occur in colloidal suspensions. Rheo-confocal setups allow us to simultaneously probe and record the response of the experimental system; the mechanism of rearrangement of particles and how this is dictated by the external stress sheds light on shear stress influenced phenomena. Microfludic devices are used to investigate clogging of channels when transporting colloidal particles; the experimental result will help resolve issues of clogging in systems such as arteries. Laser light and neutron scattering techniques are used to measure size of particles, dynamics of suspensions, and structure of individual particles.

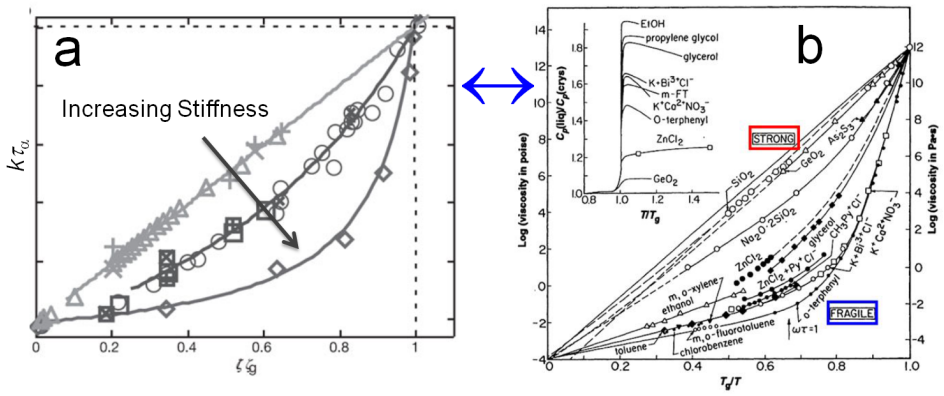

Figure 1.2: Softer particles make stronger glasses (a) Relaxation behavior as a function of concentration for microgel particles as the stiffness is varied [39]. (b) Viscosity of molecular glass formers as a function of inverse temperature. The inset is a plot of heat capacity (C_p) as a funciton of temperature [3].

1.4 A summary of new findings

I begin by discussing synthesis methods for fluorescently labeled p(NIPAm-co-AAc) microgel particles. The resulting particles can be imaged under a confocal microscope for several hours without significant bleaching. Standard tracking algorithms [12] can be employed to analyze the images and produce accurate identification of particles and tracking of particle locations over time. A set of calculations such as pair correlation functions, mean square displacements, single particle tracking, and rendering are used to extract the relevant physics. The techniques used and illustrative data are discussed throughout the thesis. I also present experimental procedures to create high quality data suitable for image analysis.

I present structural and dynamical study of suspensions of pNIPAm microgel particles as a function of stiffness, size, concentration of particles, and pH level of the suspension. By changing the pH of the suspension, it is possible to control the interaction between the particles; this has a strong effect on how the structure and

dynamics of the suspensions evolve over time. By following the temporal development of the dynamics and structure of the suspensions, our experiments demonstrate that p(NIPAm-co-AAc) microgel colloids follow distinctly different routes to dynamic arrest depending on the pH of the suspension. Previously, the final state of the microgel suspensions has been reported to be a function of the pH and concentration of the suspension [42, 30]; but what happens between the initial fluid-like state and the final solid-like state has remained unclear. We find that at low pH, where particles are slightly attractive, the dynamics is dictated both by attraction driven nucleation of crystals and concentration. Nucleation occurs homogeneously in the suspensions without restriction to geometric boundaries. In addition, crystallization is nucleation-limited, where a sudden and fast rise in crystallinity occurs after concentration dependent lag time. By contrast, at high pH, where particles are charged and repulsive, concentration of particles dictates the phase behavior. At both low and high pH, the higher the concentration, the smaller the particles get. This illustrates that increasing the density of soft colloids has two complementary effects: isotropic shrinking and deformation. The resulting suspension is jammed and shows no observable relaxation. The details of this finding are included in chapter 5 and published in [46].

I also discuss experimental results showing that the structure of crystals formed by p(NIPAm-co-AAc) microgel particles does not depend on charge, stiffness, and concentration of particles remaining FCC under all conditions. In attractive conditions and at very low concentration where crystallization is mainly the result of attraction driven nucleation, the structures are polycrystalline solids. The crystals formed display remarkable stability maintaining their structure even after external

pressure is applied to them, a property unique to these soft spheres. These results are included in chapter 6 and published in [47].

1.5 Structure of thesis

In chapter 2, I explain the synthesis and characterization of p(NIPAm-co-AAc) microgel particles. The synthesis procedure and the reaction process are covered in some detail. I will discuss dynamic light scattering techniques used to characterize size. An overview of charge-pH relationship in the suspensions supported by data from zeta potential measurement is given. This chapter will summarize important facts about the soft sphere particles employed in this research.

In chapter 3, I detail the experimental procedure with a focus on microscopic methods employed in the experiments. Sample preparation, experimental challenges encountered and the steps taken to overcome them, image quality issues, instabilities in sample, and image acquisition are covered. Confocal microscopy as it applies to imaging fluorescently labeled microgels is discussed.

In chapter 4, A summary of the different methods and tools employed to analyze and understand our microscopy data is presented. Using the tracked positions, ensemble and single particle mean squared displacements are computed. Calculation of MSDs in 3D and 2D are compared. A brief discussion of pair correlation functions, voronoi tessellations, and rendering techniques are given.

In chapter 5, I report our first contribution to the field of deformable colloids published in [46], where we determine how the interplay of pH and concentration dictates the temporal evolution of the p(NIPAm-co-AAc) microgel colloidal suspensions.

Attraction induced, homogeneous nucleation and growth of crystals dominates the dynamics in the low pH systems. By contrast, concentration dominates the dynamic behavior at high pH when particles are repulsive. In addition, I present data on the packing structure of the soft particles: as they are packed to higher concentrations, they deswell isotropically.

Chapter 6 summarizes results on investigation of crystallization behavior of our microgles. Simulation results predicted that ionic polymer particles of smaller size and smaller charge have a crystallization behavior that depends on charge, size, and concentration [24, 23]. The experiments reported in this chapter show that the crystal structures formed by our p(NIPAm-co-AAc) colloids is invariably FCC under varying particle charge, size, concentration, and internal structure. We also observe different spacial behaviors as a function of the charge on the particles without any effect on the crystal structure.

In chapter 7, I present further data on the concentration dependent dynamic arrest in microgels systems. In summary, the denser the system the less dynamic it is. This behavior holds throughout the different samples studied. The dynamic behavior is reminiscent of packing dynamics in hard-sphere colloids, save for differences in the extent of packing possible in the two systems.

Chapter 8 discusses AFM of microgels. I outline the steps followed and discuss the results obtained. Such a measurement can be used to measure the stiffness of the particles, as we do, but also can be applied for measuring the interaction potential between the particles.

Chapter 9 gives a summary of the main points in the thesis, presents current

preliminary data, and discusses possible future directions.

Appendix A and B The codes I authored and are used in data analysis are given.

Chapter 2

The particles - synthesis and characterization

2.1 Synthesis

Microgels are synthesized by precipitation polymerization of constituent monomers. The synthesis reaction takes place at a temperature of 70 °C, the most convenient temperature for the formation of radicals from the reaction initiator.

2.1.1 Synthesis procedure

The monomers used as building blocks are Isopropylacrylamide (NIPAm) and Acrylic Acid (AAc). The crosslinker is Methylene-bis-acrylamide (BIS). Potassium persulfate (KPS) is used as initiator. A scarce amount of sodium dodecyl sulfate (SDS) is used as a stablizer and Rhodamine B (PolyFlour 570 ©, Polysciences, Inc.) is added for fluorescent labeling of the particles. Their formulas are shown in figure

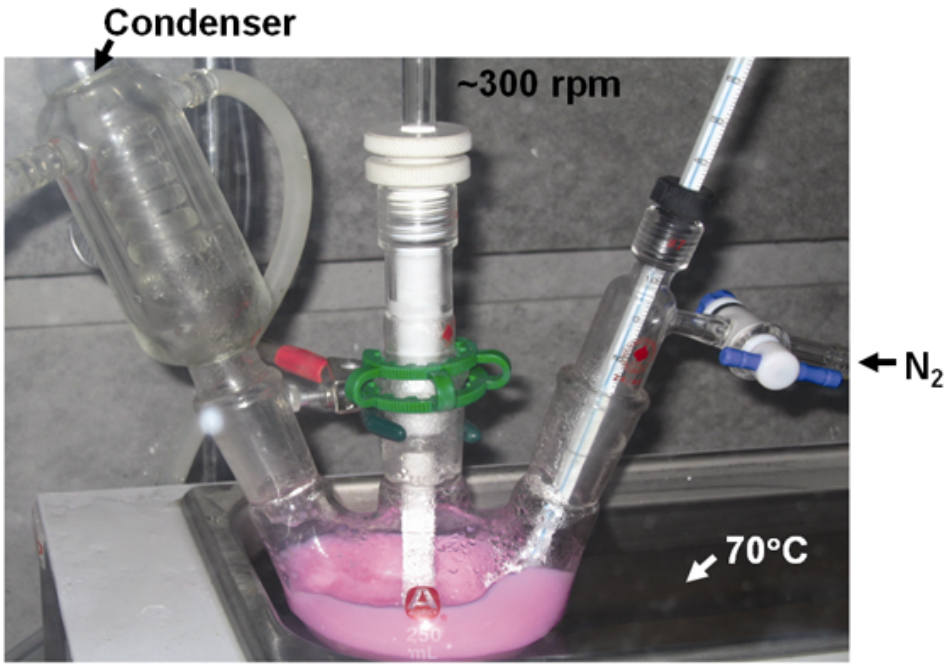

Figure 2.1: Reaction setup.

2.2.

- Measure monomers to obtain required ratio. Typical amounts are: NIPAm - 3.6 gm, BIS - 0.5-10% of 3.6 gm, AAc - 0.29 gm. Put these together in a 500 ml flask and add 200 ml of water.

  Separately prepare: KPS - 0.29 gm in 10 ml of water, SDS - 0.1 gm in 5 ml of water, Rhodamine and Dimethylsulfoxide (DMSO) (0.3 ml) together in 10 ml of water. Make sure that the KPS is mixed well by vortexing. Sonicate if necessary.

- Bubble Ar or N_2 gas in the reaction mixture to remove dissolved O_2. This step can be skipped if one is flowing N_2 gas through the flask during the reaction.

- Add sufficient water in the flask for a final volume close to 400 ml (after adding all chemicals). Set up the reaction as in figure 2.1. Set the temperature to 70 °C. The level of the Heat bath fluid should be slightly higher than the level of the reaction mixture in the flask. Make sure the stirrer and the N_2 flow line are properly placed.
- After stirring the mixture for about 10 min, add initiator using a syringe.
- Wait for 15 min and add the SDS solution. Add the Rhodamine solution right after.
- Leave to react for about 3 hours.
- When done, cool down to room temperature while stirring. Then quench the reaction mixture by putting the flask in a bucket of ice. Filter into a storage container using a regular paper filter to remove macroscopic aggregates and impurities.

2.1.2 Reaction kinetics

The reaction occurs according to the simplified chain of events I describe here. When 70 °C is reached (see above), the dissolved initiator is added. The persulfate breaks up creating free radicals according to equation 2.1.

$$K_2S_2O_8 \rightarrow 2K^+ + S_2O_8^{-2} \tag{2.1}$$

The free radicals readily combine with the hydrogen-rich NIPAm or AAc monomers (denoted as M in the equations) to create conjugated radicals that contain persulfate

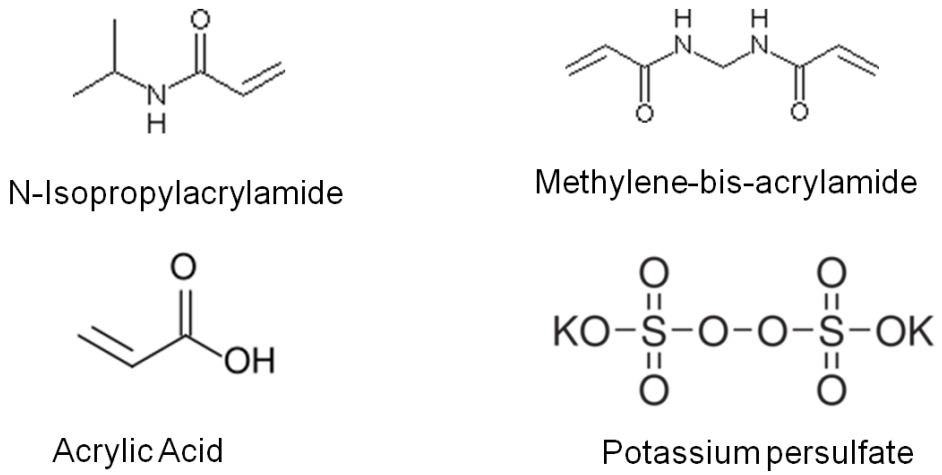

Figure 2.2: Basic constituent chemicals in the synthesis of pNIPAm-co-AAc microgel particles

and mononmers, in a process dubbed initiation.

$$R^{\bullet} + M \rightarrow RM^{\bullet} \tag{2.2}$$

This process is repeated (propagates).

$$RM_n^{\bullet} + M \rightarrow RM_{n+1}^{\bullet} \tag{2.3}$$

The combination of radicals produces a neutral polymer chain, in a process named Termination.

$$RM_x^{\bullet} + KM_y^{\bullet} \rightarrow KM_{x+y} \tag{2.4}$$

The precursor particles form either new particle centers or attach with already growing nuclei. Stabilization of nuclei is steric (volume exclusion) and electrostatic. The anionic surfactant SDS helps stability of nuclei by increasing their surface charge. When all monomers are consumed, the nuclei can no longer grow and the reaction can be stopped. A detailed discussion on the effect of varying reaction time, composition

of reactants, and other factors that influence reaction kinetics is given in references [16, 76].

2.1.3 Cleaning

The sample is then cleaned by repeated centrifugation at 10,000-14,000g (Multifuge X1R centrifuge, Thermo Scientific) and redispersion in deionized water (Millipore Milli-Q, Integral 10). This removes unreacted monomers from the surfactant. The particles are considered clean when the top part of a centrifuged sample is clear except for slight tint from the dye.

2.2 Characterization

Our particles are first characterized by measuring their size as a function of temperature and pH through dynamic light scattering. The scattering measurement is done on an ALV/DLS-5000 laser light scattering spectrometer/goniometer and autocorrelation is done with ALV-5000/60XO digital correlator software by ALV-GmbH. We also measure the zeta potential to quantify the amount of charge on the particles.

2.2.1 Dynamic light scattering (DLS)

Theory

There are a number of assumptions made for the theoretical derivation of relevant equations. The first is that scattering is assumed to be elastic, hence the magnitudes of the incoming and scattered vectors are equal, $K_o = K_f$. This implies that there is

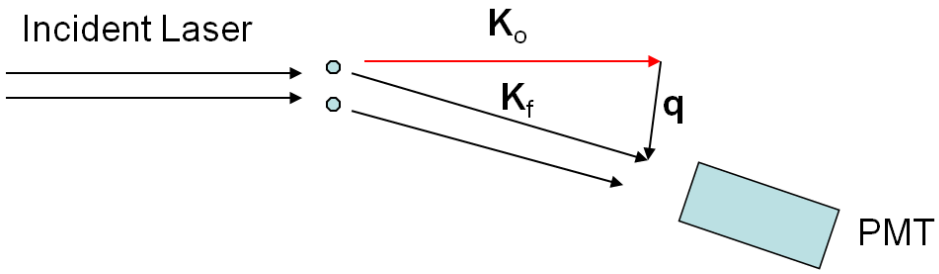

Figure 2.3: Laser light scattered from sample is detected by the photo multiplier tube (PMT) situated at an angle $\hat{q}$ with corresponding wave vectors $\hat{K}_o$ and $\hat{K}_f$.

no energy loss during scattering of the light wave as a result of momentum transfer from the wave to the particles. In addition, the colloids are required to be index matched with the suspending fluid. This allows us to assume that diffraction at the colloid/fluid interface does not play a role; hence can deduce the direction of light in the sample to be the same everywhere. Since our particles are mostly made of water, index matching is automatic. The measurement is done in the dilute limit to minimize multiple scattering. This is roughly checked by examining the sample by eye and making sure that it is optically clear. For spherical particles, the scattering amplitude can be assumed to be independent of the orientation of the particles, hence the scattered intensity is proportional to density fluctuation.

The magnitude of the scattering vector, $\hat{q}$, is given as

$$q = \frac{4\pi}{\lambda} \sin \frac{\theta}{2} \tag{2.5}$$

The intensity, I, of the scattered light is measured by the PMT. The autocorrelation function of the intensity, $g_{\text{I}}(\tau)$, is given as

$$g_{\mathrm{I}}(\tau) = \frac{\langle I(t+\tau)I(t)\rangle}{\langle I(t)\rangle^2} \tag{2.6}$$

The electric field autocorrelation is defined as

$$g_{\mathrm{E}}(\tau) = \frac{\langle E(t+\tau)E(t)\rangle}{\langle I(t)\rangle} \tag{2.7}$$

It can be shown that the two are related as $g_{\mathrm{E}} = \sqrt{g_{\mathrm{I}} - 1}$. The detailed derivation can be found in [15]. One can deduce the equation relating the diffusion coefficient in equation 1.1 and g_{E}

$$g_{\mathrm{E}}(t) = e^{-Dq^2t} \tag{2.8}$$

Plotting $\frac{1}{\tau}$ values from figure 2.4 as a function of q^2 gives D. Equation 1.1 is then

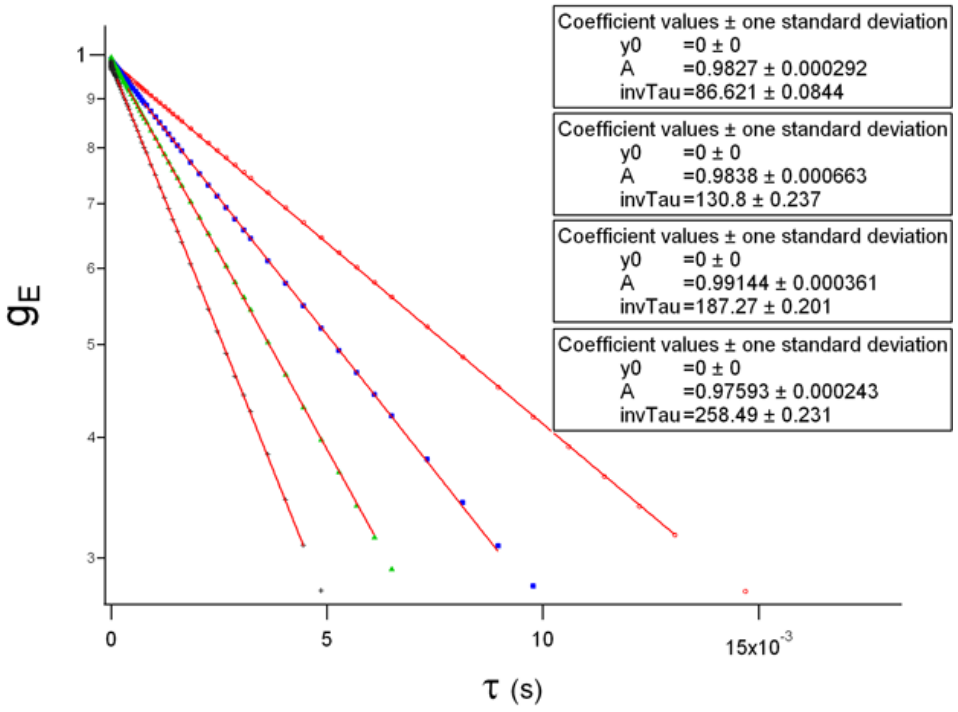

Figure 2.4: g_{E} as a function of delay time, τ for, from right to left, $\theta = 30°, 40°, 50°$, and $60°$.

used to compute the hydrodynamic radius, a. What we just described is the cumulant

method. Alternatively, one can fit a well averaged g_{E} with an exponential and use the Contin algorithm to compute the radius.

Scattering measurement

Methods

A few microliters of the cleaned particles are diluted with milli-Q water until the suspension is optically clear. A cuvette (pyrex culture tube, 9820-10 Corning Inc.) is then filled half-way with the diluted sample, and covered with a cup. This is placed in a chamber containing toulene, which is index matched with the cuvette to circumvent refraction. A 633 nm HeNe laser light is used for the size measurement. This is suitablly well beyond the excitation wavelength of Rhodamine B. This insures that fluorescence of the dye does not interfere with the experiment. Data is collected for 5 minutes at each angle set at $30°, 40°, 50°$, and $60°$. using the goniometer to automatically adjust the angle. The intensity autocorrelation is then fitted with exponentials as in figure 2.4 to obtain $\frac{1}{\tau}$, which is plotted as a function of q^2 to find the slope, D.

Results

The size of the particles measured is in the range of 1.0-1.5 μm in diameter at room temperature. pNIPAm-based microgel particles are known to have temperature and pH dependent size. The particles synthesized do shrink past the lower critical solution temperature (LCST) of NIPAm (32 °C) as shown in figure 2.5. The higher the cross-linker to monomer ratio, the less the particles shrink upon heating, as

one can see going from the 0.8% to 10% sample. Both the deswelling and swelling curves (red and blue respectively) are shown for the softest sample. The swelling and deswelling of polymer gels can be explained by considering the mixing and demixing free energy of the polymers with the solvent. The total free energy is the sum of the free energy of mixing the polymer with the solvent and the free energy due to change of configuration. The size of the polymer cloud is then decided by the minimum position of the total free energy at a given temperature [32].

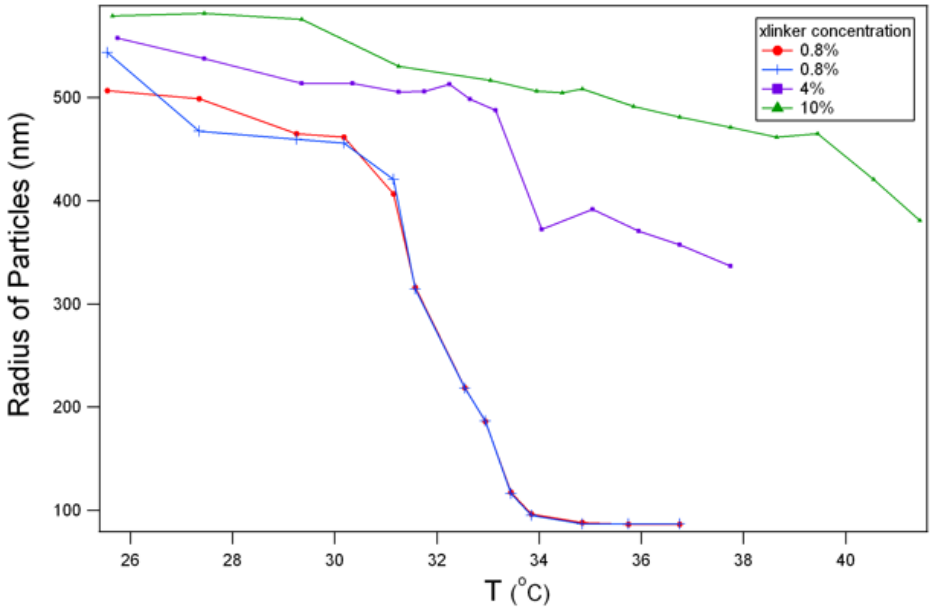

Figure 2.5: Size as a function of temperature for samples with different cross-linker to monomer ratios.

A point of contention concerning scattering experiments involving polymeric colloids should be raised here. The particles constitute mostly water with very low polymer volume fraction of around 0.13 below the LCST [38, 65]; hence it is not straightforward to think about the mechanism of scattering. In other words, is the fluctuation caused by vibrations of the cross-link points, or is it caused by diffusion of

the particles? In spite of this uncertainty, the size found from the DLS measurement is close to the size estimated roughly from the confocal images, shown for particles with hydrodynamic diameter of 1.2 μm in figure 2.6.

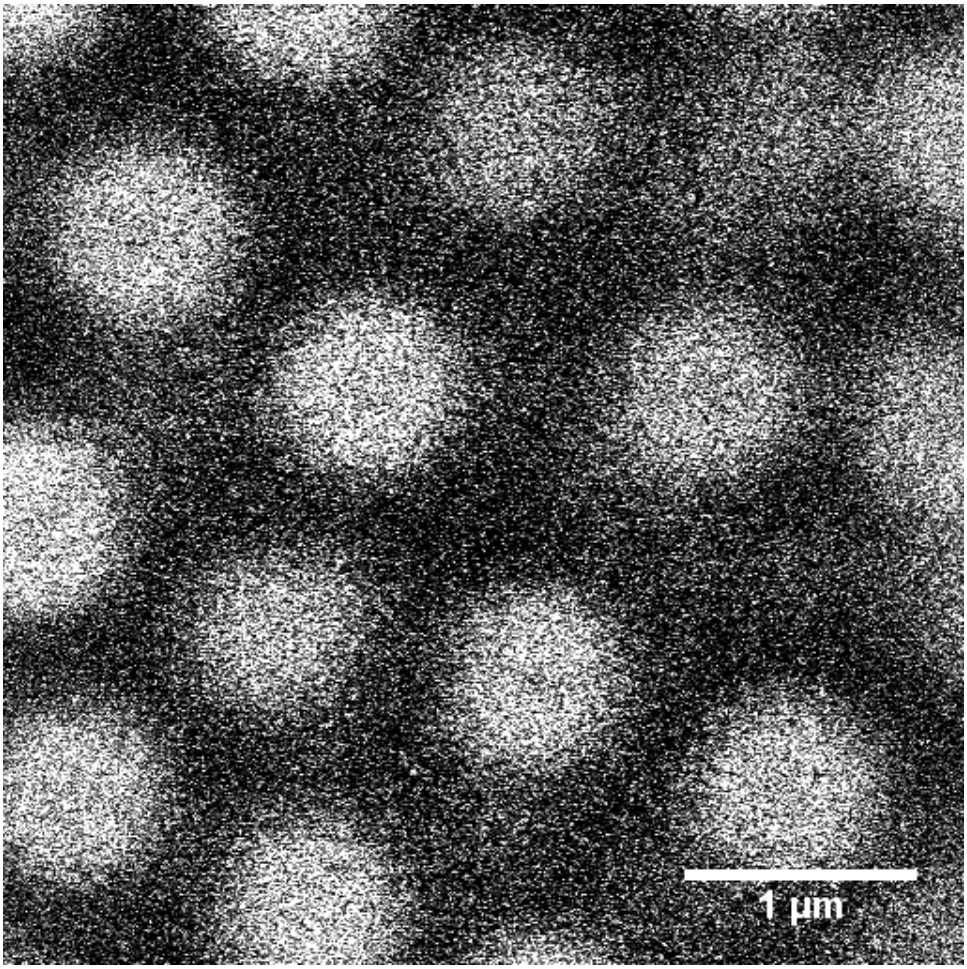

Figure 2.6: A close up fluorescent image of the microgel particles.

The pH of the suspension also influences the size of the particles. The pKa of AAc, which imparts pH sensitivity to the polymer network, is close to 4.5. Hence, the higher the pH, the bigger the charge on the chains forcing them to repel each other; as a result the particles swell. The opposite is true at low pH. This is shown

in figure 2.7.

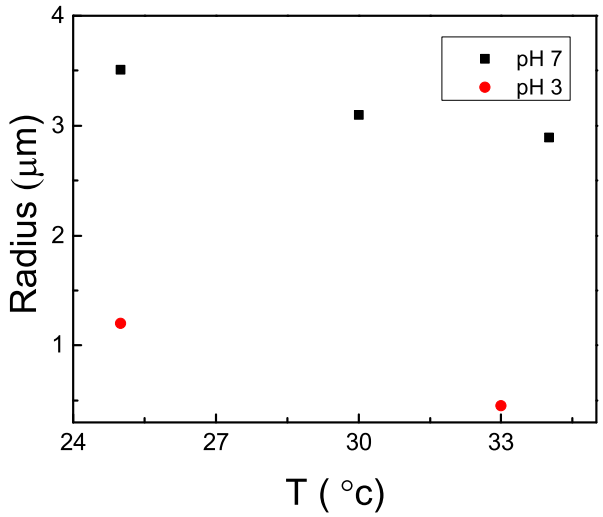

Figure 2.7: Size as a function of temperature and pH for PMMA-NIPAm-AAc core-shell particles.

2.2.2 Zeta potential and charge

Another characterization of the particles is done by measuring the zeta potential (Malvern Zetasizer) in dilute solutions. The zeta potential is defined as the potential at the periphery of the electrical double layer that surrounds an ionic particle in a solution (see figure 2.8). The negatively charged particle attracts counterions from the solution, which form a layer of positive charge, called the stern layer. More counterions accumulate beyond the stern layer forming the diffuse or the slipping layer. The zeta potential is the potential difference between infinity and the edge of the diffuse layer. The electrophoretic mobility of the particle is determined by this potential. The measured zeta potential is used to deduce the charge on the particles. I obtain potential values of -0.7 mV at pH = 3, -12 mV at pH = 5.0 and -16 at pH

= 7, these agree with values in [56]. The critical potential for aggregation to occur is usually given as ±25 mV. Regardless, I see no aggregation in our particle suspensions.

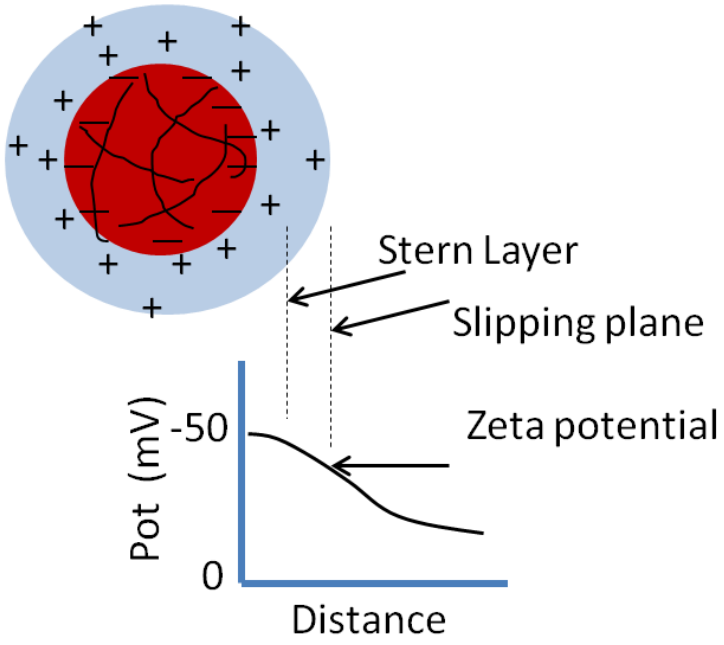

Figure 2.8: Potential profile of ionic particle in aqueous solution.

Using the measured zeta potential one can calculate the charge on the particles. First one needs to calculate the Debye-Huckel parameter (equation 2.9) for the specific pH values listed.

$$\kappa = \left(\frac{2ne^2}{\epsilon_r \epsilon_o kT} \right)^{\frac{1}{2}} \tag{2.9}$$

where n is the ionic strength of the solution, e is the electron charge, ϵ_r is relative permitivity of solution, ϵ_o is permitivity of vacuum, and k is the Boltzmann constant. The ionic strength of HCL solution at pH = 3.0 is close to $0.01M$. This value is $0.025M$ at pH = 5 [56]. The surface charge density, σ, on a particle can then be

expressed in terms of κ and the zeta potential, ψ, as described in [48].

$$\sigma = \epsilon_r \epsilon_o \kappa \frac{\kappa a + 1}{\kappa a} \psi \tag{2.10}$$

Using this, the σ is found to be $-4.53 \times 10^{-8} \frac{C}{m^2}$ at pH=3, $-1.55 \times 10^{-4} \frac{C}{m^2}$ at pH=5.0, and $-2 \times 10^{-3} \frac{C}{m^2}$ at pH = 7. For ~ 1 μm sized particles, these correspond to charge values of $57e$, $3000e$, and $4000e$, where e is the electron charge.

2.3 Particle structure

Neutron scattering measurements indicate that the particles have structure that depends on distance from the center: the polymer density decreases radially outwards [38, 65]. The scattering experiments have also shown that gradient in density is smaller for stiffer particles with higher cross-linker to monomer ratios. Our experimental methods do not provide a measure of the density gradient for a given particle. Nevertheless, we see a clear gradient in the dye concentration with the centers being brighter than the outer parts: the particles either have a higher polymer concentration towards the center, or the fluorescent dye is consumed completely at an earlier stage in the synthesis.

The periphery of the particles is not well defined. The neutron scattering experiments mentioned above can be interpreted to mean that the particles end with hairy extensions. This obscures definition of packing induced deformation, since deformation can exist even when particles are not touching due to the feathery nature of the outer section.

The overall density of the particles depends strongly on the cross-linker to monomer

ratio. The higher the ratio, the quicker the particles sediment upon centrifugation. For example, the 10% cross-linker to monomer ratio particles sediment to the bottom if centrifuged for 1 hour at 10,000g. By contrast, particles with 4% cross-linker to monomer ratio have to be centrifuged for more than 3 hours at 14,000g for satisfactory sedimentation, confirming the dependence of particle density on cross-linker concentration.

Chapter 3

Microscopic methods

As discussed in chapter 2, our system consists of poly(N-isopropylacrylamide-co-acrylic acid) particles cross-linked with N-N-methylene bisacrylamide synthesized by precipitation polymerization, yielding microgels with a fully swollen size in the range of 1.0-1.5 μm in diameter as measured by dynamic light scattering in dilute solutions. The particles are fluorescently labeled using Rhodamine B, which copolymerizes with the p(NIPAm-co-AAc) network. After the synthesis, the particles are cleaned by repeated centrifugation and redispersion in deionized water. These microgels have physical and chemical behaviors that are sensitive to pH, ionic strength, temperature, and polymer content.

3.1 Sample preparation

The centrifuged suspensions can be further concentrated by dialyzing against a 10 wt% solution of dextran (molecular weight of 70 k/mol), resulting in an applied

osmotic pressure of approximately 20 kPa [34]. A series of suspensions of varying concentrations are then prepared by diluting this concentrated suspension. To vary the pH, a $0.1M$ HCl or NaOH is used. First, a substantial volume of dilute sample at the desired pH is prepared. The solution is then centrifuged to concentrate it.

The cell for imaging should fulfill a set of requirements.

- Must on one side be made of a coverslip (VWR No 1.5, $0.16-0.19$ mm thickness) with a refractive index of 1.525. This is required for confocal imaging.
- Must be easily fillable with sample.
- Must be hermetically sealed. This is to avoid leakage of sample and movement of air.
- Must not be easily affected by temperature changes.

I passed through several generations of sample cells before coming up with a design that fulfilled the requirements. Representative designs are shown in figure 3.1a-d appearing in order from the earliest to the latest. The separator in 3.1d is made of plastic and cut into shape using a laser cutter.

Before loading to sample cell

A few micro-liters of the sample are placed in a tube and vortexed thoroughly for about 3 min. The purpose of vortexing it is to apply shear and erase any ageing related artifacts such as attraction or concentration induced arrest. The sheared sample is then degassed under vacuum to remove dissolved air; the vacuum is vented when the

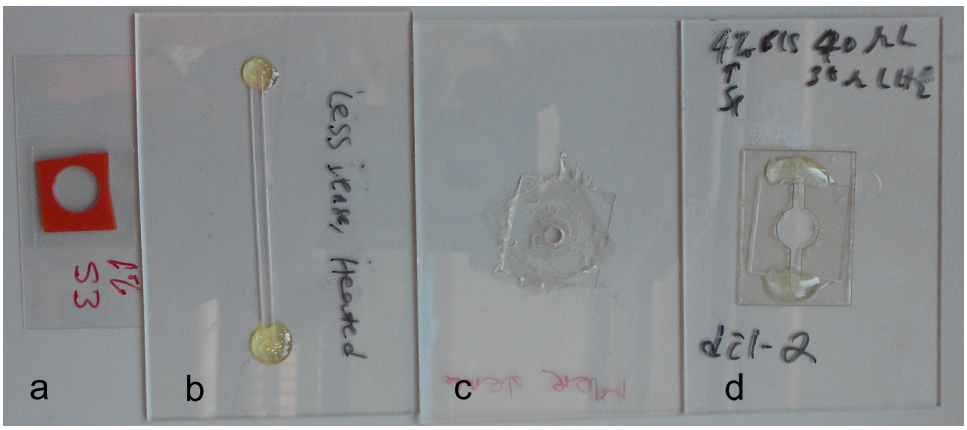

Figure 3.1: Example cells

sample stops bubbling. Degassing helps to reduce amount of dissolved oxygen which can cause faster bleaching of the fluorescent dye during laser induced excitation.

Sample loading

In case of the cell shown in figures 3.1b and d capillary forces are used to suck the sample in. A drop of the sample is placed in contact with the opening on one end, while the other end is free for displaced air to escape through. The time it takes for the sample to load is between a few seconds to several minutes, depending on the viscosity. The cell is then sealed using epoxy at both ends to prevent drying and convection. In cases where the sample is too viscous for capillary drag to work, sample cells as in 3.1a and c are used, and the sample is pipetted directly into the cell.

Initialization

We initialize the sample by quenching from a temperature above the lower critical solution temperature (LCST) of pNIPAm to room temperature, where the particles become fully swollen [11, 68]. The sample is then kept at room temperature for 1 hour, which is sufficient time for the particles to swell and reach thermal equilibrium. After image acquisition, the particle positions are determined using particle tracking algorithms [12, 73].

3.2 Confocal scanning microscopy

The confocal scanning microscope was invented by Marvin Minsky in 1955 at Harvard [44]. The invention came out of the need to avoid unnecessary scattered light from microscopic images. The solution was to selectively illuminate a point of the specimen and to look at the scattered or fluorescent light coming only from that point. Additionally, placing a pinhole next to the detector helped to block scattered light from non-focal points. Information from each point is then reconstructed on a computer screen producing the full image of the scanned-field. Three-dimensional images are obtained by putting together planar scans from different heights in the specimen.

How it works

The method works by illuminating a point in the sample at a time and using moving slits to scan through the field of view. A pathway of the light is shown in figure 3.2. A Helium-Neon source is used to generate 543 nm and 633 nm lasers

while an Argon source produces a 488 nm laser. The laser light is first expanded by a diverging lens and a collimator is used to parallelize the waves. This is reflected towards the objective by a dichroic mirror. The mirror has the property that it reflects light below a specific wavelength and allows the rest to pass through, providing a way to isolate the fluorescent light, which has higher wavelength than the excitation laser (a phenomenon called stoke-shift). An acousto-optical beam splitter (AOBS) can also be used for this purpose: a narrow band of light (as narrow as 1 - 2 nm) can be selected to pass through in this case. The laser light is then guided by the scanning mirrors that sweep the field of view in the x and y directions. The fluorescent light from the focal point passes back through the scanning mirrors, and the dichroic mirror to be focused onto the pinhole. There are filters placed in front of the dichroic mirror and after it just before the pinhole (not shown in figure) to further insure that the only wavelengths that get to the sample and then to the pinhole are the excitation and the fluorescent wavelengths respectively. Any light that comes from the off-focal points is blocked by the pinhole. In figure 3.2, the off-focal lights correspond to the red and the blue lines. The red line represents a ray that originated from above the focal point in the specimen (the set up in the figure is inverted) and is focused onto a single point before the pinhole. By the time the ray reaches the pinhole, it has re-dispersed and is blocked. Similarly, a ray originating from below the focal plane reaches the pinhole before it is focused into a point and is thus blocked. The same is true for rays originating from non-focal points in the same plane as the focal point. The stage or the objective of the microscope is moved vertically to image a different plane. The final 3-dimensional image is obtained by putting together pixel information from the

scans.

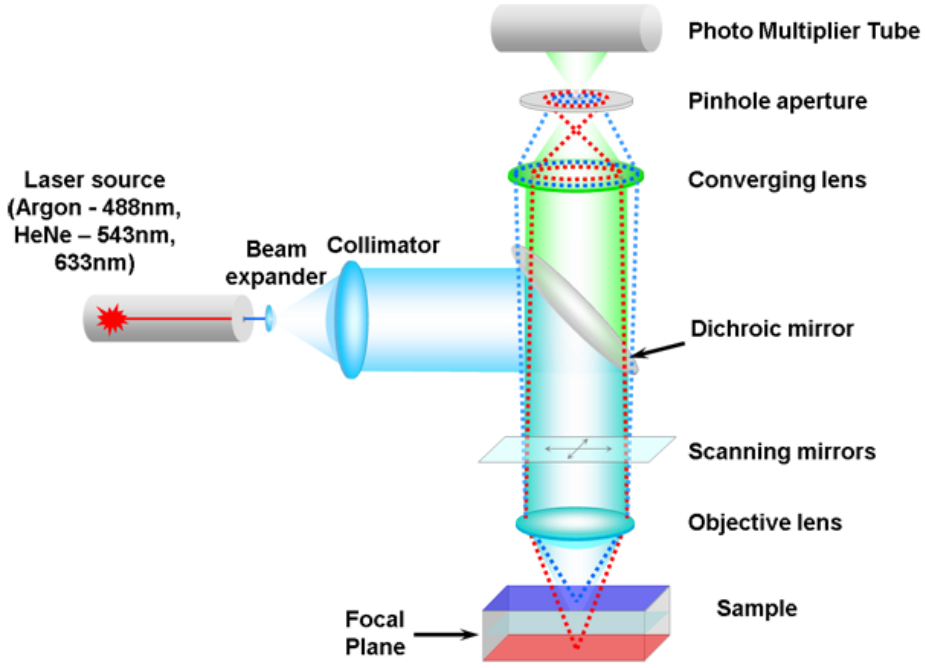

Figure 3.2: Schematic of working principle of a confocal microscope.

This design sophistication is still not enough to completely avoid noise, and off-focal point light can still affect images. The suggested solution is a 2-photon microscope where only a few photons are allowed to illuminate the sample at a time; but this has yet to overcome design hurdles [58].

Diffraction limit

The smallest distance between points that are just resolvable is the diffraction limit of the microscope. This determines the smallest feature we can image using the microscope. The diffraction limit is a function of the wavelength of the laser. The smallest focused point of the laser is called the airy disk (shown in figure 3.3). The

width of the central band of the airy disk is given by

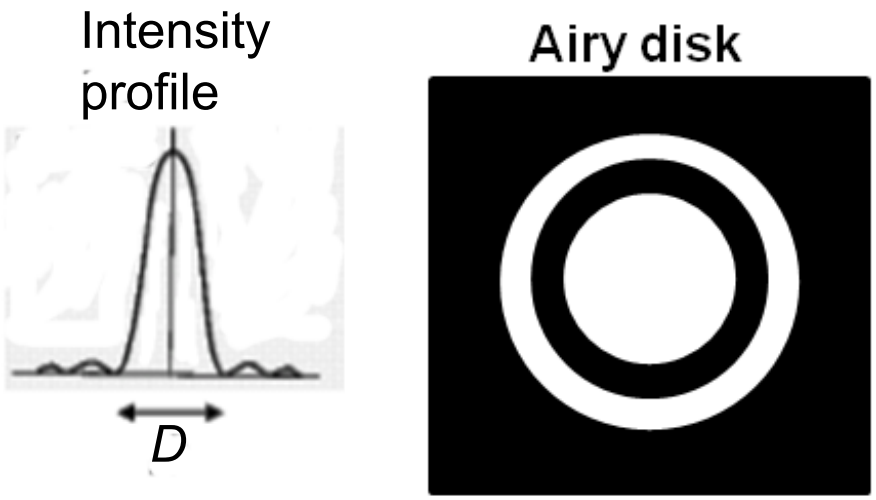

Figure 3.3: The smallest focussed point from a focal plane.

$$D = \frac{1.21\lambda}{n \sin\theta} \tag{3.1}$$

where the numerical aperture, NA, of the objective is given by $n \sin\theta$. The resolution, which is the smallest distance between two resolvable points, is give based on the Rayleigh criterion as:

$$\Delta d = \frac{0.61\lambda}{NA} \tag{3.2}$$

This is the distance between the first minimum and the central maxium of the two airy discs from the two just resolvable points.

The LeicaSP5

Our images are recorded using the Leica SP5. The principles are the same as described in the previous two sections. The use of AOBS makes it easier to use several

excitation lines at the same time, enabling imaging of multi-labeled specimen concurrently. The Leica LAS AF software makes the control relatively straightforward. Using the software, one can control the filter types, the laser power, the objective type (magnification and immersion options), and several other image specifications. The actual microscope on which most data is acquired is shown in figure 3.4.

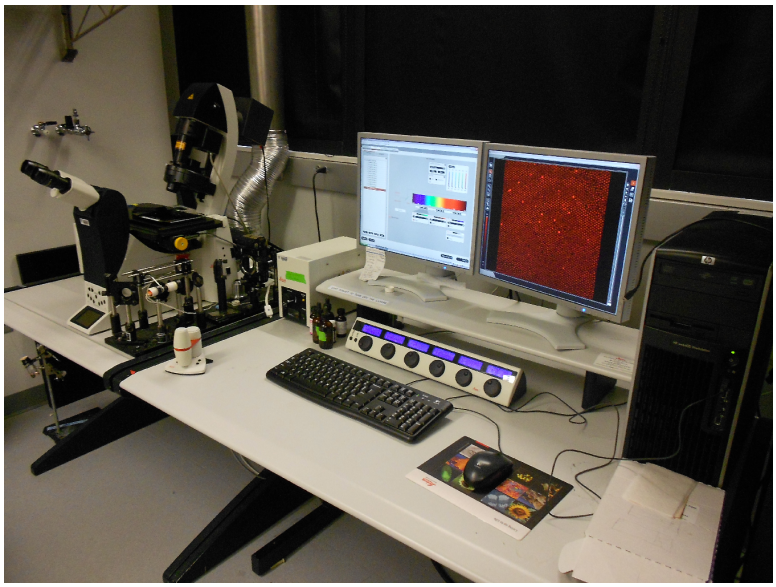

Figure 3.4: Weitz lab Leica SP5 used in the experiments.

3.2.1 Technical details

The Leica SP5 in our lab can be fitted with 10x,20x,40x,63x, and 100x objectives. The objectives are of two types: immersion or dry. I use the immersion objectives exclusively. Both the oil and water immersion objective give good quality images. For longer experiments, only oil has to be used since water dries out very quickly. Other parameters such as line averaging, plane averaging, laser intensity, scanning

speed, width of emission/detection band, smart gain, etc. are adjusted on sample to sample basis. The samples that have low particle density and are more dynamic require faster speed with less averaging and higher laser intensity, with the smart gain as low as possible (700V) to reduce the noise level. For denser samples consisting of slower particles, more averaging is possible (line or plane), hence the laser power can be reduced and smart gain can be turned up (900-1100V); this lessens bleaching. This is particulary important because particles are exposed for longer when moving very slowly. Bi-directional scanning mode can be used to gain even faster speed in case of higly mobile samples. This can give time resolution as small as 150 ms, with image quality still suitable for analysis.

3.2.2 Microscopy of microgels

As the swollen microgels contain more than 90% solvent, their density and refractive index are very close to that of the solvent, which respectively minimize the effects of sedimentation and of optical artifacts due to scattering. By optimizing the laser power and the gain on the photomultiplier tubes (PMTs), one can image the same field of view for several hours without significant loss of contrast due to photobleaching. This eliminates the need for an anti-bleaching agent that could alter the chemical environment of the suspension. The 3D field of view for our image stacks is chosen to be around $35 \times 35 \times 10\,\mu\text{m}^3$, containing between 5000 and 10000 particles, depending on concentration. Images are recorded at a distance of several particle diameters away from the bottom cover slip and several tens of microns away from the side walls to minimize wall effects on the imaging as well as on the data [74, 19].

The centers of the microgel particles appear brighter than their outer parts in the microscopy images; this is due to the fact that microgel particles made by precipitation polymerization are not homogeneous in density, but exhibit a heterogeneous core-shell-type structure with a denser core of cross-linked polymer and a corona, or shell, where the polymer concentration and crosslink density are much lower, as described in chapter 2. The corresponding radial gradient in the dye concentration allows us to identify individual particles even at very high packing densities, as the particle cores remain optically separated. Figure 3.5 shows a typical xy image of the microgels.

Fine tuning the image

Optical artifacts cause the particles to elongate in the vertical direction (perpendicular to the coverslip) as we go deeper into the sample; this can be corrected to some degree by adjusting the pinhole diameter, although it is usually best to leave this at 1 airy, which is what is automatically chosen by the software at start up. The colar on the objective can also be adjusted to find where particles look the most round. Variation in temperature and the thickness of the coverslip ($\sim$ 0.16 mm) can cause this value to vary. To improve the image using the collar, one should set up a dual channel image where both the coverslip and the specimen are imaged concurrently. The interface between the coverslip and the sample can be seen in reflection mode. The correction ring on the objective is rotated slightly until this reflection is as thin and bright as possible. In figure 3.6, an xz image of the same sample as in 3.5 is shown. This image is taken by a 100x Oil immersion objective. It has a better

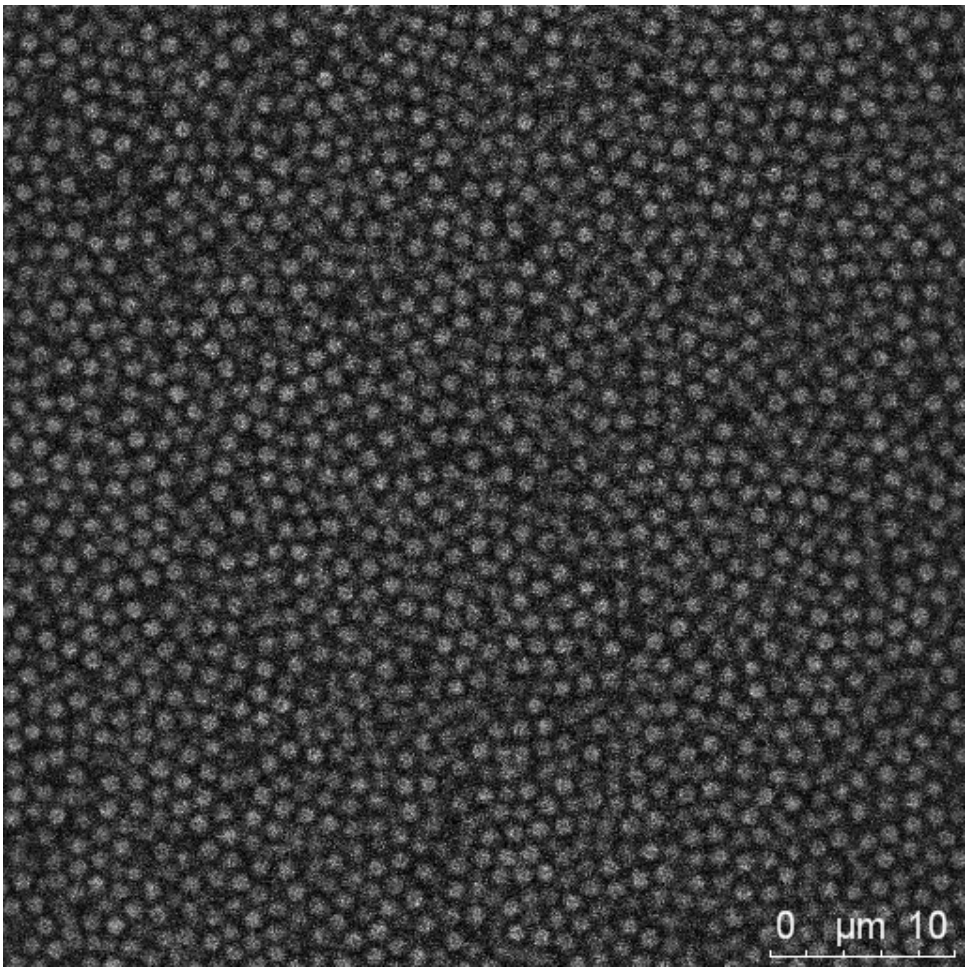

Figure 3.5: A typical unprocessed XY image of microgel particles taken by the Leica SP5.

contrast and brightness than the one in figure 3.7 which is taken with a 63x water immersion objective, with the same settings.

3.3 Concentration calibration

As a result of deformability of the microgel particles, their volume changes and the traditional definition of volume fraction in colloidal suspensions no longer reflects

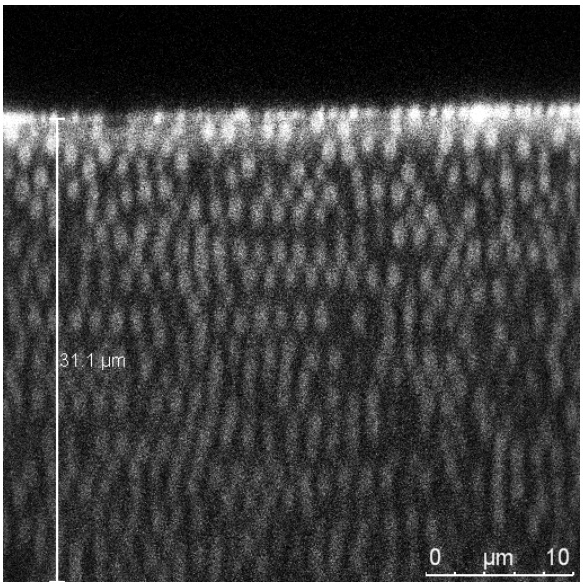

Figure 3.6: A vertical cross-section of sample in figure 3.5 taken with the 100x oil immersion objective.

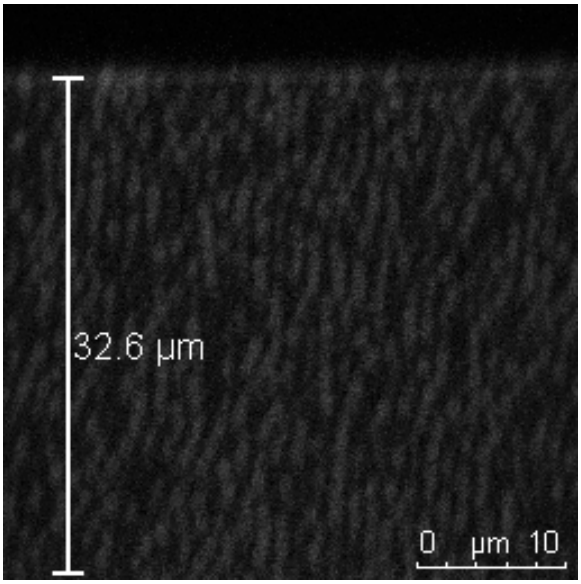

Figure 3.7: A vertical cross-section of sample in figure 3.5 taken with the 63x water immersion objective.

the concentration of particles in the systems. Therefore a concentration parameter is defined as:

$$\zeta = V_{\circ} n \tag{3.3}$$

where $V_{\circ}$ is the volume of a particle in dilute suspension, and n is the number density of particles [39, 46]. Measurement of the hydrodynamic radius is complicated by the polymer-brush extensions on the particles which have the effect of enlarging the value; as a result, a direct parallel between ζ and the colloidal volume fraction is not straightforward. In these experiments, ζ is obtained by counting the number of particles in a 3D image stack. For low volume fraction suspensions, where the particles are highly mobile, an accurate acquisition of a 3D image stack is difficult. For these samples, the number of particles in a 2D image is counted, and averaged over several subsequent frames. To measure the number density of particles, a volume $L \times L \times dz$ is defined, where L^2 is the area of the square field of view and dz is the thickness within which the centers of the particles that appear in a 2D image are located. In our case $dz \approx 2a$, where a is the hydrodynamic radius of the particles. To test the accuracy of this 2D estimate for ζ the results obtained in 2D and 3D for an arrested sample are compared: the difference in ζ is less than 5%.

At higher concentrations when the particles become compressed, ζ can reach values much larger than unity. ζ is used to provide a self-consistent calibration for a sample with a given cross-linker-to-monomer ratio and should not be compared to the traditional colloidal volume fraction. Cross-comparing values from different samples is also not useful since particle structure, pH, and slight variation in synthesis can introduce changes from sample to sample making such a comparison arbitrary.

Nevertheless, I see phase transitions to occur for values of ζ within a range of 5 percentage points; for example, crystallization of samples starts when $\zeta = 0.55 \pm 0.05$. The parameter also provides information on the range of concentrations over which crystallization occurs for a specific sample, and allows us to roughly compare the trend between ranges of concentrations of different samples.

Chapter 4

Analysis tools and techniques

The image sequences are acquired as described in chapter 3. Samples are cleaned by repeated centrifugation and redispersion in deionized water and finally dispersed in solutions with adjusted pH which is centrifuged again for desired concentration. The ready sample is then sheared by vortexing it for 3 min, followed by degassing under vacuum until no bubbles form. This is then loaded onto the sample cell through either capillary forces when possible, or by pipetting directly. Imaging is done on a Leica SP5 microscope using 100x oil immersion objective. The LIF (Laser Induced Fluorescence) files from the microscope can be opened using Leica LAS AF Lite software obtainable online for free. I find it most suitable to use the ImageJ software from $http://rsbweb.nih.gov/ij/$.

4.1 ImageJ and LAS AF Lite

ImajeJ is a convenient to use software for data loading and saving in various formats - tiff, avi, jpeg and others. It can directly read LIF files and gives users flexibility by providing numerous loading options. When a LIF file is dragged and dropped (alternatively File > open), a dialog window appears. This is used to choose options such as what file types to load (image versus metadata) and whether to specify range for each series (which is important as memory is limited). When these have been specified, a second dialog opens with a list and preview of data to assist in selection (a snapshot of the window is shown in figure 4.1) . One can then choose which series to load, and in the next dialog window choose what range and increment for each series. Once the files are open, there are multiple options for noise reduction, cropping entire stacks, smoothing, subtracting, enhancing contrast, extracting sub-stacks and such. Additionally, one can obtain extra plugins (example *www.macbiophotonics.ca*) for further stack analysis.

The LAS AF Lite software is an attractive alternative. A front panel is shown in figure 4.2. I did not use it for analysis purposes, but did use it to open and check accuracy of files: I find it particularly useful in this respect due to its similarity to the LAS AF software on Leica Microsystems.

Pre-tracking adjustments

The data is usually smoothed, background subtracted, and contrast-enhanced before further analysis. This is then saved in tiff file format. This type of data treatment tampers with pixel information and is not appropriate if data analysis is dependent

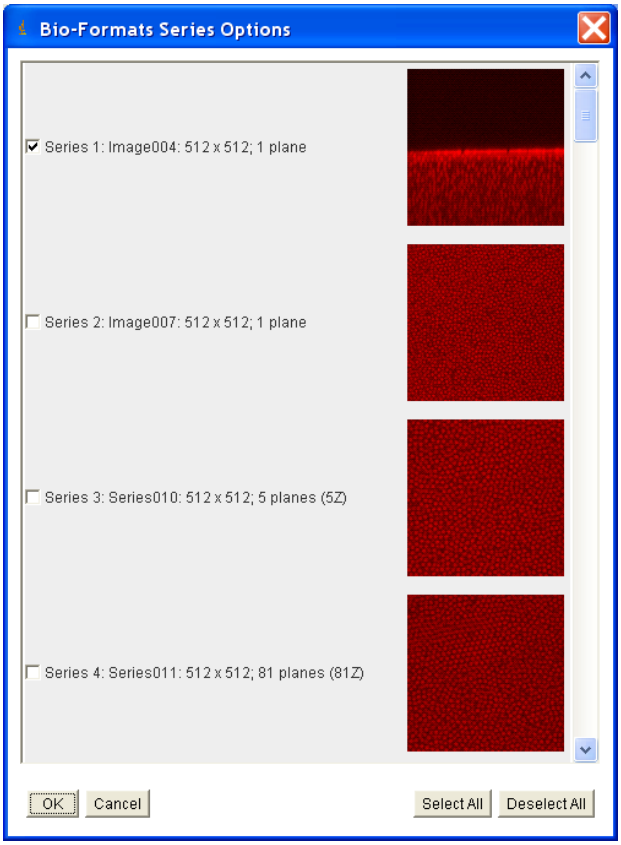

Figure 4.1: ImageJ dialog window.

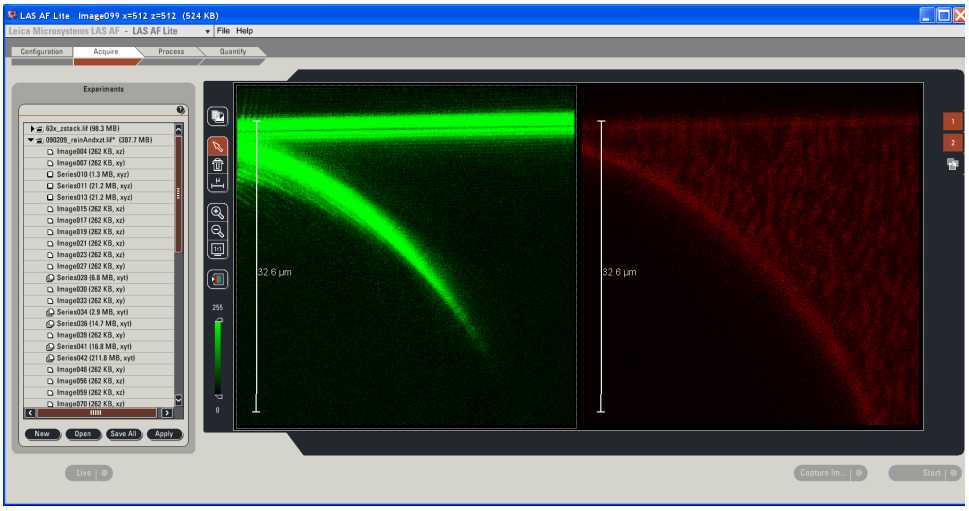

Figure 4.2: Front panel of the LAS LA Lite software for LIF file analysis.

on small position displacements. Nevertheless, the effects of such enhancements do not influence the results for the type of analysis reported in this thesis. Additionally, fluorescent images from microgel particles are characterized by irregularity in the pixel brightness hence finer analysis is intrinsically difficult.

4.2 Particle tracking tools

I use particle tracking software developed by Eric Weeks and John Crocker (IDL from here on) to analyze the data. A complete tutorial of how to use their software can be found at *www.physics.emory.edu/ weeks/idl/*. I have also applied a c tracking code (PluTarc from here on, short for Peter Lu Target-locking Acquisition with Real-time Confocal) [35].

The IDL codes employ a very different approach from the C codes. PluTarc is reported to give better in-plane (xy) resolution [35]. In addition, three-dimensional (3D) tracking proceeds in very different manners in the two cases. In IDL, an entire 3D stack is read and particles are identified in 3D in a single step via filtering using a 3D Gaussian. By contrast, PluTarc identifies bright spots in 2D by convolving with a 2D Gaussian and reconstructs the 3D image by asking the user to specify the number of frames a particle should appear in. In the latter case, one can control by how much a particle is allowed to deviate from a central position, and after how many planes the code should decide to split a bright continuum into two particles. Unfortunately, for the microgel particles in contention here, I have found this method to introduce extra error due to the inability to decide a fixed number of frames a single particle appears in. The deformability of the particles makes it particularly difficult to fix

the number, since this in most cases varies from particle to particle. The IDL set of codes also provides additional software to do further analysis of tracked data such as to check accuracy of tracking by plotting distributions and the set of codes are fairly self-sufficient.

4.2.1 Summary of tracking steps

Here I discuss the general tracking steps followed when using the IDL and PluTarc softwares. Specific parameters vary from sample to sample. But the general procedure remains the same.

IDL

- From ImageJ, save stack as a continuous image sequence (8 bit).
- Use MATLAB to construct image stacks. I do this in two steps. First I rename the files using *batch_maker*.

  $>> batch\_maker(instem, frames, stacks, outstem)$

  I then use *make_stack*, another MATLAB code, to put the images into stacks (the codes are given in full in appendix A).

  $>> make\_stack(stem, frames, stacks, outstem)$
- In IDL, follow instuctions given at *www.physics.emory.edu/ weeks/idl/three_html* where detailed illustrations and examples are given.

  An example 2D image superimposed with its tracked positions is shown in figure 4.3.

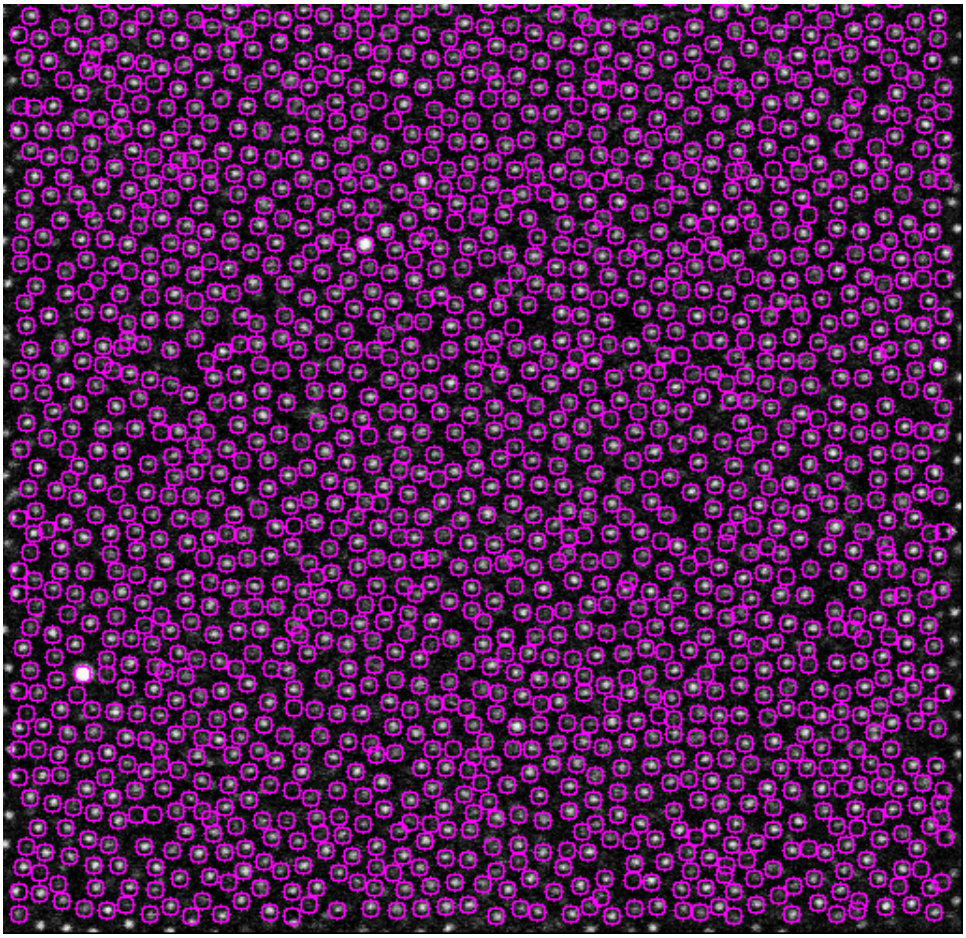

Figure 4.3: The image shown is tracked using IDL. Circles are centered at tracked positions.

PluTarc

- Using ImageJ, save the stacks as image sequence. Name them appropriately so that it is easy to read them, for example using the series name. Number them starting from 1. Make sure they are in RGB.

- Rename the files to match the naming format PluTarc can decode. The code
  $>> batch\_maker = (instem, frames, stacks, outstem)$
  in MATLB does the job.

- Determine diameter in pixel using IDL. To do this load an image using
  $> a = read\_tiff('filename.tif')$
  $> tvscl, a$
  mark two points. Do this for the brightest and repeat several times.

- From PluTarc use the *plu_centerfind* program to find center positions for the particles. Required parameters can be seen by entering an empty string. Once parameters are adjusted and satisfactory results are obtained, do for all stacks. The program allows you to do multiple stacks at once.

- From PluTrac use *plu_link*3*dt* to link particles in 3D. The program builds 3D data from 2D positions by linking bright spots in the 2D images in successive frames of a stack. The accuracy relies highly on the parameters supplied.

- Use *plu_struct*3*dt* to plot the $g(r)$. This is a good way to check if the parameters used are reasonable.

- In MATLAB import the xyzt data. Rearrange the columns so that the time

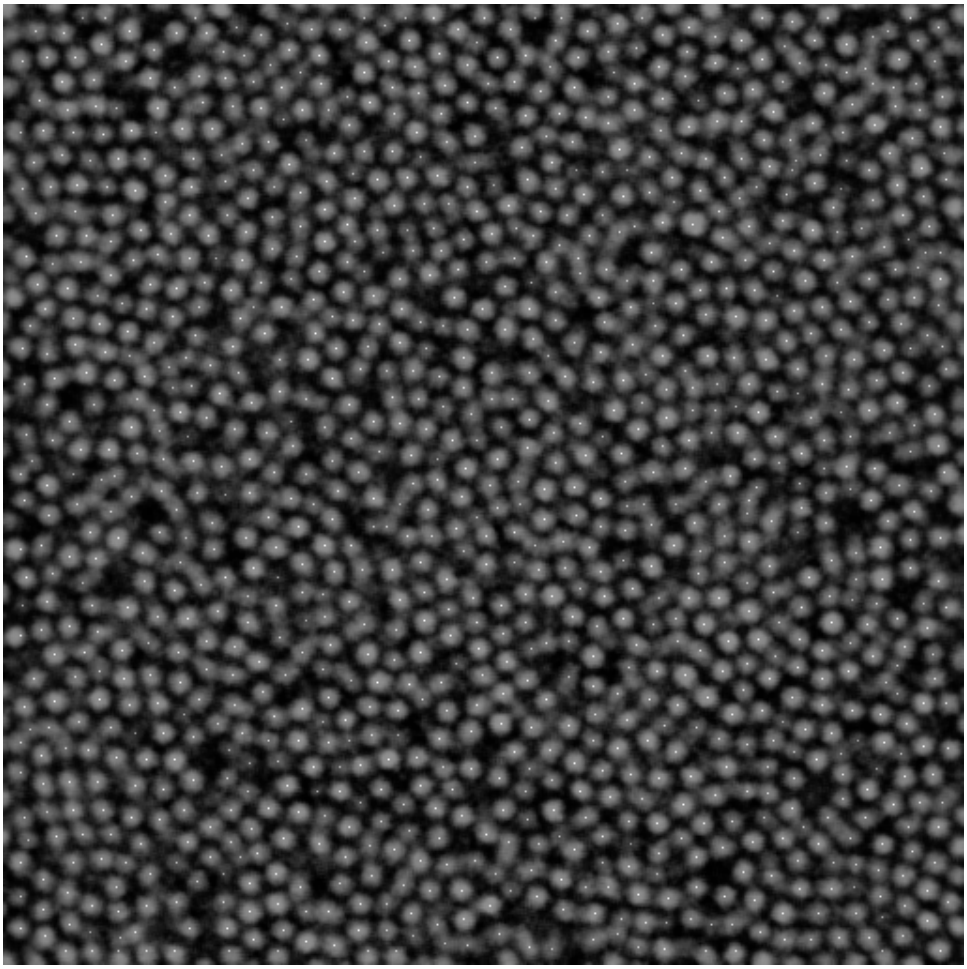

Figure 4.4: Image of a microgel suspension at $\zeta = 0.8$ superimposed with center positions of particles (white spots) as identified by *plu_centerfind*.

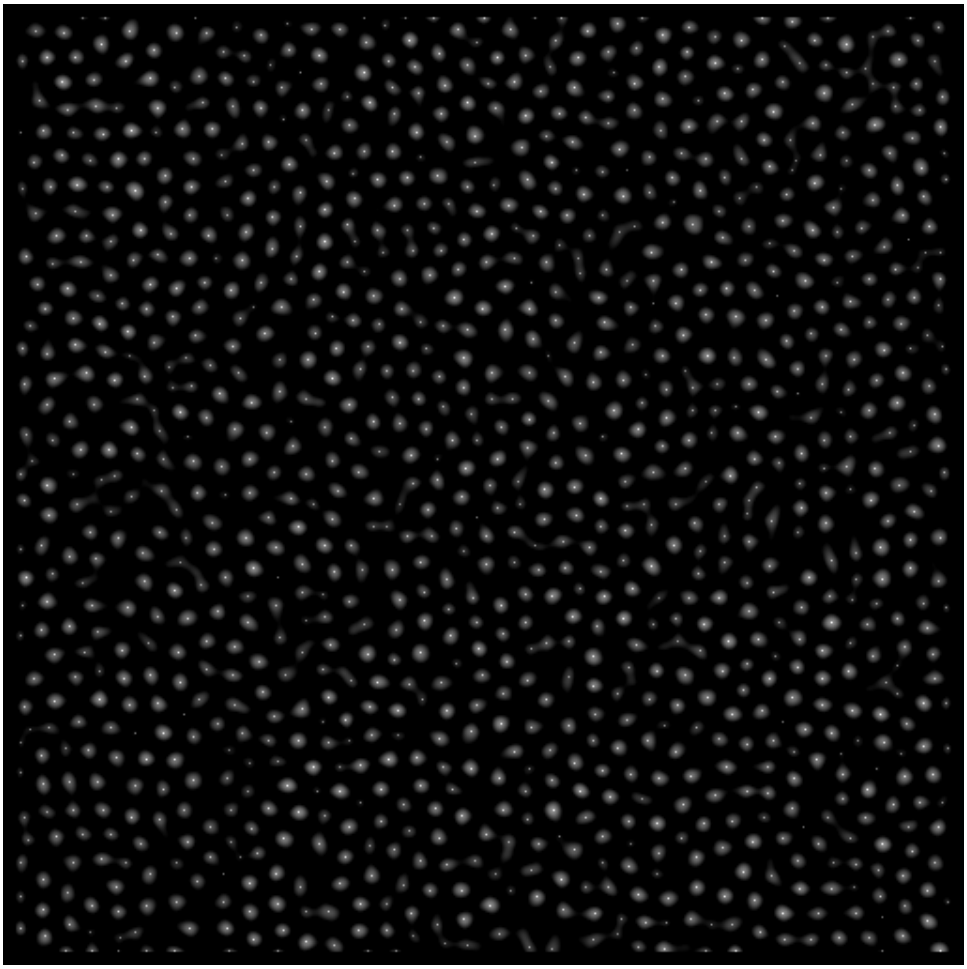

Figure 4.5: The image in 4.4 filtered with a Gaussian (width is radius of particles 0.5μm).

column is the last column.

- Make sure that *track.m* is copied to the current directory of MATLAB (which should be where the tracked files are). If not, MATLAB will try to use the built-in function *track.m* and will generate error.

- Create a parameter structure

  $>> Param = struct('mem', 'dim', 'good', 'quiet')$

  The meaning of the variables is given in the *track.m* file

- Execute tracking

  $>> tr = track(xyzt, maxdisp, param)$

  and save the data.

4.3 Tracking: linking in time

Once the positions of the particles are identified, linking of the positions in a time sequence is done by calling *track.m* or *track.pro* corresponding to the MATLAB and IDL versions of the tracking routine. The discussion of the variables required in tracking are described in the codes. In general, one needs to specify the dimension of data (2D or 3D), the amount of displacement allowed from one frame to the next, the minimum number of frames a particle must be identified in to be retained in the tracked data, and the criteria to differentiate particles appearing in the same position over time (such as the number of frames between them). This gives a fair amount of flexibility and control over the quality of tracks produced. Especially, the amount of maximum displacement allowed should be chosen carefully to capture the full extent of

displacement while making sure that the program does not confuse different particles: a good starting point is the radius of the particles. In case of a highly mobile sample, one can relax the value to the diameter or bigger. For an arrested sample, or a sample showing caged dynamic behavior, the maximum displacement is usually much smaller than the radius, and the likelihood of confusing different particles is high; hence care must be taken in choosing parameters that can still reflect the small displacements that exist. The trajectory of a particle is shown in figure 4.6. The black squares represent the position of the particle in each frame. The particle executes a random motion, moving by only a hundredths of a micron from frame to frame - this is a dense sample.

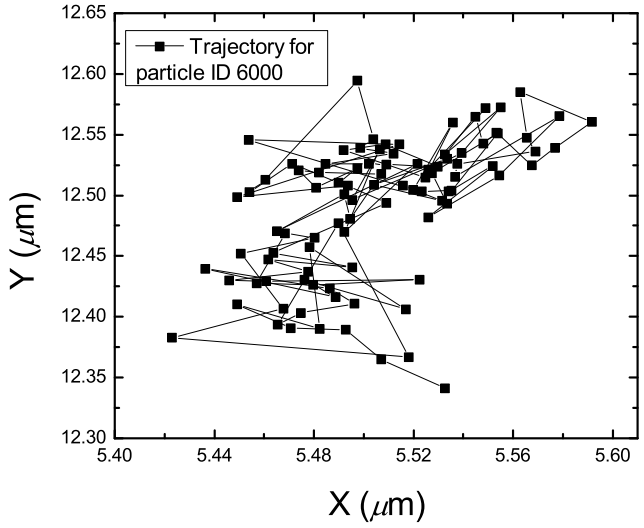

Figure 4.6: Trajectory of a particle inside a dense sample. Each square point represents a frame. Displacement from frame to frame is on the order of hundredth of a micron.

One way of checking if all the displacements for the particles have been appropriately captured is by binning the distributions and checking if they go to zero.

4.3.1 Displacement distribution

The tracked positions have one common characteristics: both the PluTarc and IDL codes give a bigger error in the z than in the xy-direction. This originates from data acquisition which is intrinsically skewed: the confocal goes through the xy planes using the scanning mirrors while the piezo is used to change z-position (see chapter 3). Hence the distribution of data in the z as measured by calculating displacement for a fixed time step is wider than those measured for the x and y directions. This is shown in figures 4.7 and 4.8.

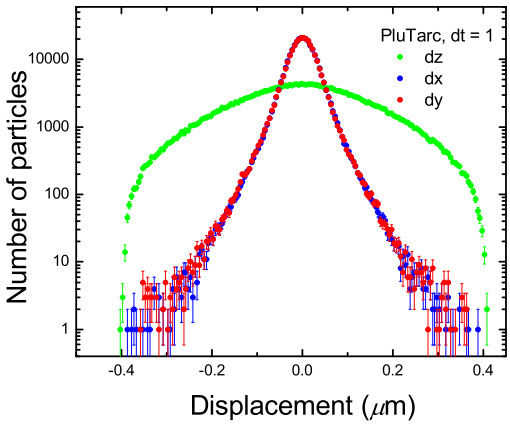

Figure 4.7: Displacement distribution of particles tracked with PluTarc. Time step is dt = 1 frame. Half Width Half Max (HWHM): xy = 0.06, z = 0.3.

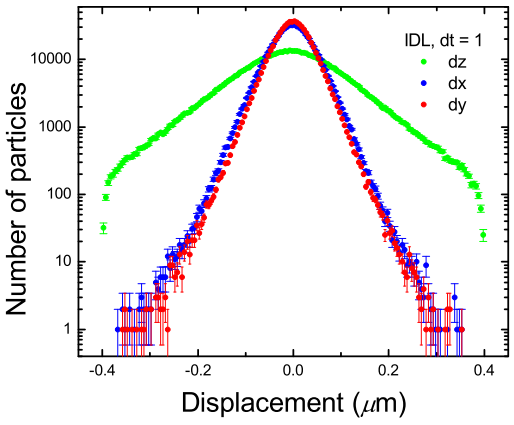

Figure 4.8: Displacement distribution of particles tracked with IDL. Time step is dt = 1 frame. Half Width Half Max (HWHM): xy = 0.075, z = 0.188.

Additionally, the Half Width Half Maximum in z is larger from the PluTarc code. This is the result of inaccuracy while linking of particle positions from 2D images to create 3D information. The tracking of positions in the IDL improves precision, specifically for the microgel particles, since 3D convolutions are done directly on the

stacks. Comparing tracking routine accuracy based on this criterion may sound questionable, given that we do not have information about how much the particles are moving and since either routine could possibly be telling the truth (actual larger displacement in z). Regardless, we can do a quick check for this by comparing displacements in xy and in z for each routine. The ratio of HWHM for IDL (in x or y versus z) is 0.4 while this value is 0.2 for PluTarc. The closer the value is to 1, the more accurate the tracking is, since the particles should not differentiate between the x, y, and the z axes (gravitation here is negligible).

4.3.2 Mean squared displacements (MSD)

The tracked file contains particle positions, with corresponding particle ID, arranged in time. The mean squared displacement of particles is then calculated by going through all initial and final time combinations constrained by a given delay time. The displacements are calculated for all the particles, squared, summed, and averaged. This is repeated for all the possible delay times. Different delay time schemes are possible. For example, the MSD routine in IDL developed by John Crocker automatically choses logarithmically spaced delay times. I have written a code that allows one to specify a random time matrix and calculates the MSD constrained by the random time steps. This is useful when one has a rare data that is difficult to repeat but from which some time steps are missing (this reason is the actual motivation for writing this code). The steps for doing randomly-spaced delay time MSD is given below. The complete code is given in appendix A.

- Load the de-drifted version of tracked position file to MATLAB.

- Create an array containing the order of the frames (this should contain monotonically increasing values)

- Find the length of the track file

  $>> length = size(trb(:, 3));$

- Reassign the time column

  $>>$ for $m = 1 : length$

  $trb(m, 3) = (array(trb(m, 3)) - 1) * timeStep;$

  end

  Where timeStep is the time step in real time (usually seconds or milli seconds).

- Calculate the MSD with modified code. The first

  $>> msd\_random = mel\_msd(trb, timeStep);$

- Open file and delete zero rows.

- Average the MSD values.

  $>>$ for $n = 1 : end$

  $msd\_random(n, [1 : 5]) = msd\_random(n, [1 : 5])./msd\_random(n, 6);$

  end

- Save files

  >> Save 'msd_random.txt' msd_random -ascii

A mean squared displacement of a sample close to the glass state is shown in figure 4.9. The mean square is an increasing function of time in most cases. But

occasionally, we can see it going down due to a sudden arrest induced by events such as crystallization and gellation.

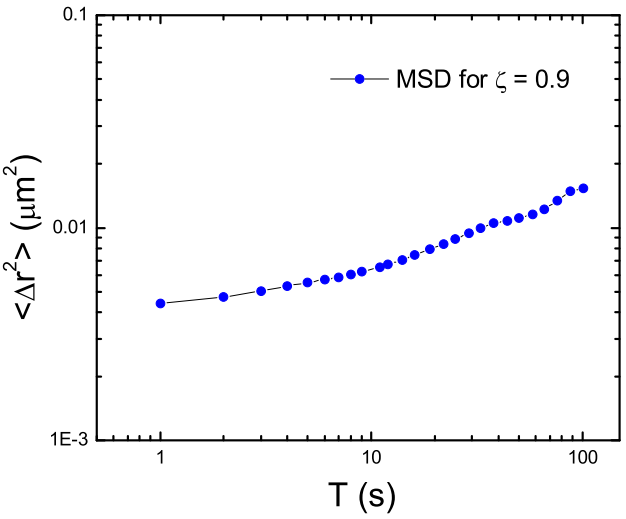

Figure 4.9: The mean squared displacement of a sample at $\zeta = 0.9$.

MSD in 2D vs 3D

Tracking in 2D and 3D are different for a number of reasons. Frist, the resolution in z is not as good as that in the xy-plane. Additionally, 3D stacks take longer to record hence their time resolution is lower compared to that of 2D image sequences. In figure 4.10, the MSD of two samples is shown for 2D and 3D imaging. MSD from 3D data calculated by ignoring the z-component is lower than the corresponding 2D data. This, perhaps, is due to the accumulation of more distance due to finer time steps in the 2D case. At longer times, the two MSDs give the same value since time is no longer a limiting factor in data acquisition.

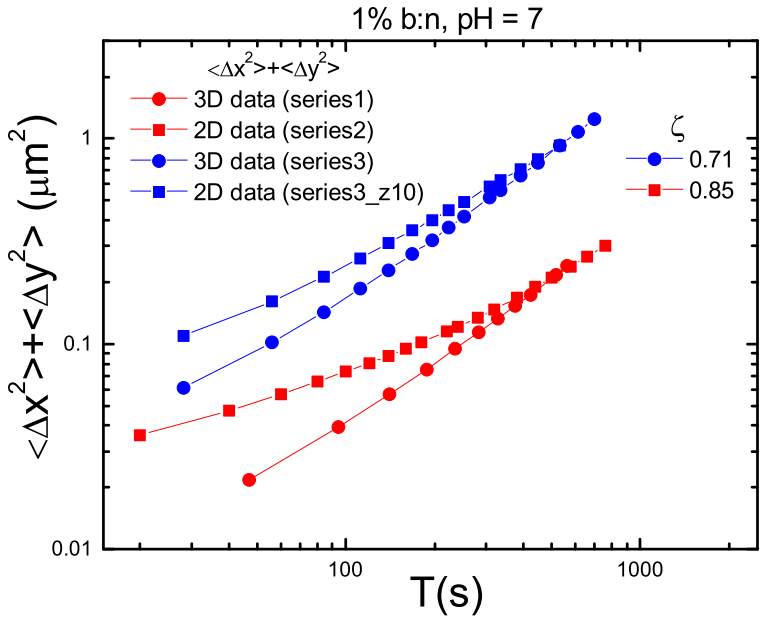

Figure 4.10: MSDs in 2D and 3D compared.

De-drifting

Data usually contains drift for a number reasons such as drying, convection, or imaging stage vibrations. It is thus essential to check each data for this undesired artifact and remove it from the data before further analysis. This is done by comparing center of mass positions of consecutive images. If the motion of the particles is random, as it should be, one should not expect the center of mass position to change very much after taking noise into consideration. If the center of mass position changes by a large amount over a single time step, then it is a clear indication of the presence of drift. To remove drift, one can subtract the displacement of center of mass from displacement of each particle. The MSD shows a decrease once the data is de-drifted.

This is shown in figure 4.13.

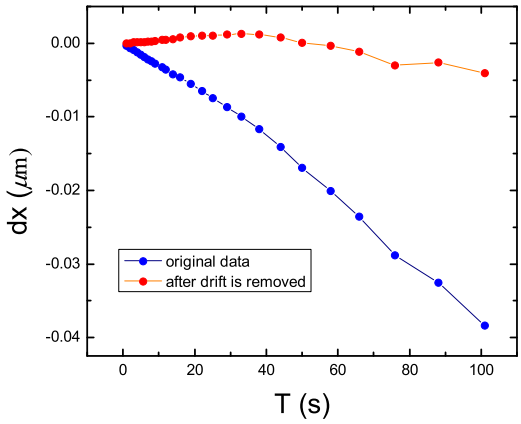

Figure 4.11: Drift in the x direction (blue) and after de-drifting (red).

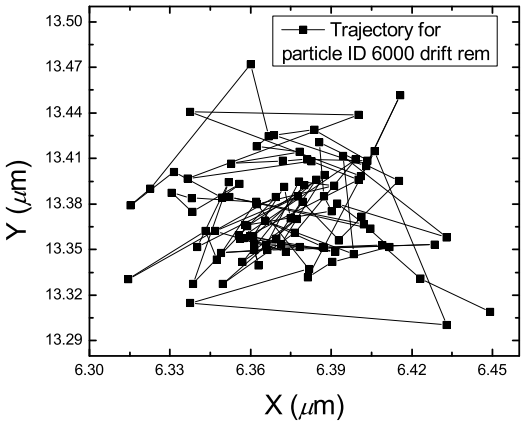

Figure 4.12: The trajectory shown in 4.6 after removing drift.

The error in the z position is bigger than the in-plane error as discussed. To reduce error in analysis, we calculate only in plane MSD from here on.

4.3.3 Single particle MSD

Single particle mean squared displacements are particularly useful when one desires to differentiate particles based on a dynamic criterion. Not only does this help in differentiating particles at a specific time, but it also can easily illustrate the evolution over time of the dynamics. This is most convenient when one deals with data taken over a period of several hours and that constitutes short movies separated by a time gap. The individual particle MSDs of each movie can then be used to capture how heterogeneous the dynamics is within each movie, and how this evolves over time. The ensemble averaged MSD does not have any information on heterogeneity within the same movie. In addition, a visual representation of the dynamics in the system

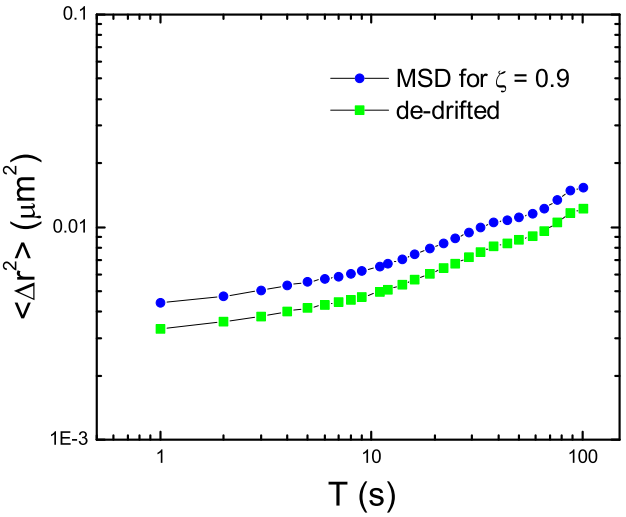

Figure 4.13: The mean squared displacement of a sample de-drifted. $\zeta = 0.9$.

is possible using the single particle MSDs. To do this, one can use cutoff MSD values to sort particles and to render the data accordingly. The steps for color coding the particles this way is given below.

- Use the tracked file to compute single particle MSDs. This is done in MATLAB using

  $>> msd\_sing = msd\_single(tr, time\_step)$

- Use tracked data and single particle MSD for color-coding in MATLAB

  $>> colorcode = crystalfinder(tr, msd\_sing)$

- In IDL, bin the colorcode file using *bin_colorcode*

  $> code = bin\_colorcode(colorcodedata)$

- Select specific time of data and save

$> w = where(colorcode(x, *) = time)$

$> code\_t = code(*, w)$

- Load color code of specific time *code_t* to MATLAB.

  $>> xy = code\_t(:, 1:2);$

  $>> xy(:, 3) = 1;$

  $>> code = code\_t(:, 4);$

  $>> Showbeadscolorcoded(xy, code, min\_x, max\_x, sizeofsphere, 0.5, 1.5, 3);$

- The codes *msd_single*, *crystalfinder*, *bin_colorcode*, and *showbeadscolorcoded* are given in appendix A.

An example of a 2D time sequence with corresponding color coded figures representing dynamical evolution is shown in figure 4.14. Yellow coded particles represent particles with single particle MSD < 0.1.

4.3.4 Particle imaging velocimetry (PIV)

This technique is usually applied for systems which have lower than particle-level resolution. I tried the technique on microgel particle suspensions to see if it would be easier to capture any displacement or velocity correlations. An example is shown in figure 4.15 where an image is superimposed with the corresponding velocity vectors. A correlation between these vectors can be used to obtain information on cooperativity in the system. Regardless, this means losing particle level resolution as analysis is done by partitioning the image into subregions and averaging over particles within the subregion in consecutive images.

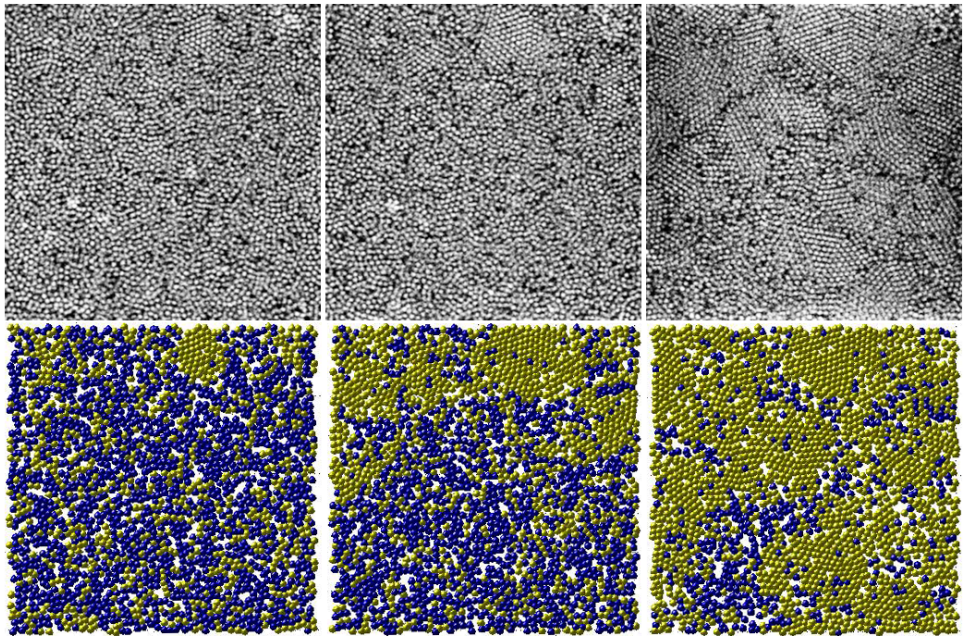

Figure 4.14: Time sequence of a microgel suspension with corresponding dynamical behavior represented by color. $\zeta = 0.8$.

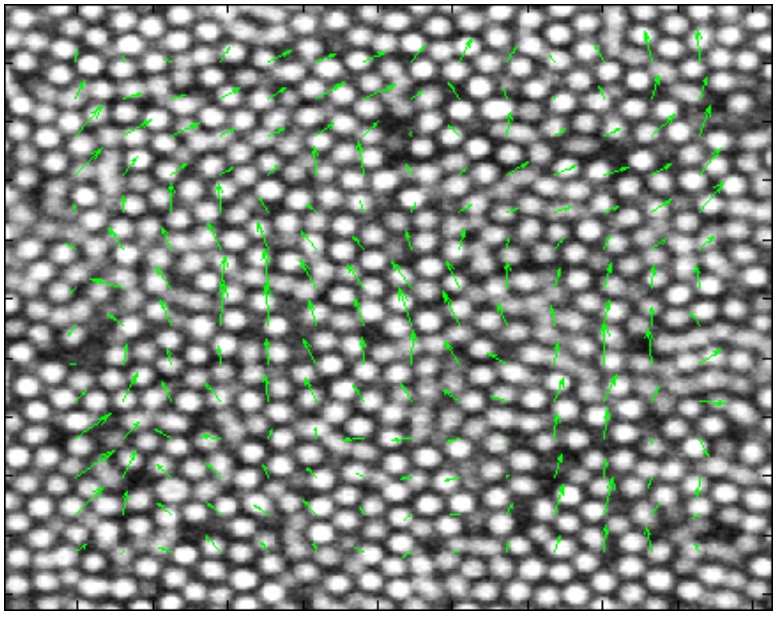

Figure 4.15: Velocity vector field superimposed with a still image at a given time.

4.4 Structural analysis

In this section we discuss some of the structural analysis applied to the microgel systems. The analysis is used to check the type of structure and order, if there is any, in the suspension. The structure factor, $s(q)$, and the pair correlation function, $g(r)$, are the main tools. Three-dimensional (3D) visualization of the suspensions is achieved through rendering.

4.4.1 Pair correlation function, $g(r)$

The pair correlation function gives the radial probability of finding a particle a distance away from an arbitrary particle at the center. For a randomly packed system of colloidal particles, this simply gives a function of distance that has peaks at well defined values [6]. The first peak appears, as one would expect, at a distance equal to 2 times the radius of the particles (this is true only for monodispersed particles). The function can be used to test presence or absence of order in a packed suspension; order manifests with peaks at specific values. The location and size of these peaks is characteristics of how the particles are arranged in the crystal (FCC, BCC, etc). Further discussion in this direction is presented in chapter 6. A set of $g(r)$ plots for glassy samples at different concentrations is shown in figure 4.16.

4.4.2 Vornoi tesselations

The distribution of volume among the particles of the suspension can be obtained from the voronoi tessellation. Literally speaking, this gives the region of space that is closest to a given particle than any other particle. Clearly, the denser the system, the

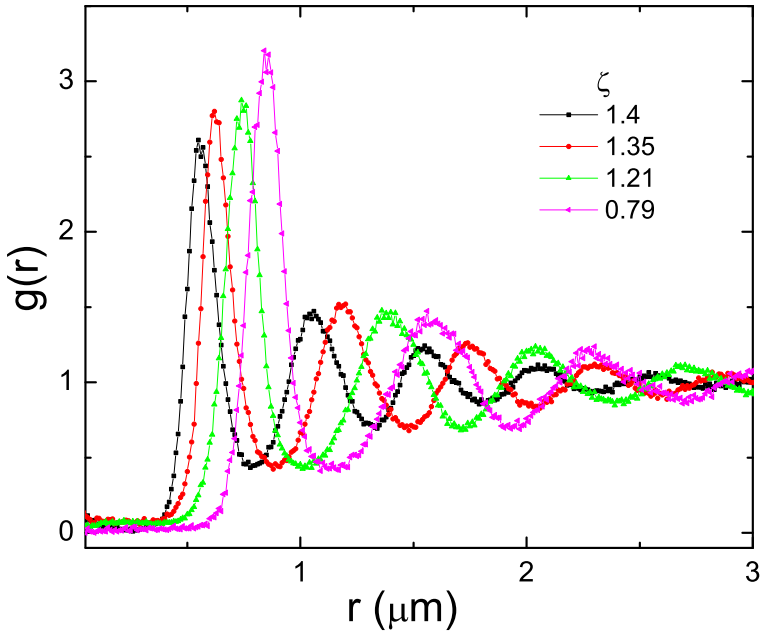

Figure 4.16: A set of $g(r)$ plots for samples at varios concentrations in a disordered glassy state.

smaller the average voronoi volume and vice versa. This trend can clearly be seen in figure 4.17 for samples whose $g(r)$ is shown in figure 4.16. This way of visualizing the data could be useful to extract information about regional variations (say by color coding according to voronoi volume) in density which can be in turn caused by a number of factors such as stress variations. Voronoi areas and volumes can also be used as a visual aid in 2D and 3D to illustrate order or disorder (see figure 4.18).

4.4.3 Structure factor, $s(q)$

The structure factor is the pair correlation function in reciprocal space [6]. The structure factor in two dimensions is a convenient measure of the degree of order: information on both translational and orientational order can be obtained. The quantity

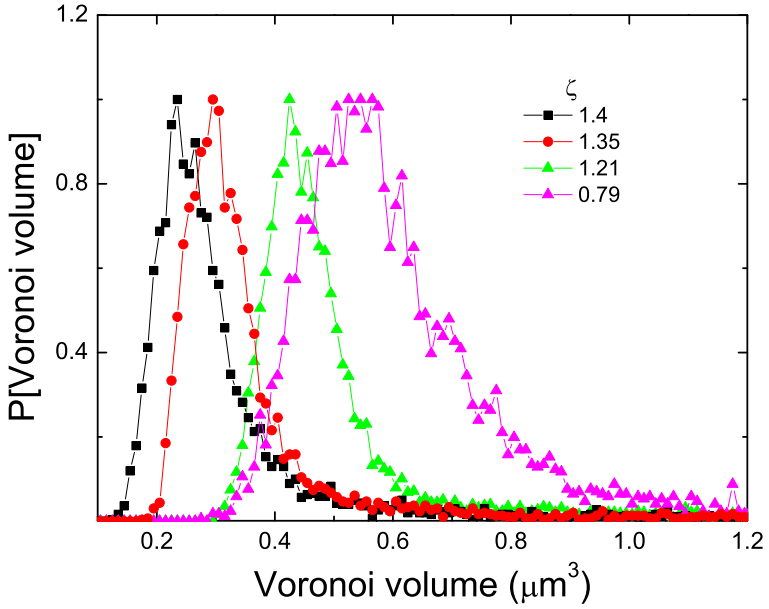

Figure 4.17: Voronoi distribution for samples as a function of concentration.

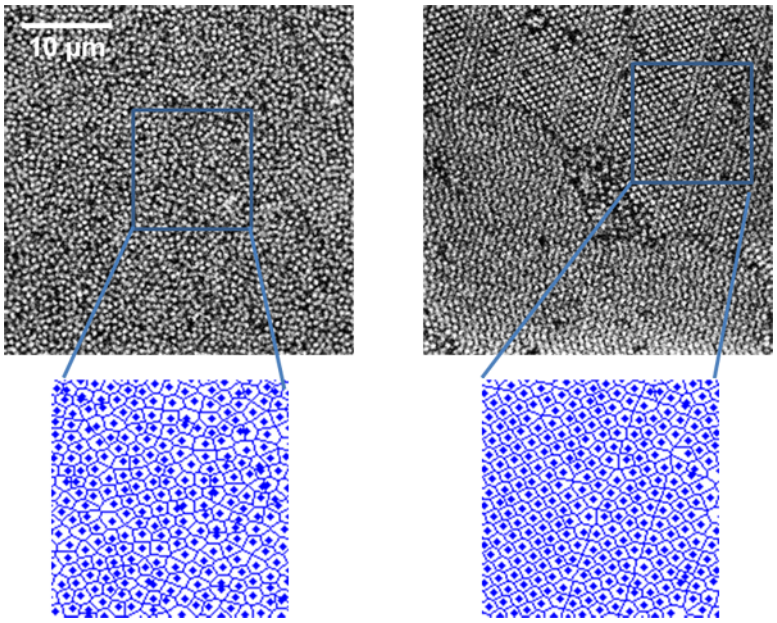

Figure 4.18: Voronoi area distribution as a function of order.

can be computed from tracked positions of N particles using equation 4.1.

$$S(q) = \frac{1}{N}\left|\sum_{j=1}^{N} e^{-i\mathbf{q}\mathbf{r}_j}\right|^2 \tag{4.1}$$

where $\mathbf{q}$ is a 2D meshgrid of points and $\mathbf{r}$ is the position of a particle of index j with respect to a reference point. The contributions from each particle for each grid point are added together and normalized. Further discussion of this parameter with regard to crystal structure analysis is given in chapter 6.

4.4.4 Bond order parameters

A discussion of the bond order parameters is given in reference [64] and [72]. Orientational order is measured by the spherical-harmonics used to describe the structure: specific structures require a specific combination. This results in unique orientational order parameters for each stacking style. For a vector bond connecting two elements, the parameter in 4.2 is computed using the values of θ and ϕ describing the vector with respect to an arbitrarily chosen but fixed polar coordinate system. The contributions from all bonds are added together and averaged.

$$Q_{lm}(\mathbf{r}) = Y_{lm}(\theta(\mathbf{r}), \phi(\mathbf{r})) \tag{4.2}$$

where Y_{lm} is the spherical harmonic function. In our case, the bond order parameters calculated from tracked particle positions of colloidal suspensions are compared with the theoretical values to determine the most likely crystal structure in the colloidal systems.

4.4.5 Three dimensional visualization: rendering in Aqsis

Rendering of colloidal structures is fun and artistic. Knowing that it is a macroscopic representation of real microscopic world makes it even more exciting. Also, it is very useful for visualizing how the colloidal particles are arranged in a suspension, for example, to directly observe stacking styles of crystals. Rendering requires us to identify positions that belong to specific particles in an ensemble; this can be quite challenging.

An example of a 2D section of a z-stack is shown in figure 4.19. The stack contains crystallites with particles arranged in a square lattice. The position of the crystallites is identified by direct inspection and guesstimation of their positions from the 2D images. The approximate positions are then used to locate the particles in the tracked file. A script is then generated via MATLAB that identifies different subgroups with different colors and shapes. The rendering proceeds in several steps.

- Identify (by inspection) particles that belong to crystals using ImageJ.
- Track the stack.
- Using the approximate positions obtained from ImageJ, find the indices of the particles that belong to crystallites in the tracked file.
- Use $xtalsPos.m$ to extract the actual data points for crystallites. The MATLAB code is given in appendix A.
- Sort the crystal position data using origin.

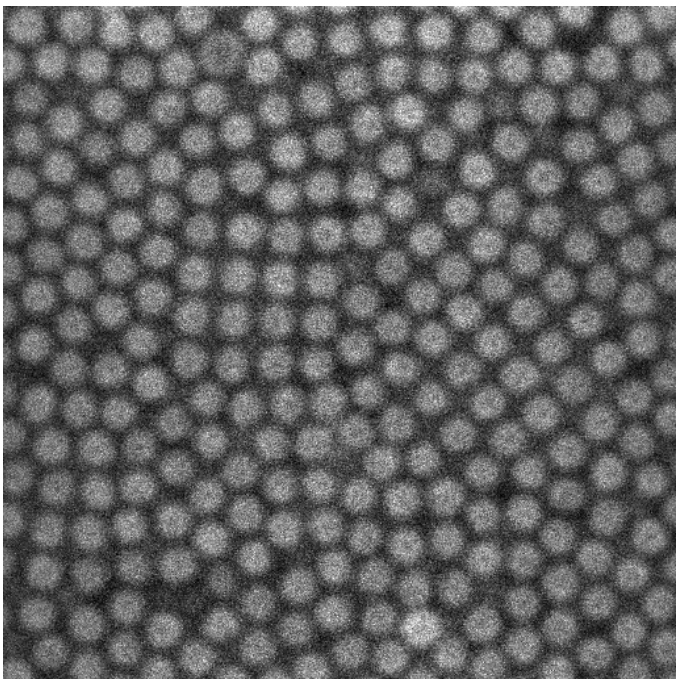

Figure 4.19: A 2D image from a z-stack.

- Create a *.rib* file for crystal position using *sorted_xtal.m*. The code is given in appendix A.

- Create a *.rib* file for entire stack using *sorted.m*.

- Create an aqsis file. Save using $.RIB$ extension from the dialog window. An example file is given in appendix B.

- Render by calling aqsis from the command prompt.

  $> aqsis - d\ filename.rib$

  The option -d opens a display window during rendering.

The rendering of the data shown in 4.19 is shown below in figures 4.20, 4.21, and 4.22 for different contrasts, angles, and positions.

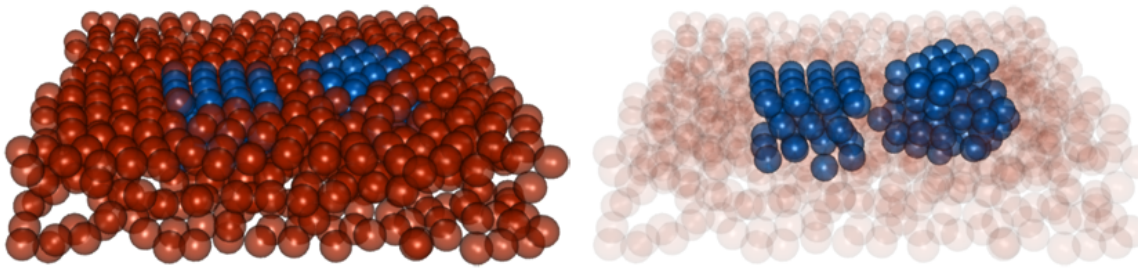

Figure 4.20: A rendering of the data shown in figure 4.19.

The crystal subgroup is rendered not only in color but also in shape, as seen in figure 4.21.

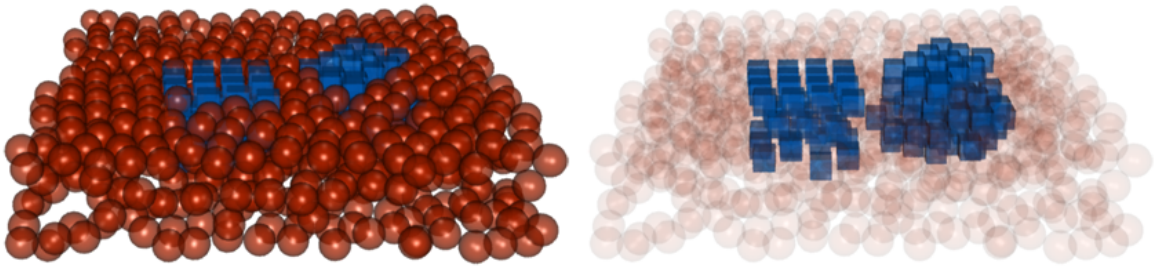

Figure 4.21: A rendering of the data shown in figure 4.19 with the crystals rendered in square blobs.

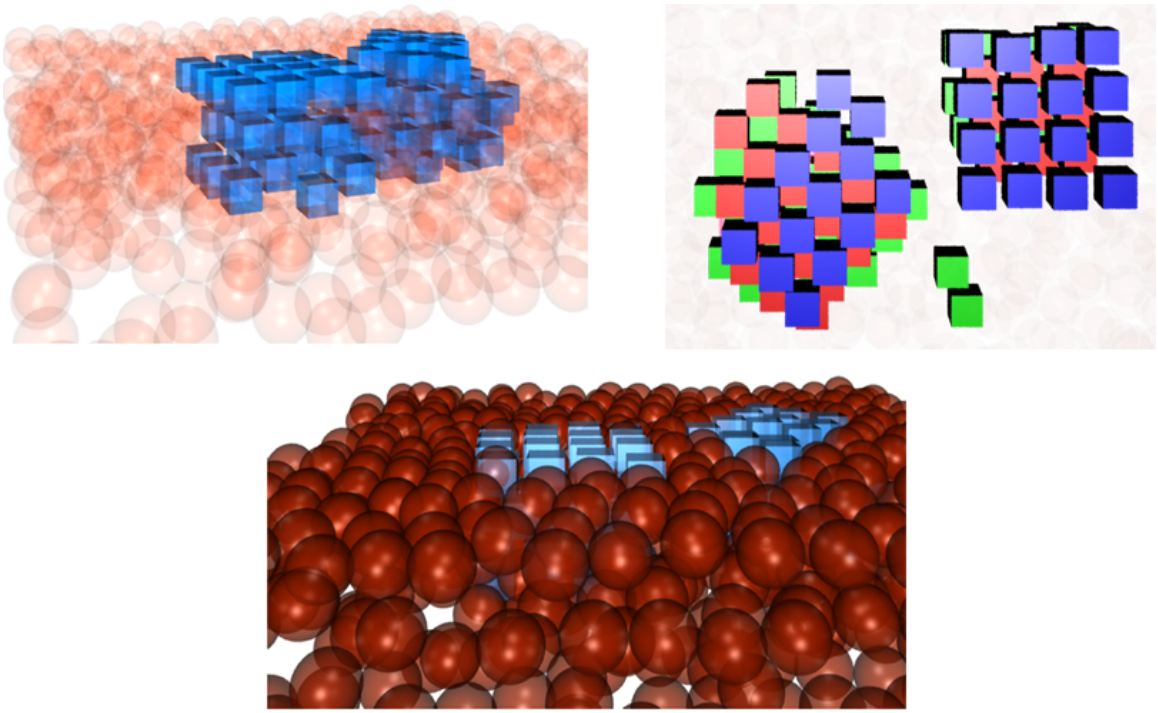

Figure 4.22: A rendering of the data shown in figure 4.19 seen from different angles.

Chapter 5

pH dependent evolution of structure and dynamics in microgel suspensions

5.1 Introduction

As discussed earlier, the phase behaviour of suspensions of such pNIPAm-based particles depends strongly on temperature, pH and ionic strength. The response of the microgels to such external triggers can be exploited: For instance, size changes induced by a change of temperature can be used to switch between the liquid and crystalline states of the suspension [37, 25, 43]. Thermal quenching protocols have also been used to study the physical ageing in microgel glasses [18, 9, 79, 51]. The interparticle potential of p(NIPAm-co-AAc) microgels is also influenced by the pH and ionic strength; at low pH the acrylic acid groups are largely protonated, and

uncharged, whereas they become more charged due to deprotonation as the pH increases. Added salt can screen these charges and reduce the electrostatic repulsion. An additional effect occurs at low pH; hydrogen bonds can form between protonated carboxylic acid groups and acrylamide moieties of the pNIPAm. This leads to a weak attraction, with a depth of attraction of approximately 0.5 k_bT, as characterized by measurements of the 2D pair correlation function [8]. Observations of concentrated p(NIPAm-co-AAc) suspensions at pH values between 3.0 and 6.0, after a waiting time of several weeks, have shown that pH plays an important role in determining the structure of the final state of these systems; suspensions at low pH age to form crystals over a broad range of concentrations, while at neutral pH they remain fluid-like and form glasses at sufficiently high concentrations. The transitions from an initially fluid state to a final solid-like state have not been studied in detail. It is thus essential to examine how both structure and dynamics evolve during the course of the transitions.

By directly observing the systems both at low pH, where the particles are weakly attractive and at neutral pH, where they are purely repulsive, using 3D confocal microscopy, we investigate the influence of the inter-particle potential on the temporal evolution of microstructure and the associated changes in single particle dynamics. At low pH, an initially fluid-like system slows down gradually due to the formation of crystalline structures. Nucleation occurs homogeneously throughout the system and does not appear to be localized at sample boundaries. We show that the freezing transition from the disordered fluid-like state to the solid-like crystalline state is a nucleation-limited process which can take up to a few hours to complete. By contrast,

at neutral pH, a fluid-like system retains its disordered structure, characterized by a lack of long-range order, throughout the duration of the experiment. In this case, the dynamics are governed solely by the concentration of the particles and do not depend on the time since the initial quench. We provide detailed information on the evolution of these systems by directly observing the structure of the suspensions and the dynamics of individual particles as a function of time.

5.2 Results and discussion

At low volume fractions, microgel particles behave effectively as hard spheres [59]. However, at higher concentrations, the microgels must shrink. This becomes apparent in confocal microscopy images, where we observe a significant reduction of the particle size upon increasing the concentration, as shown in the image series in figure 5.1 (a) and (b) for samples with cross-linker to monomer ratios of 10% and 4%, respectively at pH = 3.3. The samples with the highest concentration are prepared from dilute suspensions using dialysis against a dextran solution with an osmotic pressure of ≈ 20 kPa; the lower concentration samples are obtained by dilution of these concentrated samples. The significant difference in softness between these samples becomes apparent already during sample preparation, as particles with a cross-linker to monomer ratio of 4% shrink more than those with a ratio of 10% even though the same osmotic pressure is applied. This difference is evident when comparing the most concentrated samples in figures 5.1 (a) and (b). A similar trend in size change of particles with concentration is seen in all our other samples for a range of cross-linker to monomer ratios. Such deswelling of microgels is also observed in other situations; for example,

when a large and soft microgel is introduced into a crystalline array of smaller and stiffer particles, the large microgel can shrink to conform to the crystal lattice [28].

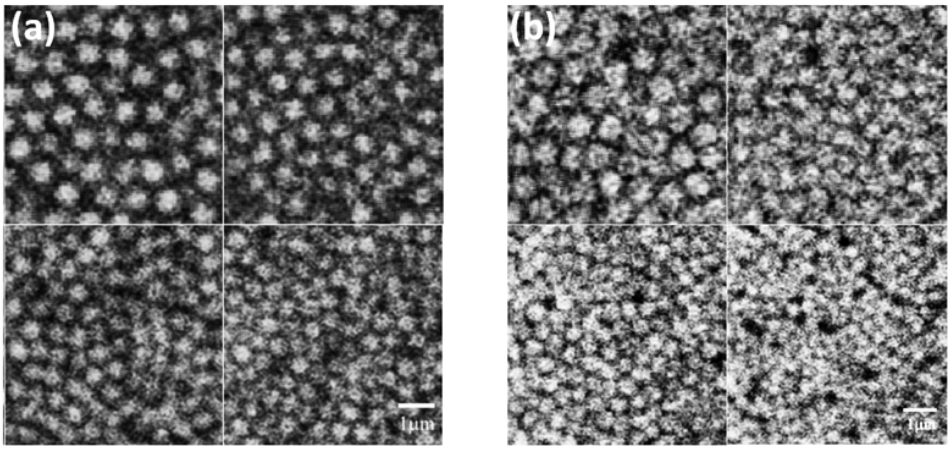

Figure 5.1: Microgel particles imaged at progressively higher concentrations at pH = 3.3. The particle size decreases systematically and the core shape remains approximately spherical. (a) Particles with cross-linker to monomer ratio of 10% for ζ = 0.79, 1.21, 1.35 and 1.40. (b) Particles with cross-linker to monomer ratio of 4% for ζ = 0:61, 1.1, 2.1 and 3.3, respectively. The highest concentration samples are prepared by dialysis against a dextran solution with an osmotic pressure of $\approx$ 20 kPa.

To quantify this deswelling of particles and the corresponding suspension structures, we track the positions of microgel particles in the confocal images and calculate the 3D radial pair correlation function, $g(r)$, which reflects the probability of finding a particle at a distance r from the center of any arbitrary reference particle [6]. The position of the first peak in the pair correlation function corresponds to the average distance to the nearest neighbor. We find that the position of the first peak, r_1 , decreases with increasing number density n as shown in figure 5.2. For isotropic deswelling r_1 should decrease as $n^{-1/3}$. Our observations are consistent with this expected scaling as illustrated by the solid line of slope $-1/3$ in figure 5.2 for the sample with cross-linker to monomer ratio of 4% at pH = 3.3 and 7.0. At high pH,

the number density is lower since the particles are bigger.

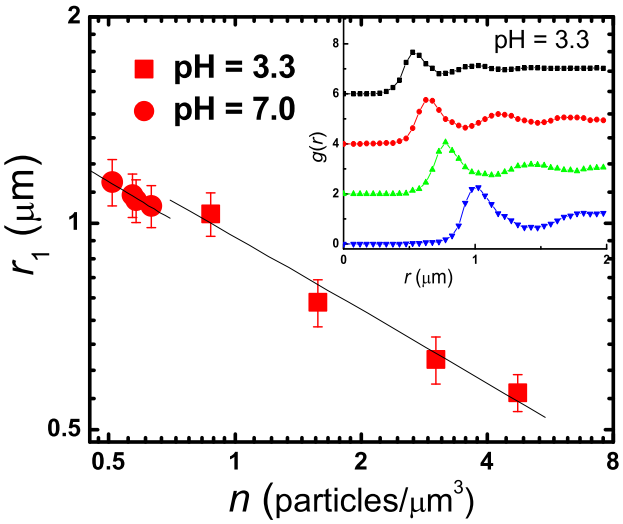

Figure 5.2: First peak position of $g(r)$ plotted as a function of number density, n, for the sample with cross-linker to monomer ratio of 4% at pH = 3.3 and 7.0. The solid line shows a power law with exponent $-1/3$ for comparison. Inset: radial pair correlation functions, $g(r)$, for the sample at pH = 3.3; curves are offset in increments of 2 for clarity.

Our microgel particles exhibit a soft repulsive interaction potential; by changing the pH from neutral to acidic, an additional attractive interaction between the particles is introduced. Here we make use of this tunability to investigate the effects of the inter-particle potential on the dynamics and structure of these suspensions. The system follows distinct routes to dynamic arrerst: At low pH, attraction driven crystallization dominates the evolution in the dynamics, while at neutral pH the evolution is dictated by concentration. The dynamics can be quantified by computing the mean-square displacement (MSD), $\langle \Delta x^2(t) \rangle$ of the particles from image sequences acquired at the two different pH levels. For the attractive suspension, at short lag-times, the MSD increases linearly in time, thus indicating a diffusive behaviour. At

increasing lag time, the sample reaches an arrested state where the MSD exhibits a plateau due to crystallization, as shown in figure 5.3(a) for a sample at pH = 3.3 and $\zeta = 0.65$. By contrast, the purely repulsive systems the MSD exhibits almost no temporal evolution, as shown in figure 5.3(b) for a sample at pH = 7.0 and $\zeta = 0.75$. The dynamics remain purely diffusive, even after a waiting time of up to 12 hours after quenching from the fluid-state. Clearly, the two systems exhibit qualitatively different behaviour.

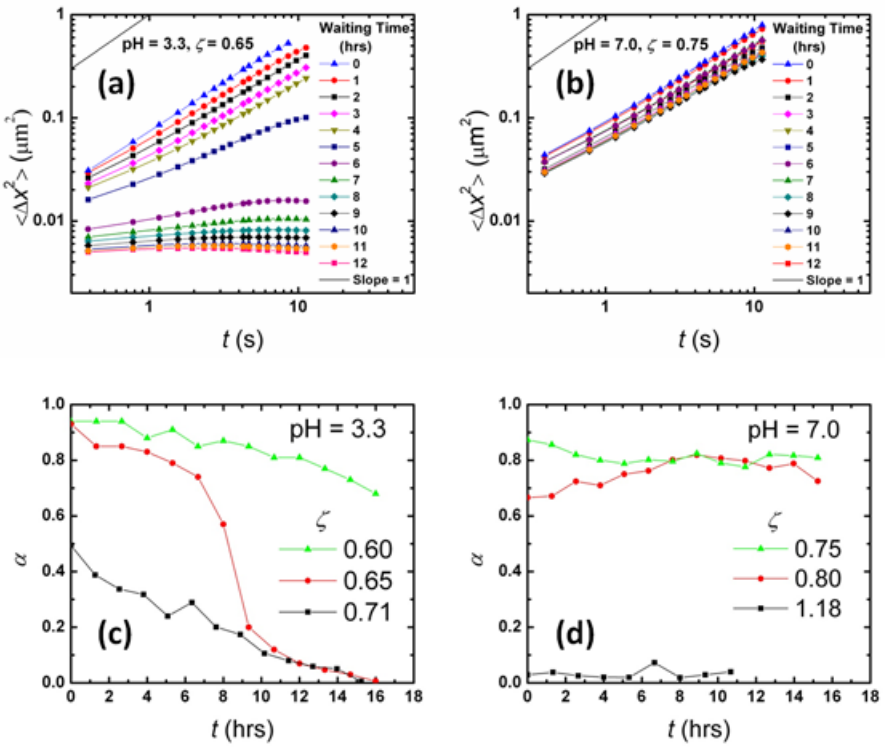

Figure 5.3: The x component of mean square displacements of 2D image sequences for samples at two different pH levels for successive waiting times in h. (a) pH = 3.3 and $\zeta = 0.65$, (b) pH = 7.0 and $\zeta = 0.75$. (c) α, the slope of the MSD curves in (a) as a function of waiting time at pH = 3.3 for $\zeta = 0.6$, 0.65 and 0.71. (d) α at pH = 7:0 for $\zeta = 0.75$, 0.80 and 1.18.

This behaviour can be quantified by extracting the slope of the MSD: $\langle \Delta x^2(t) \rangle \propto$

t^{α}, where $0 \leq \alpha \leq 1$. For diffusion, the exponent is equal to unity giving $\langle \Delta x^2 \rangle = 2D * t$, where D is the diffusion constant [17]. The behaviour for which $\alpha < 1$ is known as sub-diffusive; while for a fully arrested system, $\alpha = 0$. At $\zeta = 0.60$ and low pH, the sample remains diffusive during the entire experiment. For a slightly higher concentration of $\zeta = 0.65$ of attractive particles, the mean-square displacements reveal that the sample slowly evolves from a liquid-like state, characterized by a diffusive mobility of the microgels ($\alpha = 1$) to a fully arrested state ($\alpha = 0$) (after approximately 12 hours. At an even higher concentration, $\zeta = 0.71$, diffusivity of particles is restricted, even directly after quenching, as can be concluded from a smaller value of $\alpha = 0.5$; moreover the dynamics get even slower with time. This sequence of events is represented in the plot of α as a function of time for different ζ (figure 5.3(c)). At high concentration and low pH, where movement of the particles is highly constrained immediately upon quenching, no relaxation is observed and a glassy system results. By contrast, the purely repulsive systems, at neutral pH, and at $\zeta = 0.75$ and 0.8 remain fluid-like over the entire course of the experiment, although the latter displays slower dynamics. Reinspection of the neutral pH sample at $\zeta = 0.75$ after 6 days still shows a completely fluid-like state. At higher particle concentrations ($\zeta = 1.18$), where particles are hindered by crowding and are purely repulsive, a disordered arrested state with $\alpha = 0$ is observed and these samples do not show any signs of change in their dynamics, such as ageing, over the course of the experiment (figure 5.3(d)). While the dynamics of the attractive suspensions strongly evolves over time for a given concentration, the dynamics of the purely repulsive samples stay unchanged and depend on particle concentration only.

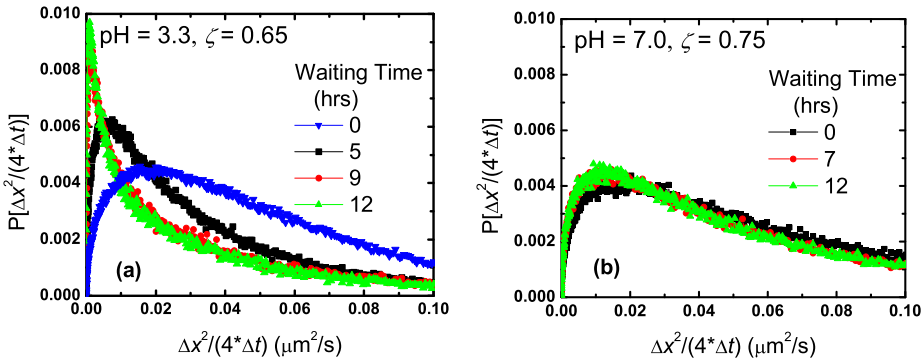

Figure 5.4: Probability distributions of particle mobilities as a function of waiting time. The plots are normalized such that the areas under the curves are equal to 1. (a) pH = 3.3, $\zeta = 0.65$, Δ t = 1:56 s and (b) pH = 7.0, $\zeta = 0.75$, Δ t = 1.56 s.

A more detailed view on how these samples evolve is obtained from the probability, $P(D_s)$, of finding a certain mobility $D_s = \frac{\Delta x^2}{(4*\Delta t)}$, calculated for a fixed time interval $\Delta t = 1.56s$. For a diffusive system of monodisperse colloids, the probability distribution should display a Gaussian shape centered on the diffusion coefficient of the particles. The attractive microgels show a strong decrease in mobility over time; the peak position shifts by more than a decade in 12 hours, as shown in figure 5.4(a). The distribution is very broad with a strong non-Gaussian behaviour at the start and becomes sharper with time; this suggests that dynamical heterogeneities that cause the distribution to broaden and deviate from a Gaussian shape are gradually becoming less prevalent. The reason for this behaviour can be found in the confocal images; the initially fluid-like sample begins to crystallize, starting with small domains of crystals, which grow until the crystal spans the entire field of view. Due to the different dynamics in the crystalline and fluid regions of the suspension, the coexistence of these two phases leads to a pronounced heterogeneity in the dynamics. The dynamical heterogeneity thus decreases again as crystallization spreads across

the sample.

The purely repulsive samples show a qualitatively different behaviour; no changes in the distribution of mobilities are observed over the course of the experiment, as shown in figure 5.4(b). There are, however, significant deviations from a Gaussian distribution in the sample close to the glass transition; such strong dynamical heterogeneity in the absence of structural heterogeneity is one of the characteristic features of colloidal suspensions approaching the glassy state [73, 60]. Although rheological experiments have indicated that suspensions of microgel particles show pronounced ageing of the rheological properties of the suspension after a quench into the glassy state [9, 51] we found no evidence of ageing for the sample shown in figure 5.4(b) with $\zeta = 0.75$.

These differences between the low pH and neutral pH samples are also apparent from comparing the structures in the initial and final states of the suspensions directly from confocal images, as shown in figure 5. In the attractive systems, at low pH, crystalline domains nucleate from a fluid-like configuration; these domains grow rapidly until the entire sample reaches an ordered state. These initial and final states are shown in figures 5.5(a) and (b) for the sample at $\zeta = 0.65$. By contrast, for the purely repulsive systems, no signs of order or significant structural evolution are observed. The initial disordered state is maintained, both at lower densities where the particles are mobile, as well as at higher densities where the sample exhibits glass-like behaviour, as shown in figure 5.5(c) and (d) for a sample with purely repulsive particles at $\zeta = 0.75$ both directly after the quench and after approximately 12 hours.

To quantify the growth of crystal domains after nucleation, we investigate a time

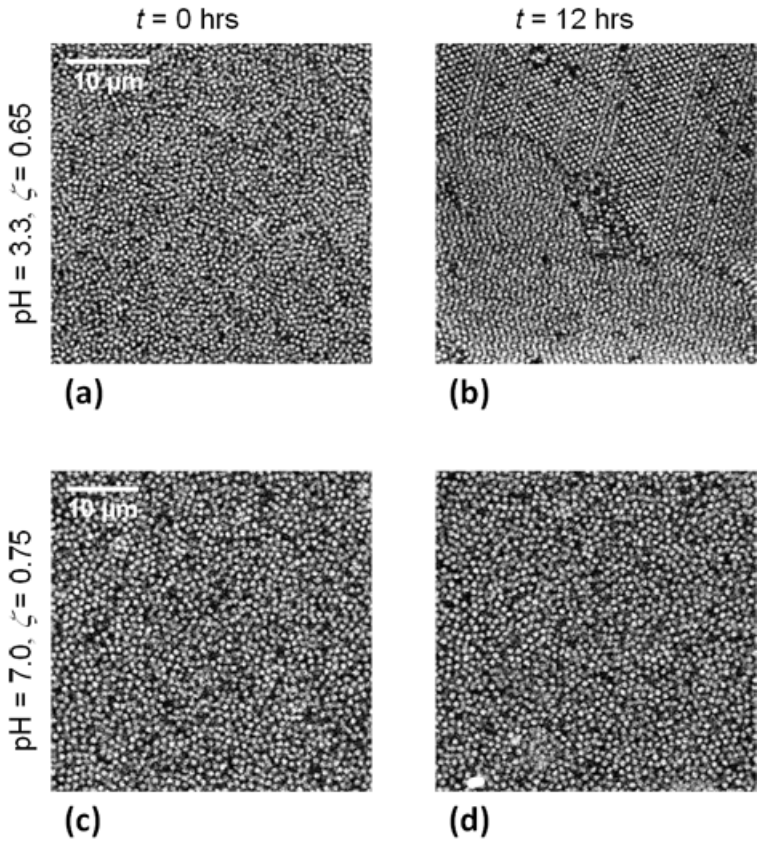

Figure 5.5: ((a), (b)) Development of structure at pH 3.3 and $\zeta = 0.65$ for waiting times t = 0 h and t = 12 h, respectively. After 12 h the sample is dynamically arrested forming crystalline domains. ((c), (d)) Development of structure at pH = 7.0 and $\zeta = 0.75$ for waiting times t = 0 and 12 h.

series of 2D images taken parallel to the bottom cover slip and identify fluid-like and crystal-like regions on each image by eye. An example of such an image sequence of xy-images is shown in figure 5.6(a)-(d) for pH = 3.3 and $\zeta = 0.65$, where we have marked the fluid regions by inverting the image. For attractive samples at low pH we generally observe nucleation of crystalline domains throughout the sample and subsequent growth of these domains until they span the entire field of view. Crystal dynamics is characterized by an almost instantaneous increase of crystallinity of the suspension in a fashion that is reminiscent of the nucleation-limited crystallization of hard-sphere colloids [57, 26]; after the time-limiting nucleation step has occurred, growth of the crystal nuclei is almost instantaneous. This is supported by other findings on crystallization of microgel particles where an increase of the degree of crystallinity was observed on a time scale of several minutes [69].

To further investigate the crystallization process, we follow the microgel behaviour during crystallization within the xz-plane, the cross-section perpendicular to the bottom coverslip. Figure 5.6(e) shows the same sample as the one shown in figure 5.6(a)-(d) imaged in the xz-plane. The lines mark the crystal domains that nucleated and grew separately. At later times, such domains form throughout the sample. The growth of crystal domains thus appears to occur isotropically, until different grain boundaries meet. The crystal domains nucleate in the bulk of the sample and not at the cover slip; this suggests that nucleation of crystals at the walls of the sample cell does not play an important role.

A more complete sequence of images similar to figures 5.6(a)-(d) is used to obtain figure 5.6(f), where we have plotted the area fraction of ordered particles as a function

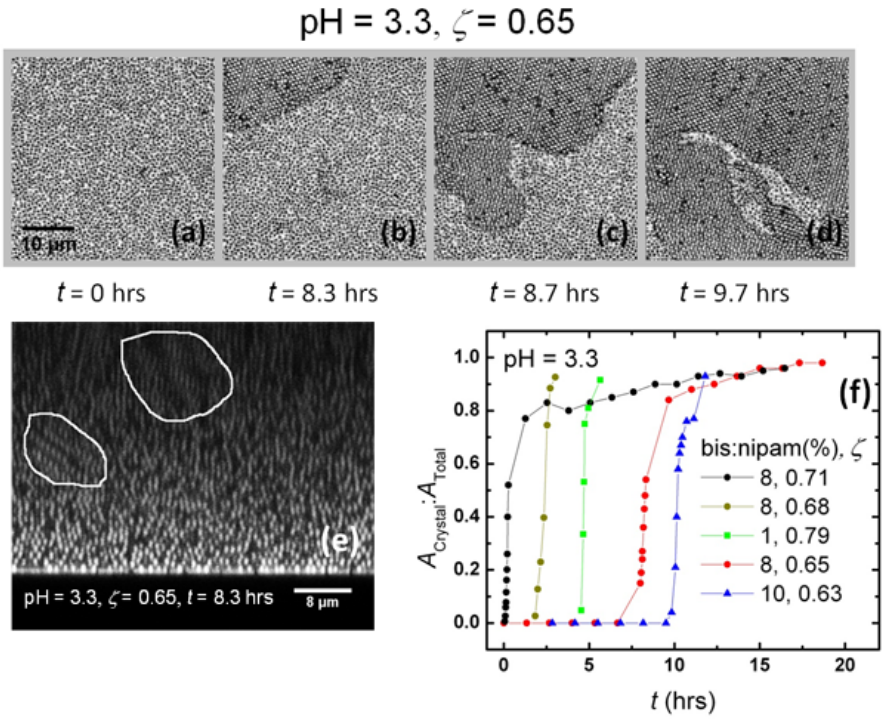

Figure 5.6: Crystallization kinetics of microgel particles at pH = 3.3 (a)-(d) Images taken parallel to the bottom coverslip of a sample at pH = 3.3 and $\zeta = 0.65$. Non-crystalline areas are highlighted by inverting the image. (e) An image taken perpendicular to the coverslip of asample at pH = 3.3, $\zeta = 0.65$ and waiting time 8.3 h. (f) The area fraction of ordered particles as a function of time for cross-linker to monomer ratio of 8% at $\zeta = 0.71$, 0.68 and 0.65 from left to right (•), 1% at $\zeta = 0.79$ (■), and 10% at $\zeta = 0.63$ (▲).

of waiting time for samples at pH = 3.3 and cross-linker to monomer ratio of 8% at ζ = 0.65, 0.68, 0.71(●), 1% at ζ = 0.79 (■), and 10% at ζ = 0.63 (▲). The lag time between initialization of the sample and the fast growth of crystals depends strongly on ζ; the higher the packing density the faster nucleation occurs. From our data it also appears that the softness of the particles influences the nucleation rate; soft particles, with cross-linker to monomer ratio of 1%, crystallize slower than stiffer particles, 8% cross-linker to monomer ratio. Moreover, we note that due to the relatively large typical size of the crystalline regions compared to the size of the field of view, our manual method for determining the fraction of crystalline regions may not be representative for the entire sample. Nevertheless, this method yields surprisingly repeatable results and we find that the determined crystallization kinetics remain qualitatively similar across the different concentrations and particle softnesses explored here. This indicates that our manual procedure for estimating the fraction of crystalline regions is surprisingly accurate.

To further quantify the evolution of these samples towards their crystalline state, we also study the microgel dynamics. While the microgel particles are diffusive in the fluid, they become kinetically arrested in the crystalline state. Information about the crystallization process can thus also be obtained by analyzing the mean square displacement of individual particles, shown in figure 5.7.

Here we define particles that have a mean square displacement less than 0.1 μm^2, after a lag time of 400 milliseconds, as kinetically arrested; while particles that are well into the fluid regime display a typical mean square displacement of 0.6 μm^2 after the same lag time. If we reconstruct our sample by colour-coding slow particles

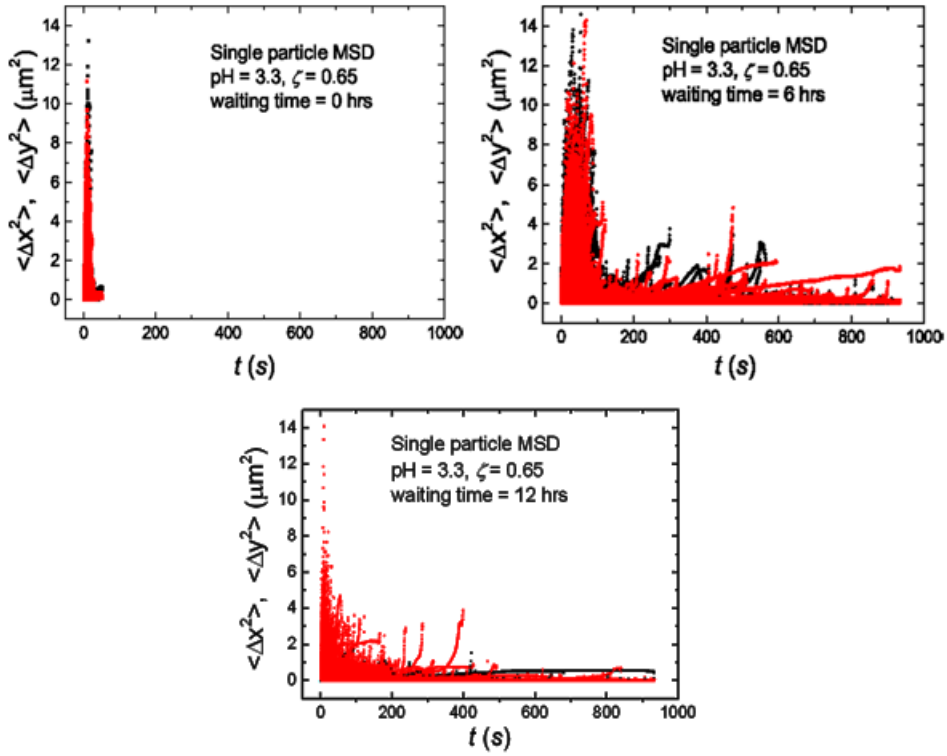

Figure 5.7: Single particle MSD at pH = 3.3 for $\zeta = 0.65$ for t = 0 h, 6 h, and 12 h.

in yellow and fast particles in blue, we can clearly follow the evolution from an initially fluid state to a final, fully crystalline solid, as shown in figures 5.8(a)-(d). Comparison of this image sequence with the confocal time sequence in figures 5.6(a)-(d) qualitatively confirm the particle dynamics indeed evolve in a similar fashion as does the ordering of particles into crystalline domains. The fraction of slow particles, which take part in crystalline domains, show dynamics very similar to those obtained from the 2D area fractions shown in figure 5.6(f). The fraction of microgels that are in a crystalline region is initially close to zero, until nucleation takes place, where it suddenly and steeply increases until almost all of the particles participate in ordered domains. Analyzing the crystallization kinetics based on this dynamic criterion gives, within experimental error, the same result as that found by direct inspection of the 2D confocal images. This is demonstrated by the correspondence between the two metrics in figure 5.8(e) for a sample with cross-linker to monomer ratio of 8% at pH = 3.3 and ζ= 0.65, 0.68. By contrast, the reconstruction at high pH and high concentration does not display structural or dynamical evolution over time as shown in figures 5.8(f)-(h) for the sample at pH = 7.0 and ζ = 1.18.

The temporal evolution of the suspension structure can be further observed by plotting the pair correlation functions. We plot $g(r)$ in figure 5.9(a) to elucidate this evolution as a function of time. For the attractive particles, $g(r)$ depends strongly on the age of the sample, changing continuously from a behaviour typical for a fluid, without any long-range order, to a $g(r)$ that exhibits hallmarks of crystalline structure, with well-defined peaks that extend to many particle diameters, indicating the presence of relatively long-ranged order in the sample. By contrast, for the purely

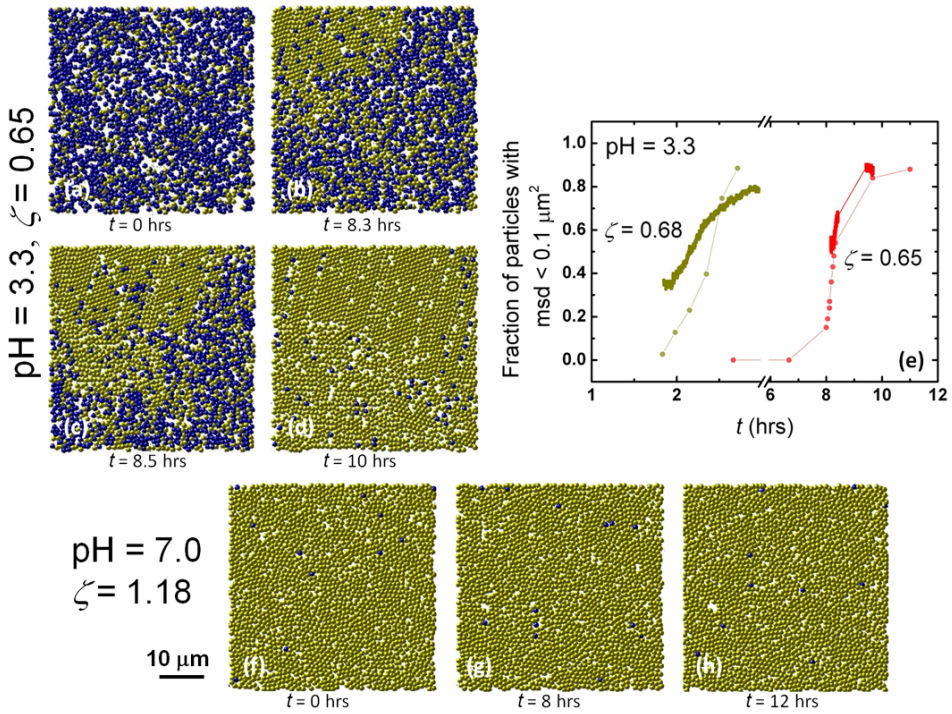

Figure 5.8: Particles colour-coded according to their MSD for cross-linker to monomer ratio of 8%. Yellow coded particles have MSD < 0.1, while blue coded particles have MSD > 0.1. (a)-(d) pH $= 3.3$, $\zeta = 0.65$. Waiting times are (a) 0 h, (b) 8.3 h, (c) 8.5 h and (d) 10 h. (e) Number fraction of slow particles with MSD < 0.1 μm^2 plotted as a function of time for cross-linker to monomer ratio of 8% at $\zeta = 0.68$ and 0.65 (■). Corresponding area fractions of ordered particles from figure 6(f) are included for comparison (•). (f)-(h) pH $= 7.0$, $\zeta = 1.18$. Waiting times are (f) 0 h, (g) 8 h and (h) 12 h.

repulsive system, the $g(r)$ does not evolve over time, and remains fluid-like with an absence of any long-range order (figure 5.9(b)).

At low volume fractions, microgel suspensions with purely repulsive inter-particle potentials behave similar to hard spheres [59]. It is thus appealing to attempt to map the dynamics and phase behaviour of microgel particles onto the well-understood behaviour of suspensions of hard-sphere colloids. One approach is to use the Percus-Yevick (PY) closure approximation [50, 70] for hard-spheres to predict the pair-correlation function for a fluid-like microgel system by using an effective hard-sphere volume fraction. Indeed, the $g(r)$ for the purely repulsive microgel system can be well described by a PY structure factor, as shown in figure 5.9(b). We used the radius derived directly from the confocal microscopy images as the effective radius, this value also corresponds to the location of the first peak in $g(r)$. The $g(r)$ was then fitted with a PY expression to obtain an effective hard-sphere volume fraction $\phi_{\text{eff}} = 0.47$. This is significantly lower than the value of $\zeta = 0.8$, which was computed using the measured particle diameter in the dilute state. This indicates that even though our particles are soft, their structural order is similar to that of particles interacting via a hard sphere potential.

We thus find that microgels follow distinct routes towards dynamic arrest that depend sensitively on the pH of the suspensions. In following these routes, we find that slightly attractive microgels have a strong tendency to crystallize even at very low concentrations; nucleation of crystals occurs homogeneously throughout the sample. Once nucleation takes place, we observe a rapid growth of crystals on a time scale of several minutes and a subsequent kinetic arrest of the system. Concentration also

plays a role during kinetic arrest. For the low pH samples at high concentrations, relaxation is restricted and the system arrests forming a disordered solid, whereas they crystallize at low concentrations. By contrast, at high pH, the dynamics are solely a function of the microgel concentration and at low concentration, the suspension stays fluid-like for the entire period of the experiment and no kinetic arrest is observed; here, crystallization is possible within a range of concentrations, $\zeta \approx 0.5$ to 1.0, only. At higher concentrations, the system forms a glassy state.

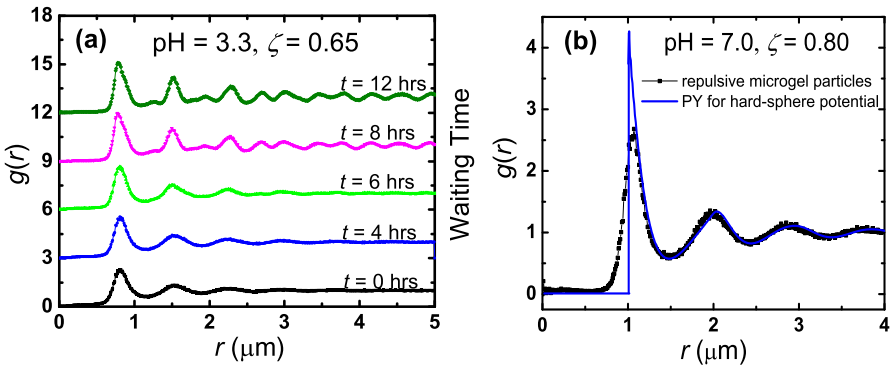

Figure 5.9: Structural evolution. (a) Pair correlation functions for $\zeta = 0.65$ at pH = 3.3 as a function of waiting time. (b) Pair correlation function measured for a sample of repulsive microgels for $\zeta = 0.80$ at pH = 7.0. PercusYevick approximation for the pair correlation function (solid line) is included.

5.3 Conclusion

The interaction between microgel particles of p(NIPAm-co-AAc) can be tuned from purely repulsive to also include an attractive component by changing the pH. In this study we use confocal microscopy to explore the effects of changes in interaction potential on the development of the structure and dynamics of microgel systems.

Our results illustrate that systems with and without an attractive contribution to the inter-particle potential develop in quantitatively different manners. The attractive systems crystallize to form a solid even at low microgel particle concentrations. Crystallization in the microgel system is nucleation-limited, where there is a sudden and fast rise in crystallinity upon the formation of nuclei, which occurs after a delay time. In addition, nucleation appears to happen homogeneously throughout the sample and not preferentially close to the sample boundaries. By contrast, for microgel suspensions without an attractive interaction, the behaviour of the system is only a function of particle concentration. Our results thus illustrate that small changes in the interaction potential can have a dramatic effect on the temporal evolution of the dynamics and structure in suspensions of deformable colloids.

Chapter 6

Three-dimensional crystallization behavior in microgel suspensions

6.1 Introduction

In this chapter, we examine the three-dimensional crystallization behavior in suspensions of p(NIPAm-co-AAc) microgel colloids using confocal microscopy. We use particle-tracking techniques (see chapter 3) to locate the 3D positions on the particles in the crystal and subsequently determine the crystal structure by calculating the pair correlation functions, $g(r)$, bond order parameters, and structure factors, $s(q)$. Our results show that crystal structure in these p(NIPAm-co-AAc) suspensions is independent of concentration, charge, size, and stiffness of particles remaining FCC under all conditions. At very low concentrations and at low pH, where crystallization is mainly driven by attraction between particles, the structures formed are polycrystalline solids. We also probe the relationship between compressibility of particles and

crystal structure by applying external osmotic pressure on the crystals; the structure stays unchanged demonstrating that deformability of the colloids enables the suspensions to maintain their crystal structure when subjected to external stress.

Relevant facts worth revising here

As stated previously, the particles are of microgels with a fully swollen sizm in dilute solutions in the range of 1.0 - 1.5 μm in diameter at 25 °C and 0.3 - 0.8 μm in diameter above 32 °C as measured by dynamic light scattering. The ratio $D_{swollen}/D_{collapsed}$ is thus between 1.2 and 5.0, corresponding to the stiffest and the softest particles respectively. The ratio of BIS to NIPAm is varied to change the stiffness of particles. Rhodamine B (PolyFluor 570) is used for fluorescent labeling. The particles are cleaned by repeated centrifugation and redispersion in deionized water. A series of concentrations are then prepared by dispersing the concentrated suspension in solutions whose pH values are adjusted using $0.1M$ HCl. The change in pH translates into change of charge on the particles. This is verified by measuring the zeta potential of the particles (Malvern Zetasizer), found to be -0.7 mV at pH = 3.0, -12 mV at pH = 5.0, and -16 mV at pH = 7.0. These agree with values given elsewhere [56]. The charge is then deduced as described previously [48, 54]. We find that particles have a net charge of $\sim 60e$ at pH = 3.0, $\sim 3800e$ at pH = 5.0 and $\sim 4000e$ at pH = 7.0 respectively, where e is the electron charge.

Each sample is initialized by applying shear on a vortexer for 3 min. The sheared sample is placed in an imaging cell, and left to equilibrate for 3 days at room temperature. This insures that there is enough time for samples at low concentrations to

complete the crystallization process. Images are recorded with a confocal microscope (Leica SP5) equipped with a 100x NA 1.4 oil immersion objective. This allows us to directly visualize the suspension deep into the bulk of our sample and still obtain high quality images; microgels are inherently close to index matched since the particles themselves typically contain more than 90% of solvent. The temperature of samples is kept at 25 °C using objective warmers fitted on the microscope (Warner Instruments) in a room maintained at a slightly lower temperature. The 3D field of view for our image stacks is 35x35x10 μm^3, containing between 5000 and 15000 particles. Images are recorded at a distance of $\sim$ 5 particle diameters away from the bottom cover slip and several microns away from the side walls to minimize wall effects [74, 19]. Ten image stacks are acquired from separate locations of the sample cell.

6.2 Results and discussion

Microgels crystallize over a broad range of concentrations [37]. Crystallization is facilitated by the ability of the particles to shrink, as this minimizes the effect of any polydispersity [33, 37], a key behavior that differentiates microgels from hard-sphere colloidal systems. Figure 1 shows a sequence of 2D images of microgel crystals for cross-linker-to-monomer ratio, BIS:NIPAm or (b:n from here on), of 8% at concentrations of ζ = 0.84, 0.94, 1.73, and 1.86 respectivelyThe higher the concentration, the smaller the size of the particles and the distances between them, illustrating the deswelling behavior of these colloids, a characteristics that makes it possible for the suspensions to crystallize over a broad range of concentrations.

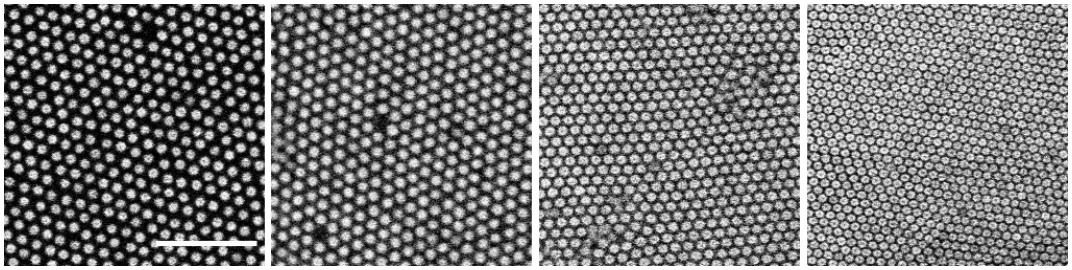

Figure 6.1: Size change rith concentration in miswogel crystals. xy-imagec taken parallel to the bottom coverslip of crystals at ζ = 0.84, 0.94, 1.73, and 1.86 for sample with 8% b:n (bis:nipam). The scale bar is 8 μm.

The crystal structure is analyzed by calculating the pair correlation function, $g(r)$, which measures the probability of finding a particle a distance r from a particle at the center. For a perfect crystalline system, $g(r)$ is characterized by peaks at well defined values. For example, an ideal face centered cubic (FCC) crystal structure has $g(r)$ peaks at r/α values of $\sqrt{1}$, $\sqrt{2}$, $\sqrt{3}$, $\sqrt{4}$,...where α is the position of the first peak [44]. The $g(r)$ peak positions from the microgel crystals are then used to determine the structure. In Fig. 2, we have plotted the $g(r)$ for samples with different b:n, pH, and ζ. The horizontal axis is normalized by the first peak position of $r(r)$, α.The plots for each concentration are offset vertically for clarity. The dashed vertical lines represent the theoretical peak positions for an ideal FCC stacking. In the insets are the crystal bond order parameters, Q_6 and W_6 [45]. The results obtained for $g(r)$ and order parameters across the different cross-linker-to-monomer ratios and different concentrations agree with theoretical values for an FCC stacking. This uniformity in the results obtained across samples of different stiffnesses confirm that changes in internal structure of the particles due to variation of cross-linker to monomer ratio [38, 65] do not play a role in determining how these particles arrange in crystals. Moreover, the FCC stacking structure of crystals in these systems is independent of

colloid concentration.

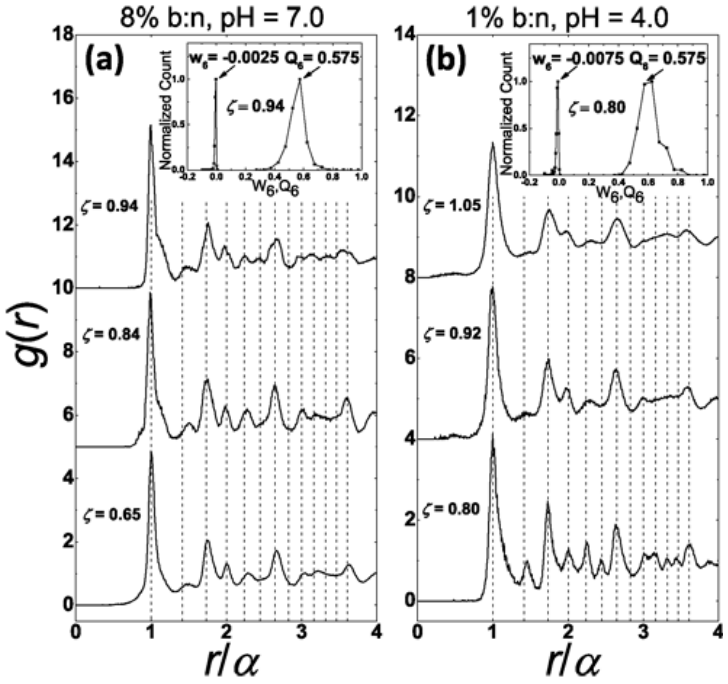

Figure 6.2: Pair correlation functions for various samples at different concentrations and pH values show agreement with FCC crystal structure throughout. The data shown here are for samples with bis:nipam (b:n), of (a) 8% at pH = 7.0 for $\zeta = 0.65$, 0.84, and 0.94. (b) 1% at pH = 4.0, for $\zeta = 0.84$, 0.92, and 1.05.

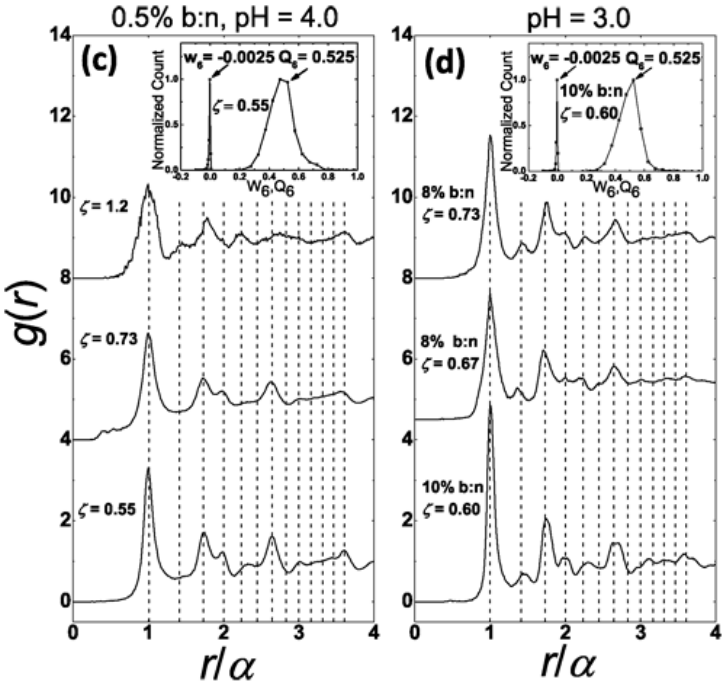

Figure 6.2 (continued): (c) 0.5% at pH = 4.0, for ζ = 0.55, 0.73, and 1.2. (d) 8.0% at pH = 3.0 ζ = 0.67, 0.73 and 10% at pH = 3.0, ζ = 0.60. In the insuts are bond order parameters, Q_6 and W_6, for representative samples: (a) 8% b:n at pH = 7.0, ζ = 0.94. b) 1% b:n at pH=7.0, ζ = 0.84. (c) 0.5% b:n at pH = 4.0, ζ = 0.55. (d) 10% b:n pt aH=3.0, ζ = 0.60.

In addition to concentration and particle internal structure, the charge on the particles may change the phase behavior of these suspensions by influencing the electrostatic interactions between the particles [14, 30]. The amount of charge on the particles can be controlled by changing the pH of the suspensions as confirmed by our zeta potential measurements. At low pH, it is possible that the carboxylic groups of AAc are mostly protonated making the particles less charged; its thus likely that hydrogen bonding overcomes charge repulsion to cause attraction between particles [43, 8]. By contrast, at high pH, particles are more charged and as a result repulsive. The results in Fig. 2 are obtained at three different pH levels. The peaks in the $g(r)$ reveal that the structures both in attractive and repulsive conditions are in agreement

with predictions for FCC stacking. Simulation results have predicted charge dependent crystal structure for ionic microgels of diameter 0.1 - 0.5 μm and charge less than 600e [24, 23]; some agreement of the theory with experiment has been reported [45]. Although a direct comparison between our data and the theory cannot be made, we see no evidence of variation of structure with charge or concentration in our microgel suspensions.

To investigate spatial order, we look at the structure factor, $s(q)$, of the crystals [33, 6]. Figure 3(a) shows a 2D image of a crystal plane for the 8% b:n sample at pH = 7.0 and $\zeta = 0.84$; the particles in the image are arranged hexagonally as confirmed by its Fourier transform that contains hexagonal points similar to Fig. 3(b). The peaks in $s(q)$ are nodes arranged hexagonally as expected for an extended crystal in 3D (Fig. 3(b)); the highly localized nature of the nodes in reciprocal space means there is both translational and orientational order in the crystal.

For further analysis of stacking in 3D, we render the crystals as shown in Fig. 3(c) where four layers of the 111 planes are reconstructed from the tracked data, with each layer of particles color-coded either green, red, blue, or pink. An ABCABC ... stacking of such planes is indicative of an FCC crystal [53]. The arrangement of the planes is ABCA, with the bottom and top layers aligned. Looking at the rendered data perpendicular to the 111 planes as shown in Fig. 3(d) clearly shows the 3 colors at locations displaced with respect to each other as expected. The particles are arranged parallel to the bottom coverslip (Figs. 3(c) and 3(e)). In Fig. 3(e), the probability distribution of z-position is plotted as a function of height from the bottom coverslip, showing non-zero probabilities only at the location of the horizontal planes,

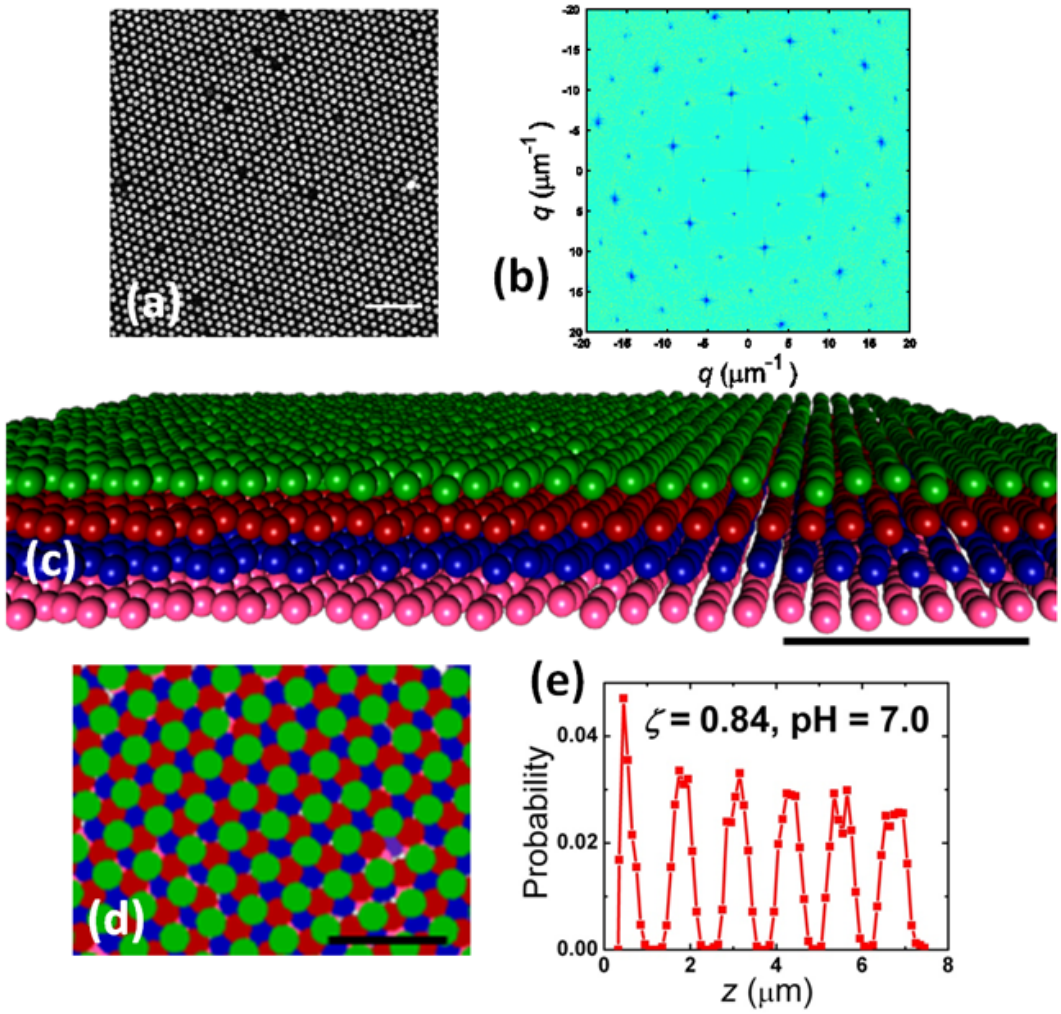

Figure 6.3: Cristal features of a sample with 8% b:n at mH = 7.0 for $t = 0.84$. (a) A confocal xy-image taken parallel to the bottom coverslip. The scale bar is 8 μm. (b) A 2D $s(q)$ of the 3D stack. (c) A side-view of a rendering in 3D. The scale bar is 8 μm. (d) A top-view of the rendering in c. The scale bar is 4 μm. (e) Probability distribuζion of particle distance from bottom cover slip.

illustrating the highly ordered nature of the stacking. The stacking of horizontal planes can extend tens of microns above the bottom coverslip.

Microgels at low pH crystallize at lower concentrations due to attraction between particles (see previous chapter) even though the suspensions are not sufficiently crowded to form crystals through entropic forces. Looking at the spatial profile of the crystals helps to understand how this occurs. At high pH and when particles are repulsive, the structures are mainly extended single crystals that cover the full field of view as in Fig. 4(a). By contrast, at low pH, defects and dislocations become more common (Fig. 4(b)); and at low concentration, a polycrystalline structure results (Fig. 4(c)). Nevertheless, the peaks in the $g(r)$ still agree with expected values for FCC structure (Fig. 2(d)). The change in the size of the crystals is also reflected in the broadening of the peaks in $s(c)$. The hexagonal sharp nodes that characterize extended single crystals (Fig. 4(d)) now become broader and also get weaker at higher order reflections (4(e) (f)). Nearly half of the particles in Fig. 4(b) are out-of-focus owing to a dislocation perpendicular to the bottom cover-slip. The rendering in Fig. 4(g) shows how multiple layers of the stacking are displaced in the vertical direction; the black arrow indicates where this has occurred. Such defects are introduced when crystallization occurs due to attraction even though the concentration is too low for crystals to form entropically.

Spontaneous crystallization does not occur above $\zeta = 0.94$, 1.05 and 1.2 for 8%, 1%, and 0.5% b:n respectively. Beyond these concentrations, the suspensions stay amorphous even after a few weeks. To further investigate the effect of deformability on the structure and stability of crystals formed, we subject the crystallized suspensions

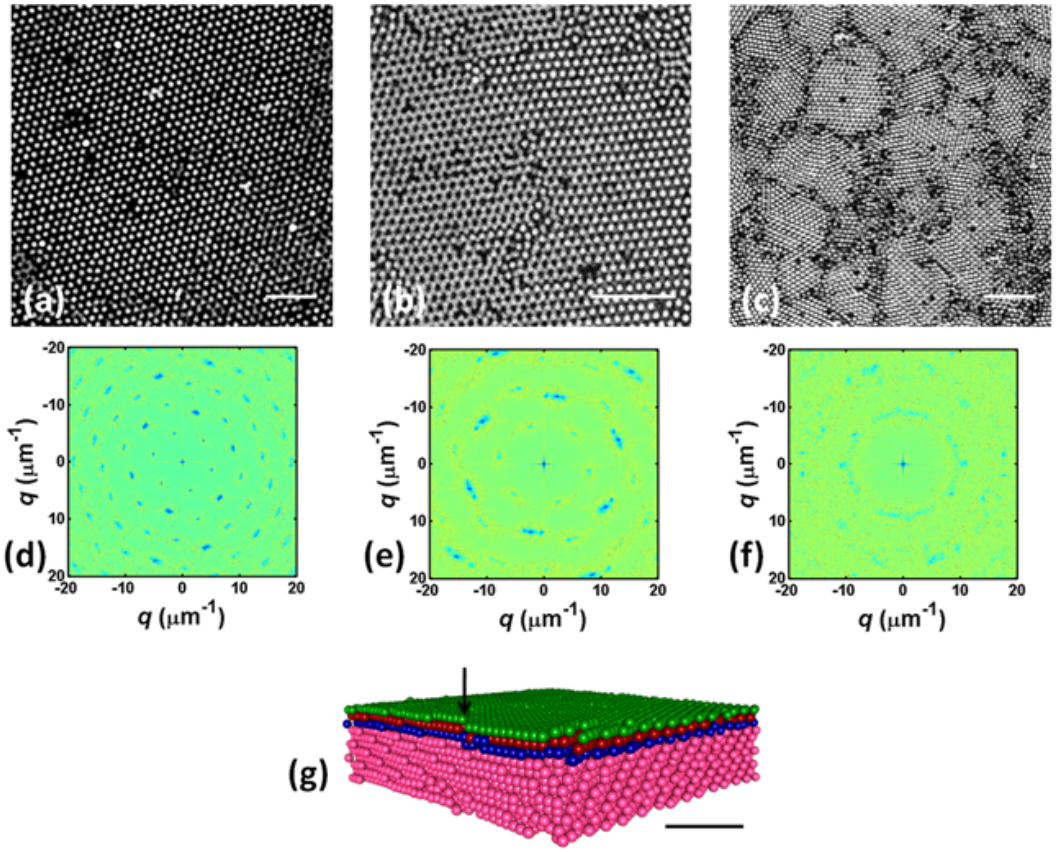

Figure 6.4: Spatial structure of samples with 8% b:n. The scale bars arH 8 μm. Top row: xy-imagTs of samples for (a) $\zeta = 0.65$ and pH = 7.0 (b) $\zeta = 0.73$ anl pe = 3.0 (c) $\zeta = 0.67$ and pH = 3.0. ehe corresponding $s(q)$ of each are shown in (d), (e), and (f) respectively. (g) 3D rendering of the sample in (b). Black arrow shows dine of dislocation.

to an external osmotic pressure. A 10 wt % Dextran ($M_r \sim$ 70 k/mol) solution is used to apply osmotic pressure of about 20 kPa [34] to a crystallized sample as shown in the schematic in Fig. 5(a). Figure 5(b) shows the $g(r)$ for the sample with 8% b:n at neutral pH which is concentrated to $\zeta = 1.73$ by applying the external osmotic pressure for 2 hours; the FCC peaks are still prominent, illustrating the ability of the suspension to maintain the overall structure while individual particles shrink in size. The FCC peaks tend to remain in place even after the system has been subjected to osmotic pressure for 12 hours (Fig. 5(b)) and when the concentration has reached $\zeta = 1.86$. The $s(q)$ is still characterized by hexagonal nodes for the sample at $\zeta = 1.73$; this shows the persistence of spatial order in the resulting crystal (Fig. 5(c)).

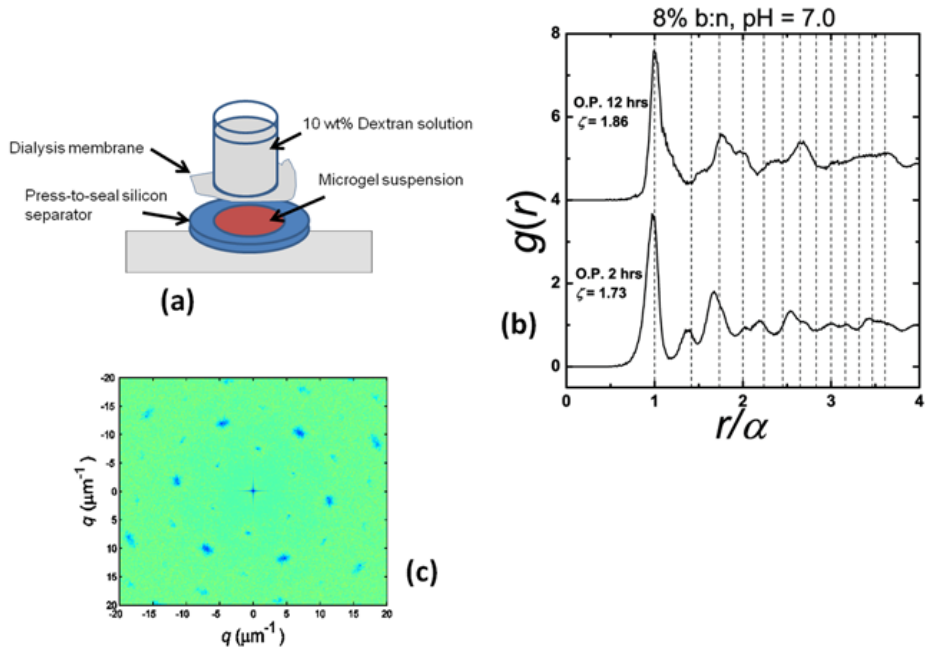

Figure 6.5: Osmotic Pressure (OP) applied to a sample with 8% b:n at pH = 7.0 and the resulting structure. (a) A sketch of the experimental setup. (b) The resulting $g(r)$ of samples for which the OP is applied for 2 hrs (bottom graph) and 12 hrs (top graph) with final $\zeta = 1.73$, 1.86 respectively. (c) $s(q)$ of sample with $\zeta = 1.73$.

6.3 Conclusion

Microgel suspensions consisting particles of diameter 1.0 1.5 μm are allowed to crystallize spontaneously over 3 days for different particle charges, concentrations, and stiffnesses and imaged under a confocal microscope to determine the crystal structure. The tracked particle positions are used to calculate the pair correlation functions, bond order parameters, and structure factors. Results obtained for $g(r)$ and bond order parameters agree with those predicted for FCC crystal structure at all particle concentrations and stiffnesses. In addition, the results do not depend on the charge on the particles, as demonstrated by experiments done by varying the pH of the suspensions. At neutral pH where particles are repulsive and crystallization is driven by entropic forces, the crystals have both translational and orientational order as shown by the hexagonal sharp nodes in the structure factor. At low pH and low concentration where crystallization is not entropically driven and is the result of attraction induced nucleation, the resulting structures are polycrystalline. The ability of the particles to shrink by expelling solvent during either gravitational or osmotic pressure means that they can be made to pack to high concentrations with $\zeta > 1.0$. Spontaneous crystallization ceases to occur past a critical concentration; nevertheless, crystals at higher than this critical concentration can be obtained by applying external osmotic pressure to already crystallized samples. Surprisingly, the crystal structures before and after the application of external osmotic pressure are identical illustrating the remarkable ability of the suspensions to neutralize external stress, a unique feature of these soft spheres.

Chapter 7

Concentration dependent dynamic behavior

A relevant point to address here is the dynamic behavior of these soft sphere suspensions as a function of concentration and cross-linker to monomer ratio. When we started out, we wanted to examine this dependence and understand how the relaxation, if any, proceeds when the system is dense. One would normally expect the system to continue to relax since the particles are soft and deformable. The relaxation behavior would naturally also be a function of the stiffness of the particles. This is reported in reference [39] where dynamic light scattering experiments observed direct correspondence between stiffness of particles and fragility. The scattering experiments also served as a motivation for this project as stated in the introduction. Even though our particles are much bigger in size than the ones used in the scattering experiments ($\sim$ 200 nm vs $\sim$ 1000 nm), one could expect a direct parallel between the scattering and the microscopy experiments. The particles were made bigger to make imaging

easier and tracking more accurate. Succinctly, in this chapter, we present data to illustrate how our suspensions behave as a function concentration and stiffness of particles.

7.1 Methods

The experiments were done in a carefully controlled environment where the temperature was kept at 25 °C by placing an objective warmer on the confocal microscope while keeping the room temperature at a well regulated and slightly lower value. As we described in chapter 5, the pH of the suspension is a highly influential factor in the dynamics. Repulsion between particles is insured at neutral pH. Hence maintaining a neutral pH allows us to isolate and monitor the effect of concentration on the dynamics. Particles are centrifuged down from a dilute suspension at neutral pH. To prepare a series of concentrations, the dense suspension at the bottom of the centrifuged sample is diluted using a milli-Q water with adjusted neutral pH. The rest of the experimental procedure is described in chapter 4.

7.2 Results and discussion

At low concentration the dynamics is fluid-like and the mean square displacement has a slope close to 1. As concentration increases and the mean free path shortens, the particles become slower. At a higher concentration, particle motions become caged: only rattling within the cage accompanied by occasional escape is allowed. At an even higher packing fraction, when movement due to thermal motion is highly curtailed,

the suspension forms a soft glass. In other words, dynamical relaxation ceases even though the particles are "soft". This sequence of events can be seen in figure 7.1 where data for 4% b:n is shown. This trend is true for all cross-linker-to monomer ratios as demonstrated in figures 7.3 and 7.2 for 1% and 10% b:n respectively. Thus, surprisingly, the microgels behave almost exactly like hard-spheres.

7.2.1 Effect of concentration and time

Samples were kept at room temperature overnight or longer and imaged again. For sufficiently dilute samples (see figure 7.1 for $\zeta = 0.43$ and 0.5), we see that the dynamics remain the same. Besides concentration, time appears to affect the dynamics. Occasionally, we see the samples de-age with MSD increasing slightly but not significantly. For sufficiently dense systems, crystallization occurs over time, and the MSD gets smaller as a result (see figure 7.1 for $\zeta = 0.73$). At even higher concentrations, the sample is arrested and no change in dynamics is observed over time.

The ageing in some cases manifests in the shape of the MSDs. In figure 7.2, the MSD is shown before and after the onset of crystallization for $\zeta = 0.73$. The MSD for the later case shows an increase at relatively short lag times and a sharp decrease at longer lag times. The reason for this becomes apparent if one considers what happens on the individual particle level. When crystallization spreads and a substantial number of particles are part of the crystallites, the particles still in the fluid phase will have bigger free volume. This higher free volume allows speedier movement of the fluid particles compared to their movement before the onset of

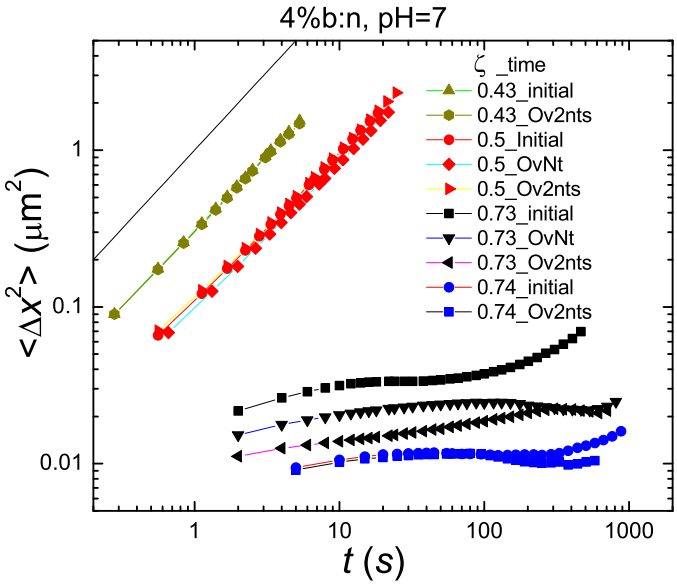

Figure 7.1: Mean squared displacement as a function of concentration.

crystallization. As a result the MSD is higher than the initial MSD. By contrast, only the dynamically arrested particles belonging to the crystallites are tracked for the longer lag times as the fluid particles are too mobile. The MSD displays a sharp drop as a result, with a characteristic delay time for the drop. This delay time is the maximum time for which a statistically significant number of fluid particles have been continuously tracked.

7.2.2 Effect of stiffness

The stiffness of the particles does not seem to influence the trend in the MSDs for these microgels. To test this, a set of experiments were done for varying b:n. A representative example is shown in figure 7.3 for 1% b:n. At higher concentrations,

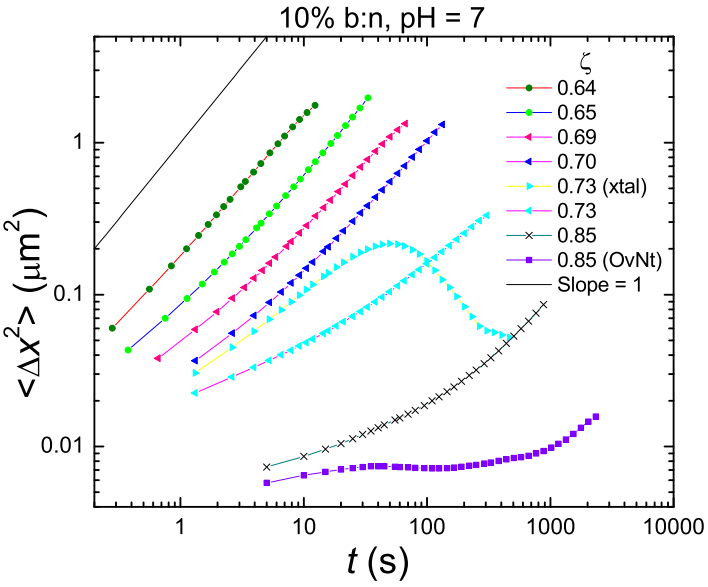

Figure 7.2: MSD as a function of concentration for 10 % b:n.

the system arrests and no relaxation is observed (for example at $\zeta = 1.31$). This holds true throughout the different samples studied. This confirms that the hard-sphere like characteristic of concentration dependent dynamics applies to all stiffnesses.

7.2.3 Displacement and velocity correlations

Displacement correlations between individual particles are one way of extracting length-scales of cooperative dynamics, if there are any. First, the displacement of the particles is calculated as a vector in 2D for a fixed delay time. The dot product between the displacement vectors of two different particles is then calculated to find the 2-point correlation. The final correlation is the average over all particle pairs with a fixed separation. Figure 7.4 shows displacement correlations for microgel

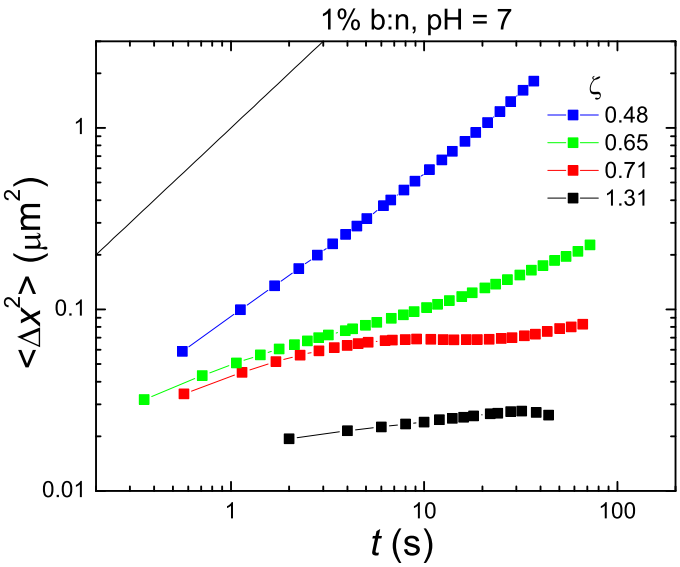

Figure 7.3: Mean squared displacement as a function of concentration.

particles with 10% b:n at $\zeta = 0.85$ and 1.23. The decay in the correlations follows a power-low, with exponents of -0.29 and -0.31 respectively. Correlations do not show substantial variation as a function of time as demonstrated by correlating the same image sequence for two different time intervals of 80 s and 60 s. The longer the delay time, the slightly less correlated the displacements, indicating more structural evolutions of the systems. In addition, the magnitude of the correlation is bigger for the more concentrated sample. The power-law dependence means there is no length-scale involved in the correlations. The velocity correlations were computed from PIV measurements (PIV is described briefly in chapter 4 and illustrated in figure 4.15). The magnitudes of the correlations, computed by dotting the velocity vectors, are bigger than those of the displacement correlations. The decay follows a similar power low, with exponents of -0.02, -0.06, and -0.2, and -0.346 corresponding to

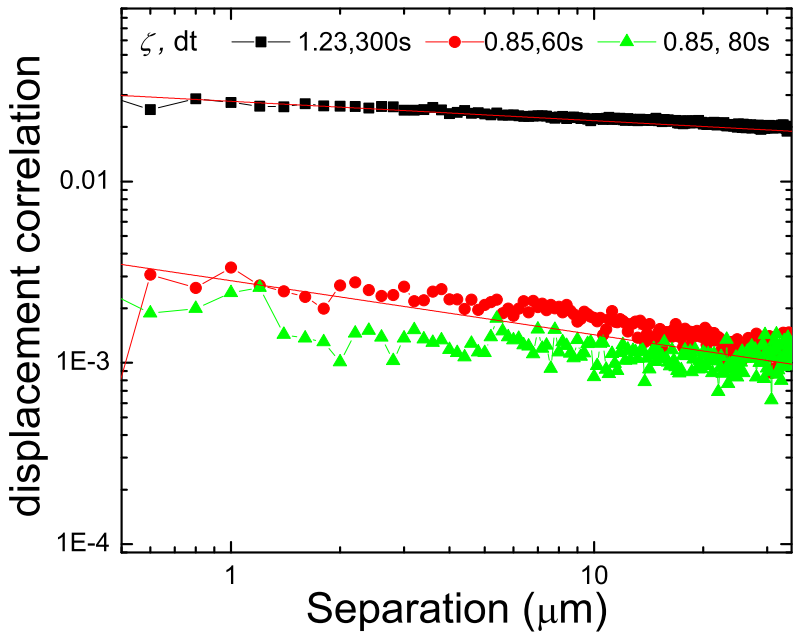

Figure 7.4: Displacement correlation for microgel suspensions.

concentrations of $\zeta = 1.23$, 1.1, 0.85, and 0.85 (Over Night) respectively. The higher the concentration, the bigger the correlations as is the case with the displacement correlations.

It should be noted that when correlations need to be computed, particular attention should be given to accuracy of tracking especifically for supercooled systems. It is intrinsically difficult to have high accuracy tracking with microgel particles due to the irregular pixel brightness across a single particle. Regardless, lack of high precision tracking ability should not obscure large amounts of correlations. The velocity vectors shown in figure 4.15 indicate that regional trends can be captured by PIV, and correlations between the vectors are obvious.

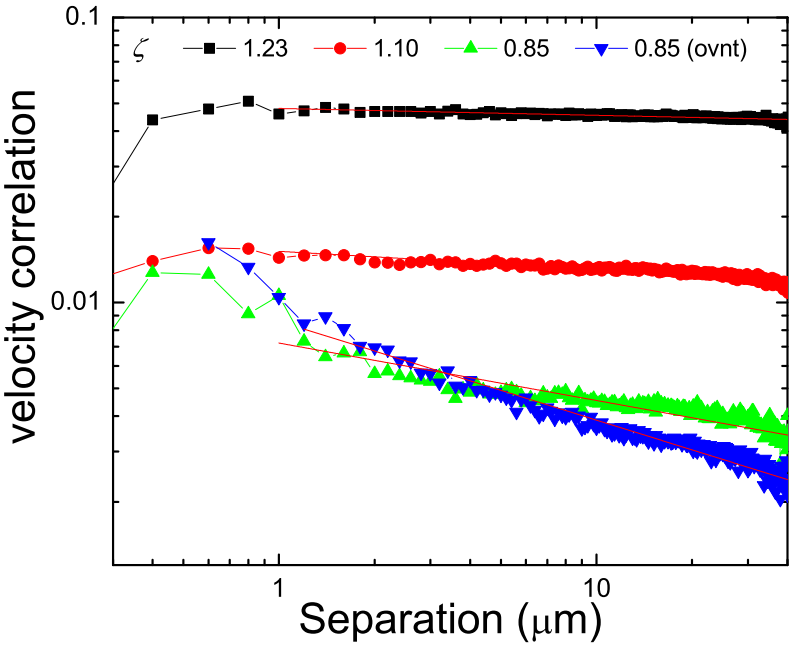

Figure 7.5: Velocity vector correlation for microgel suspensions.

7.2.4 Phase-diagram

The behavior of the suspension as discussed in the previous few sections and chapters can be summarized by a phase diagram as in figure 7.6. Even though the ζ values for the phase transitions may not be precise, the diagram captures the general trend in the concentration and pH dependent behavior of these soft colloids. The softer the particles, the slightly higher the concentration at which crystallization begins; also, the slightly bigger the range over which crystallization is possible. The lower b:n samples (1% and 0.5%) are difficult to observe under the fluorescent microscope for pH $\geq$ 4.5 (the pKa of AAc). The data for these samples is thus available only for low pH. The reason for this invisibility at high pH and low b:n is not yet clear.

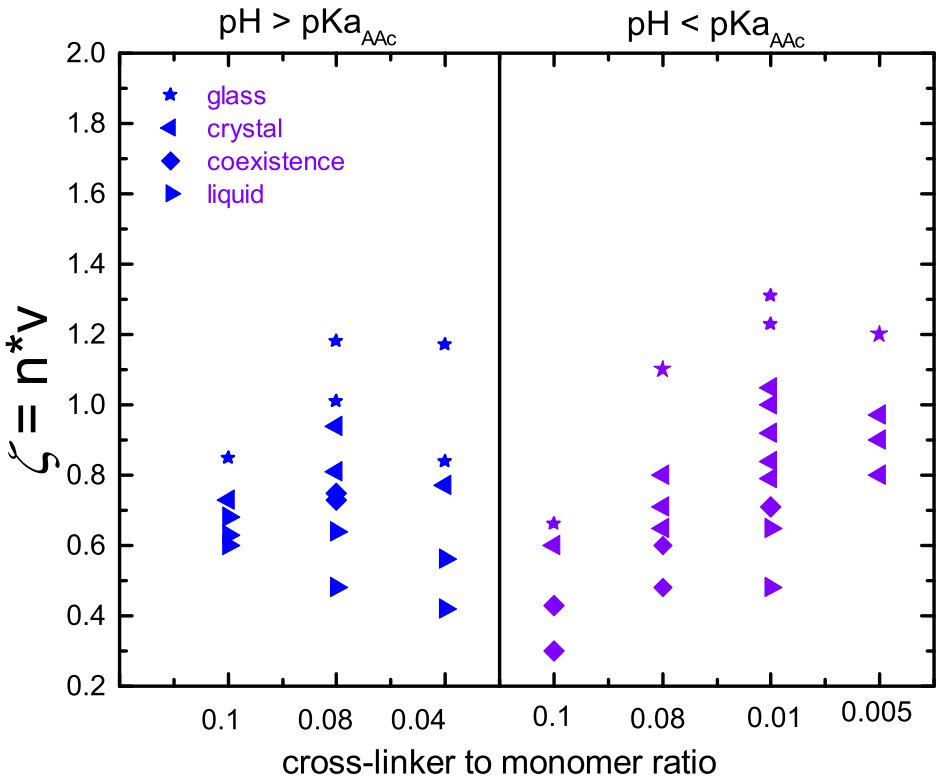

Figure 7.6: Mean squared displacement as a function of concentration.

Chapter 8

Atomic Force Microscopy (AFM) of microgles

In this section we discuss our Atomic Foce Microscopy experiments involving the microgel particles. The motivation for this experiment is the ability to measure molecular level traction forces with AFM. If it is possible to do it on molecules, it should then be possible to do it on microgels! The goal of the experiments is two fold: first we would like to quantify the stiffness of the microgel particles, and second, we would like to measure the interaction potential between particles. Here, we report results on the first.

8.1 Methods

In general, we need to find a way to immobilize the particles onto the surface of a coverslip in a wet environment so that they are well positioned for probing with

the cantilever on the AFM. To do this, the coverslips need to be functionalized with amine groups which can then covalently bond to the carboxyl-rich particles.

- Get ready with tweezers, coverslips, and some ethanol. Heat Oven to 90° C for about 10 min.
- Clean both sides of the coverslips with mill-Q water. Repeat with ethanol.
- Dry in over for 5 min.
- Prepare ethanol in petridish. Take out coverslips and clean them in the ethanol.
- Put the coverslips back in the oven, and place a few drops of Aminosaline on the surface.
- Leave in oven for about 10 min or until dry. Take out and put in petridish.

Aminosilane creates the functional groups on the surface of the coverslips. The sample has to be submerged in a buffer solution during the AFM experiments. In addition to keeping a wet environment, the buffer solution will deprotonate the carboxyls (-COOH) on the microgels, an action needed to effect binding of the particles to the glass surface.

- 1 ml of solvent (buffer solution) and add 3-5 mg of N-hydroxysuccinimide (NHS) and 20-50 mg of 1-Ethyl-3-[3-dimethylaminopropyl]carbodiimide (EDC).
- EDC activates the carboxyl groups of the particles for reaction with the amines. NHS serves as a facilitator by creating intermediate esters that speed up the deprotonation.

- Mix this solution with a very dilute sample.

The basic steps for doing AFM on microgels are summarized below.

- Prepare the buffer solution described above. Rinse salinated coverslip with DI water.
- Put a drop on the salinated surface. Keep in petridish.
- Load cantilever. Position and tune. Do this on an empty coverslip.
- Put salinated coverslip loaded with sample. Put extra buffer solution on top of sample. Approach with cantilever tip. Monitor tip on the computer screen while approaching. Make sure the tip breaks into the solvent.
- Once inside the solution, scan and adjust parameters: find resonance, align laser on cantilever, check signal strength is to spec, and approach and scan.
- A typical frequency spectrum of the cantilever is shown in figure 8.2.

An attempt was made to use a cantilever with a very small force constant, assuming very floppy microgels. The cantilever has a wide rim making it extremely challenging to attach it only to a single particle. Instead, we chose to use a cantilever with a sharp tip as shown in figure 8.1. This made isolation and scanning of single particles much simpler.

A test image of a well defined square well array is shown in figure 8.3.

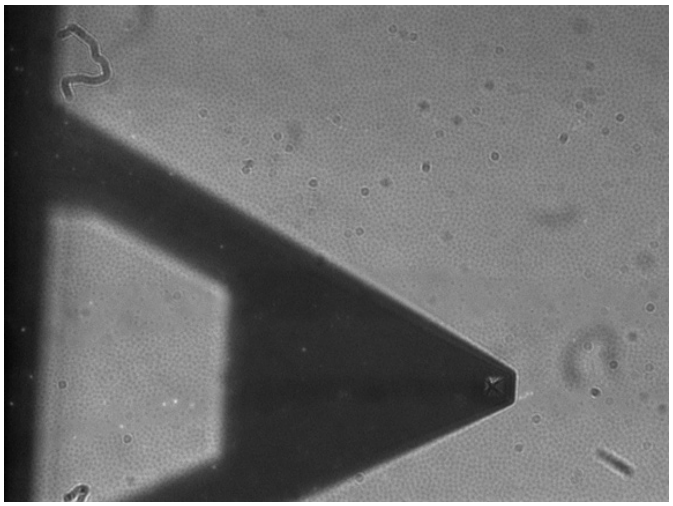

Figure 8.1: A cantilever with a sharp tip.

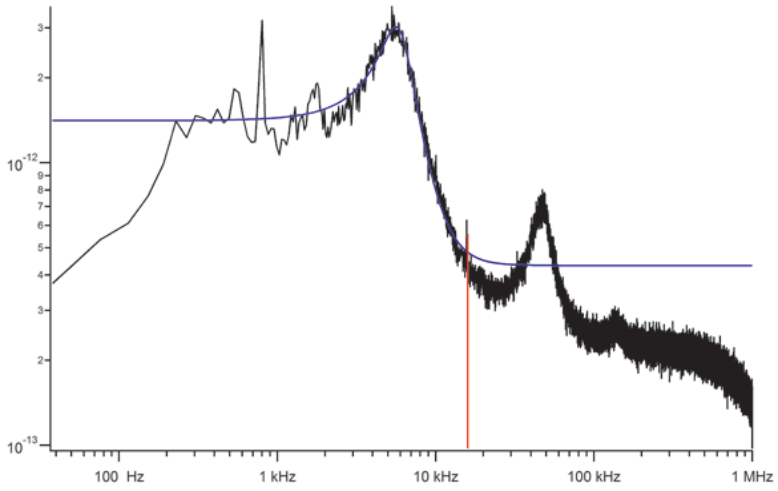

Figure 8.2: Thermal response of the cantilever used to set the scanning frequency.

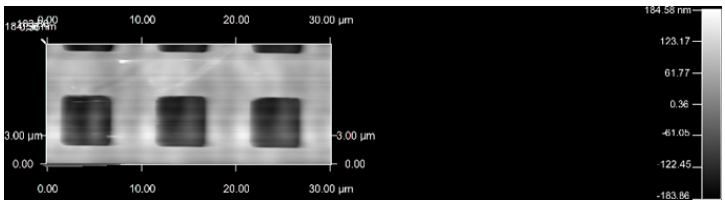

Figure 8.3: A typical test image.

8.2 Results and discussion

A confocal image of the sample ready to be imaged under the AFM is shown in figure 8.4. The sample is sparsely populated as required for these measurements.

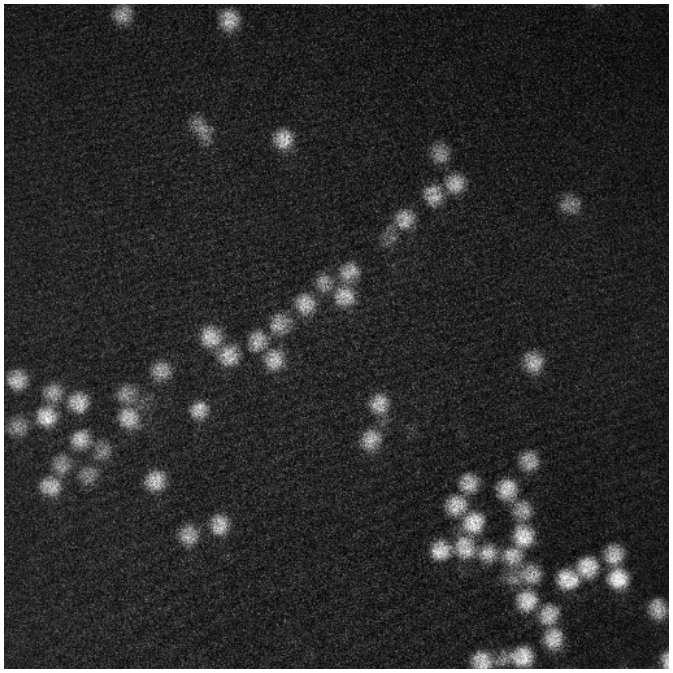

Figure 8.4: A typical confocal image of a sample prepared for AFM scanning.

An AFM image of the 4% b:n sample is shown in figure 8.5. The scanning is done in the horizontal direction (right to left in the figure). As a result, the particles seem to be pulled towards one direction. The cantilever is likely to drag the particle along with it. This is not the case for the sample with 10% b:n for which the AFM image is shown in figure 8.6. The stiffer the particles get, the harder it is to pull them along. Alternatively, the stiffer the particles, the less hairy extensions they posses as discussed previously and hence the less likely it is for the cantilever to grab onto them.

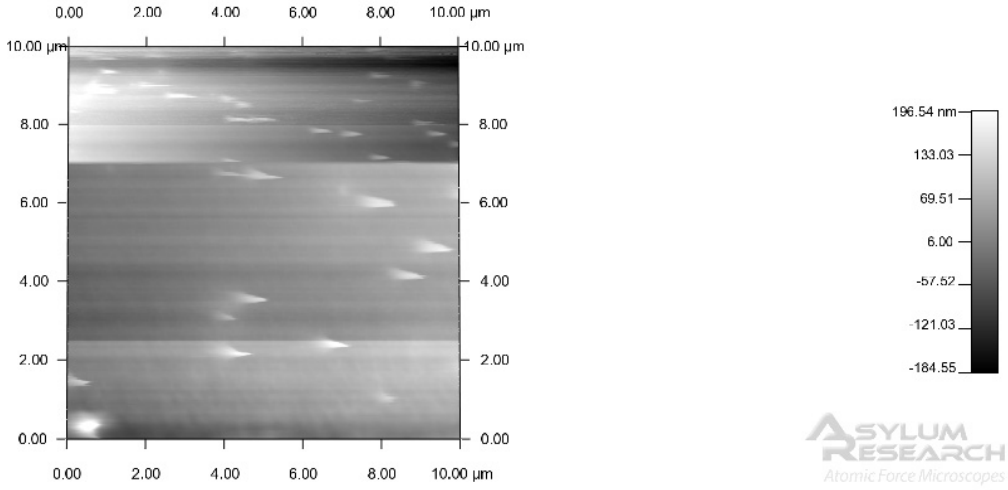

Figure 8.5: AFM image of a 4% b:n sample.

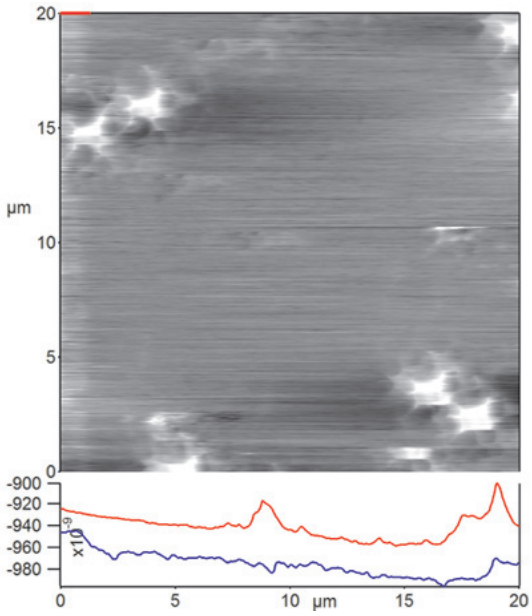

Figure 8.6: AFM image of a 10% b:n sample.

Force curves

The main motivation of these experiments, as stated earlier, is measurement of the stiffness of the particles and possibly the interaction potential between them. To measure stiffness, indentation experiments on single particles are conducted. The force curve as the cantilever moves closer and away from a smooth coverslip is shown in figure 8.7. The vertical axis represents the deflection of the cantilever while the bottom axis shows the distance from the reference "zero" position. The deflection curve as the cantilever approaches the surface is shown in red. No deflection is observed before approximately 0.1 μm from the coverslip, at which point the cantilever experiences a sharp but small deflection as van der waals force pulls it into the coverslip. On further push, the cantilever bends up as shown by the portion of the red line with non-zero slope. When the bending reaches a set value, the piezo of the AFM pulls back on the cantilever. The retraction is represented by the blue curve. As we pull away, the van der waals foce is more effective in deterring the movement of the tip, effectively attaching the cantilever to the coverslip until the distance from the reference is 3.35 μm, at which point the bending-restoring force is able to snap the cantilever off of the coverslip (the sharp rise of the deflection to zero).

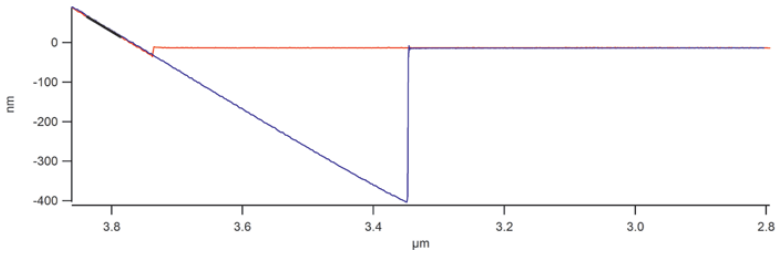

Figure 8.7: Deflection curve of a cantilever on a coverslip.

We locate particles by moving the cantilever around and tapping into the surface, and looking at the shape of the force curve. If the curve looks like that shown in figure 8.7, the cantilever is pulled back and relocated. The force curve of a soft particle is shown in figure 8.8. The contact points are much smoother. Also, the approach and the retraction curves have very similar shape. The force curves are used to determine the stiffness of the probed particle. For an approximation where both the cantilever head and the particle are thought of as spherical in shape, the force can be described by the Hertzian model.

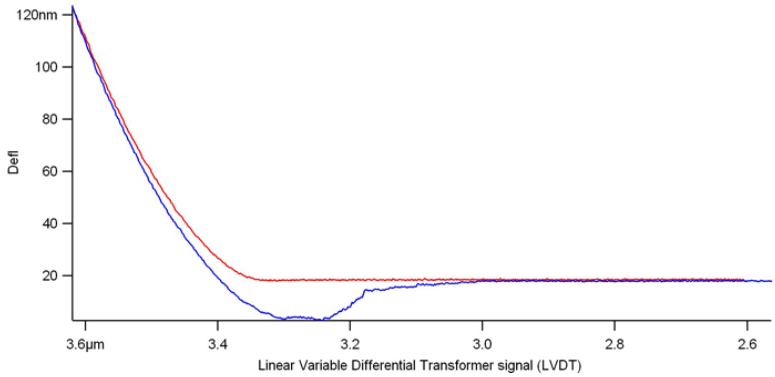

Figure 8.8: Force curve as a result of contact with a particle.

$$F = \lambda \delta^{3/2} \tag{8.1}$$

where λ is given by $4E/3(1-\nu^2)$, where ν is Poisson's ratio and E is Young's modulus. δ is indentation depth. After fitting the curves as shown in figure 8.9, we find:

$$E = 143 \pm 17 \text{ kPa} \tag{8.2}$$

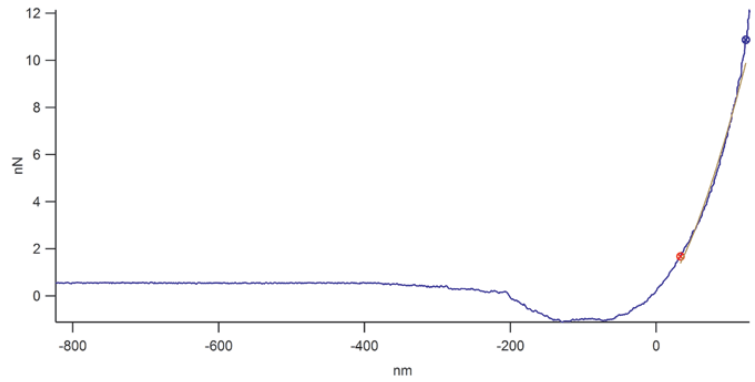

Figure 8.9: Force fit of deflection curve of a cantilever on a coverslip.

Acknowledgement

I thank Dr Claudia Friedsam for showing me how to conduct AFM measurement in a wet environment.

Chapter 9

Summary, current experiments, and future directions

9.1 Summary

In this thesis, I have presented the results of the study on packing structure and dynamics of suspensions of p(NIPAm-co-AAc) microgel particles of diameter 1.0 - 1.5 μm. Using light scattering and confocal microscopy combined with particle tracking techniques, we find that these specific class of colloidal particles show suspension relaxation behavior that depends on concentration and pH. The higher the concentration, the slower the dynamics. At high enough concentrations (usually around $\zeta \sim 1.5$) the suspensions arrest to form a disordered solid. No relaxation is observed on the order of several hours. This is reminiscent of the dynamics of suspensions of hard-sphere colloids, albeit the difference in the concentrations where transitions occur.

In addition, the higher the concentration, the smaller the sizes of the particles as observed from images of successively more concentrated samples. Regardless, this ability of the particles to shrink does not influence the suspension dynamics which remains arrested past a critical concentration. Deviation from a spherical shape past the random close packing density is possible but direct observation of this is difficult due to the invisibility of the periphery of the particles in the confocal microscope.

The dynamics also depend on the charge on the particles. At low pH and hence low charge on the particles, attraction induced nucleation and growth of crystals dominates the evolution of the dynamics. The full dynamic range, from purely diffusive to completely arrested, can be observed within several ours for the same suspension. It takes only approximately 12 hours for this process to finish and the sample usually arrests with the formation of a polycrystalline solid. Hence, for the attractive samples, two factors play a role in determining the dynamics: interaction potential and concentration.

The crystals formed by the microgels are surprisingly insensitive to concentration, charge, and composition of the particles and remain FCC under all conditions. This is confirmed by calculating the pair correlation function across a range of samples. In attractive conditions and at very low concentrations, polycrystalline solids result. In general the lower the concentration, the more common are defects and dislocations. For repulsive particles, large single crystals are formed entropically. There is a critical concentration beyond which crystallization is no longer favored and glassy soft solids form. To obtain crystals at high concentrations, one can apply external osmotic pressure to already crystallized samples. The ability of the particles to shrink allows

a degree of flexibility that enables the suspensions to maintain FCC crystal structures even when the concentration has reached as high as $\zeta = 1.73$.

These results illustrate the relationship between dynamics and structure in soft colloidal suspensions. In addition to enhancing our ability to use the suspensions to modify properties of industrial products, they inform us on how to use them to better model atomic and molecular materials.

9.2 Current preliminary results

Recently, I have been involved in integrating macro- and micro- gels with Carbon Nanotubes (CNTs) in order to modify the electrical as well as thermal properties of the gels. We have been able to successfully integrate p(NIPAm-co-AAc) onto the surface of carbon nanotubes as confirmed by size measurements before and after the integration procedure (not shown here). We also have made micogels composed of CNTs and p(NIPAm-co-AAc) polymers. We found out that the pH and thermal response of these particles is similar to those made without CNTs (figures 9.1 and 9.2). We are in the process of testing the electrical and thermal response of these particles.

Macrogels of NIPAm and NIPAm-CNT base polymers were made and their rheological properties compared. Figures 9.3 and 9.4 show strain response as the shear is increased. The pure NIPAm gel shows a response that is smoothly changing with no clear distinction between linear and nonlinear regimes. By contrast, the NIPAm-CNT gel exhibits a clear distinction between the two regimes. This difference in the rheological characteristics can also be discerned by a subjective experiment: a tap

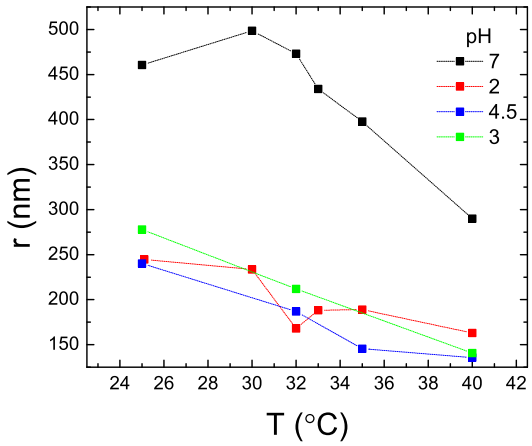

Figure 9.1: pH and temperature response of microgels containing CNT.

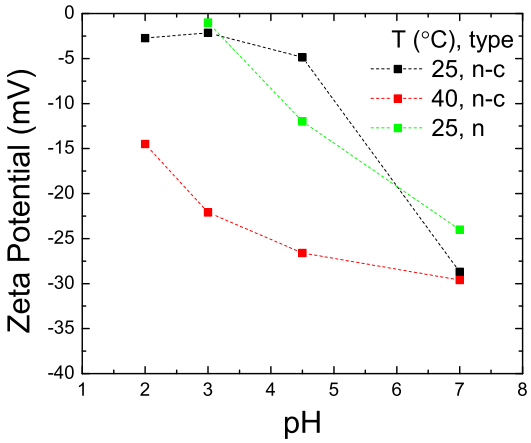

Figure 9.2: pH influence on zeta potential of microgels containing CNT.

on the containers produces last longing vibrations in the case of the NIPAm-CNT based macrogels while these vibrations are short lived and weak in the case of the pure NIPAm based macrogels. This shows that the first tend to effectively transmit the imparted energy while the latter absorb it.

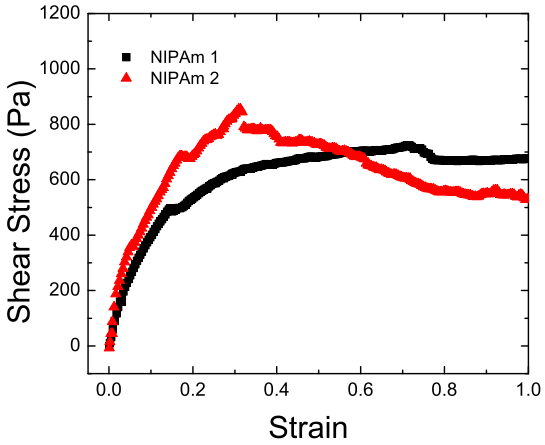

Figure 9.3: Rheology of pure NIPAm macrogel.

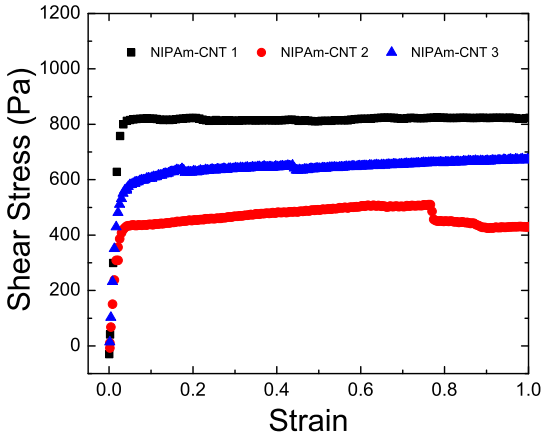

Figure 9.4: Rheology of NIPAm-CNT macrogel.

However, the moduli of the two systems do not show appreciable differences (only approximately a factor of 2 difference) as can be seen in figures 9.5 and 9.6. The

values are extracted from the stress-strain plots by doing a fit to the linear regimes (or low strain values). The frequency responses (not shown here) give similar moduli values.

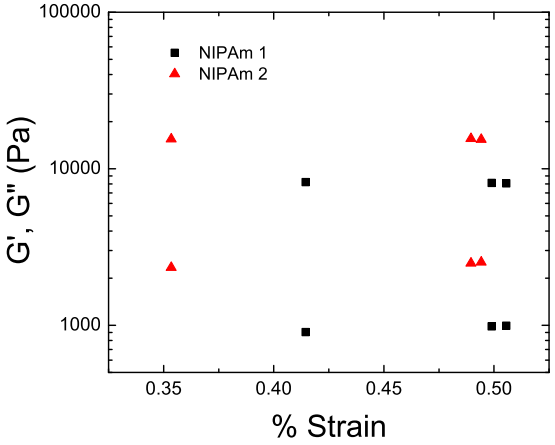

Figure 9.5: Rheology of pure NIPAm macrogel.

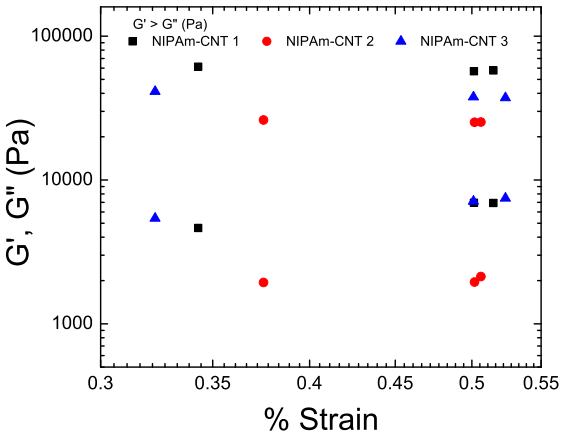

Figure 9.6: Rheology of NIPAm-CNT macrogel.

Aside

Scanning electron microscope images of the freeze dried p(NIPAm-co-AAc) microgel suspensions display remarkable features as in figures 9.7 and 9.8 (image credit: Michael De Volder). I imaged the warming up process of the frozen sample and did not observe a phase separation that could have potentially caused the features seen in the SEM images. The background physics for this phenomena has to be determined before we can discuss the data in detail.

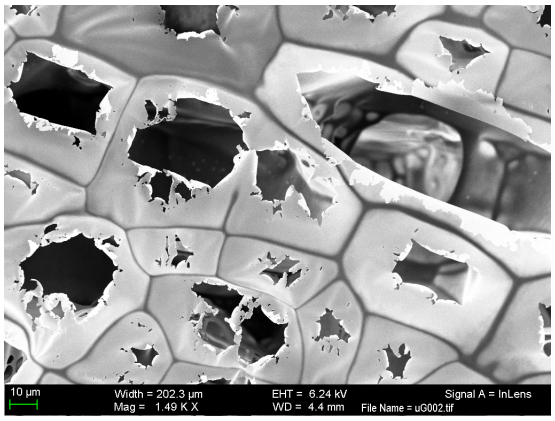

Figure 9.7: SEM image of a freeze dryed microgel suspension.

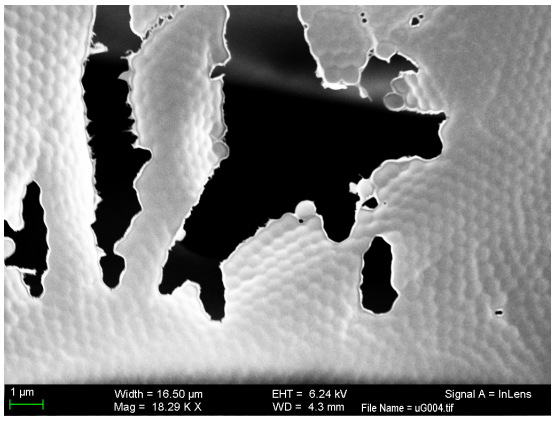

Figure 9.8: A closer look reveals individual particles.

9.3 Future directions

The extra degrees of freedom introduced as a result of deformability of the microgels could be exploited for modeling the diverse phase behavior of atomic and molecular materials. To do this, the relevant parameters of the colloidal systems need to be identified and controlled. Size and pH play detrimental roles in the phase behavior. For example, to mimic the fragility behavior of glass formers, researchers employed particles of size about 90 nm in radius and controlled the stiffness by changing the chemical composition [39]. To reproduce the results using confocal microscopy and to be able to make doubtless comparison of the microscopic data with the scattering data, our experiments indicate that it is important to employ the same type of particles as in the scattering experiments. To improve quality of images, one could use fluorescent tracer particles dispersed in the suspension. The pH of the suspension should be duly monitored.

Conjugating NIPAm-co-AAc polymers with structures such as CNTs provides an interesting platform with potential technological and biological applications. An

example of such applications is an extra cellular matrix that is composed of CNTs and methacrylate [61]. The mechanical behavior, electrical properties, and texture of the gel can be controlled by altering the proportion of CNTs.

Bibliography

[1] C. Allain, M. Cloitre, and M. Wafra. Aggregation and sedimentation in colloidal suspensions. *Physical Review Letters*, **74**(8):1478–1481, 1995.

[2] A.M. Alsayed, M. F. Islam, J. Zhang, P.J. Collings, and A. G. Yodh. Premelting at defects within bulk colloidal crystals. *Science*, **309**:1207–1210, 2005.

[3] C. A. Angell. Formation of glasses from liquids and biopolymers. *Science*, **267**(5206):1924–1935, 1995.

[4] C. A. Angell, K. L. Ngai, G. B. McKenna, P. F. McMillan, and S. W. Martin. Relaxation in glassforming liquids and amorphous solids. *Jornal of Applied Physics*, **88**(6):3113–3157, 2000.

[5] P. Bradna, P. Stern, O. Quadrat, and J. Snuparek. Thickening effect of dispersions of ethyl acrylate-metacrylic acid copolymer prepared by different polymerization routes. *Colloid and Polymer Science*, **273**(4):324–330, 1995.

[6] P. M. Chaikin and T. C. Lubensky. *Principles of condensed matter physics*. Principles of condensed matter physics. Cambridge University Press, Cambridge, 1997.

[7] A. Chilkoti, M.R. Dreher, D.E. Meyer, and D. Raucher. Targeted drug delivery by thermally responsive polymers. *Advanced drug delivery reviews*, **54**:613–630, 2002.

[8] Jae Kyu Cho, Zhiyong Meng, L. Andrew Lyon, and Victor Breedveld. Tunable attractive and repulsive interactions between ph-responsive microgels. *Soft Matter*, **5**(19):3599–3602, 2009.

[9] Michel Cloitre, Regis Borrega, and Ludwik Leibler. Rheological aging and rejuvenation in microgel pastes. *Physical Review Letters*, **85**(22):4819–4822, 2000.

[10] Michel Cloitre, Regis Borrega, Fabrice Monti, and Ludwik Leibler. Glassy dynamics and flow properties of soft colloidal pastes. *Physical Review Letters*, **90**(6), 2003.

[11] R. Colin, Alsayed A.M., and J.C. Castaing. Spatially heterogeneous dynamics in a thermosensitive soft suspension before and after glass transition. *Soft Matter*, **7**:4504–4514, 2011.

[12] John C. Crocker and David G. Grier. Methods of digital video microscopy for colloidal studies. *Jornal of Colloid and Interface Science*, **179**:298–310, 1996.

[13] Mallika Das, Hong Zhang, and Eugenia Kumacheva. Microgels: Old materials with new applications. *Annual Review of Materials Research*, **36**:117–142, 2006.

[14] A. R. Denton. Counterion penetration and effective electrostatic interactions in solutions of polyelectrolyte stars and microgles. *Physical Review E*, **67**:011804, 2003.

[15] Jan K. G. Dhont. In *An introduction to dynamics of colloids*, Studies in interface science, pages 107–170. Elsevier, Amsterdam, 1996.

[16] David Duracher, Abdelhamid Elaissari, and Christian Pichot. Preparation of poly(n-isopropylmethacrylamide) latexes kinetic studies and characterization. *Journal of Polymer Science Part A: Polymer Chemistry*, **37**:1823, 1999.

[17] Albert Einstein. On the movement of small particles suspended in stationary liquids required by the molecular-kinetic theory of heat. *Annalen der Physik*, **17**:549–560, 1905.

[18] Brian M. Erwin, Dimitris Vlassopoulos, and Michel Cloitre. Rheological fingerprinting of an aging soft colloidal glass. *J. Rheol.*, **54**(4):915–939, 2010.

[19] Markus Franke, Achim Lederer, and Hans Joachim Schope. Heterogeneous and homogeneous crystal nucleation in colloidal hard-sphere like microgels at low metastabilities. *Soft Matter*, **7**(23):11267–11274, 2011.

[20] U Gasser, Andrew Schofield, and D A Weitz. Local order in a supercooled colloidal fluid observed by confocal microscopy. *Journal of Physics: Condensed Matter*, **15**:S375–S380, 2002.

[21] U. Gasser, Eric R. Weeks, Andrew Schofield, P. N. Pusey, and D. A. Weitz. Real-space imaging of nucleation and growth in colloidal crystallization. *Science*, **292**(5515):258–262, 2001.

[22] S.C. Glotzer and M.J. Solomon. Anisotropy of building blocks and their assembly into complex structures. *Nature*, **6**:557–562, 2007.

[23] D Gottwald, C N Likos, G Kahl, and H Lowen. Ionic microgels as model systems for colloids with an ultrasoft electrosteric repulsion: Structure and thermodynamics. *Journal of Chemical Physics*, **122**:074903–10, 2005.

[24] D. Gottwald, C.N. Likos, G. Kahl, and H. Lowen. Phase behavior of ionic microgels. *Physical Review Letters*, **92**(6):068301–4, 2004.

[25] Y. Han, N. Y. Ha, A. M. Alsayed, and A. G. Yodh. Melting of two-dimensional tunable-diameter colloidal crystals. *Physical Review E*, **77**:41406, 2008.

[26] J. L. Harland and W. van Megen. Crystallization kinetics of suspensions of hard colloidal spheres. *Physical Review E*, **55**(3):3054–3065, 1997.

[27] Hsien Hsueh Lee, Kan-Sen Chou, and Kuo-Cheng Huang. Inkjet printing of nanosized silver colloids. *Nanotechnology*, **16**:2436–2441, 2005.

[28] Ashlee St. John Iyer and L. Andrew Lyon. Self-healing colloidal crystals. *Angewandte Chemie International Edition*, **48**:4562–4566, 2009.

[29] J Jackle. Models of the glass transition. *Rep. Prog. Phys.*, **49**:171–231, 1986.

[30] Ashlee N. St. John, Victor Breedveld, and L. Andrew Lyon. Phase behavior in highly concentrated assemblies of microgels with soft repulsive interaction potentials. *Jornal of Physical Chemistry B*, **111**(27):7796–7801, 2007.

[31] C.P. Lapointe, T. G. Mason, and I.I. Smalyukh. Shape-controlled colloidal interactions in nematic liquid crystals. *Science*, **326**:1083–1086, 2009.

[32] A.K. Lele, M.M. Hirve, M.V. Badiger, and R.A. Mashelkar. Predictions of bound water content in poly(n-isopropylacrylamide) gel. *Macromolecules*, **30**(1):157–159, 1997.

[33] J. Liu, D. A. Weitz, and B.J. Ackerson. Coherent crystallography of shear-aligned crystals of hard-sphere colloids. *Physical Review E*, **48**(2):1106–1114, 1993.

[34] Yoav D. Livney, Ory Ramon, Ellina Kesselman, Uri Cogan, Shimon Mizrahi, and Yachin Cohen. Swelling of dextran gel and osmotic pressure of soluble dextran in the presence of salts. *Journal of Polymer Science Part B: Polymer Physics*, **39**:2740–2750, 2001.

[35] Peter J. Lu, Peter A. Sims, Hidekazu Oki, James B Macarthur, and David A Weitz. Target-locking acquisition with real-time confocal (tarc) microscopy. *Optics Express*, **15**(14):8702–8712, 2007.

[36] P.J. Lu, J.C. Conrad, H.M. Wyss, A.B. Schofield, and D.A Weitz. Fluids of clusters in attractive colloids. *Physical Review Letters*, **96**:028306, 2006.

[37] L. Andrew Lyon, Justin D. Debord, Saet Byul Debord, Clinton D. Jones, Jonathan G. McGrath, and Michael J. Serpe. Microgel colloidal crystals. *Journal of Physical Chemistry B*, **108**(50):19099–19108, 2004.

[38] T. G. Mason and M. Y. Lin. Density profiles of temperature-sensitive microgel particles. *Physical Review E*, **71**:040801, 2005.

[39] Johan Mattsson, Hans M. Wyss, Alberto Fernandez-Nieves, Kunimasa Miyazaki, Zhibing Hu, David R. Reichman, and David A. Weitz. Soft colloids make strong glasses. *Nature*, **462**:83–86, 2009.

[40] W. van Megen and P. N. Pusey. Dynamic light-scattering study of the glass transition in a colloidal suspension. *Physical Review A*, **43**(10):5429, 1991.

[41] W. van Megen and S.M. Underwood. Glass transition in colloidal hard spheres: Measurement and mode-coupling-theory analysis of the coherent intermediate scattering function. *Physical Review E*, **49**(5):4206, 1994.

[42] Zhiyong Meng, Jae Kyu Cho, Victor Breedveld, and L. Andrew Lyon. Physical aging and phase behavior of multiresponsive microgel colloidal dispersions. *Journal of Physical Chemistry B*, **113**:4590–4599, 2009.

[43] Zhiyong Meng, Jae Kyu Cho, Stella Debord, Victor Breedveld, and L. Andrew Lyon. Crystallization behavior of soft, attractive microgels. *Journal of Physical Chemistry B*, **111**(25):6992–6997, 2007.

[44] M. Minsky. Memoir on inventing the confocal scanning microscope. *Scanning*, **10**(4):128–138, 1998.

[45] P. S. Mohanty and W. Richtering. Structural ordering and phase behavior of charged microgels. *Journal of Physical Chemistry B*, **112**(47):14692–14697, 2008.

[46] M. Muluneh, J. Sprakel, H.M. Wyss, J Mattsson, and D.A. Weitz. Direct visualization of ph-dependent evolution of structure and dynamics in microgel suspensions. *Journal of Physics: Condensed Matter*, **23**(50):505101, 2011.

[47] M. Muluneh and D.A. Weitz. Direct visualization of theree dimensional crystallization behavior in microgels. *Physical Review E*, **85**(2):021405–6, 2012.

[48] Hiroyuki Ohshima, Thomas W. Healy, and Lee R. White. Accurate analytic expressions for the surface charge density/surface potential relationship and double-layer potential distribution for a spherical colloidal particles. *Journal of Colloid and Interface Science*, **90**(1):17–26, 1982.

[49] Robert Pelton. Temperature-sensitive aqueous microgels. *Advances in Colloid and Interface Science*, **85**:1–33, 2000.

[50] Jerome K. Percus and George J. Yevick. Analysis of classical statistical mechanics by means of collective coordinates. *The Physical Review*, **110**(1), 1958.

[51] Eko H. Purnomo, Dirk van den Ende, Siva A. Vanapalli, and Frieder Mugele. Glass transition and aging in dense suspension of thermosensitive microgel particles. *Physical Review Letters*, **101**, 2008.

[52] P. N. Pusey and W. van Megen. Observation of a glass transition in suspensions of spherical colloidal particles. *Physical Review Letters*, **59**(18), 1987.

[53] P. N. Pusey, W. van Megen, P. Bartlett, B. J. Ackerson, J. G. Rarity, and S. M. Underwood. Structure of crystals of hard colloidal spheres. *Physical Review Letters*, **63**(25):2753–2756, 1989.

[54] Dale W. Schaefer. Colloidal suspensions as soft core liquids. *Journal of Chemical Physics*, **66**(9):3980–3984, 1977.

[55] Peter Schall, Itai Cohen, David A. Weitz, and Frans Spaepen. Visualization of dislocation dynamics in colloidal crystals. *Science*, **305**:1944–1948, 2004.

[56] Stephan Schmidt, Thomas Hellweg, and Regine von Klitzing. Packing density control in p(nipam-co-aac) microgel monolayers: Effect of surface charge, ph, and preparation technique. *Langmuir*, **24**(21):12595–12602, 2008.

[57] Hans Joachim Schope, Gary Bryant, and William van Megen. Two-step crystallization kinetics in colloidal hard-sphere systems. *Physical Review Letters*, **96**(17):175701, 2006.

[58] D. Semwogerere and E.R. Weeks. Confocal microscopy. *Encyclopedia of Biomaterials and Biomedical Engineering by Taylor and Francis*, 2005.

[59] H. Senff and W. Richtering. Influence of corss-link density on rheological properties of temperature-sensitive microgel suspensions. *Colloid and Polymer Science*, **278**:830–840, 2000.

[60] David A. Sessoms, Irmgard Bischofberger, Luca Cipelletti, and Veronique Trappe. Multiple dynamic regimes in concentrated microgel systems. *Philosophical Transactions of The Royal Society A*, **367**:5013–5032, 2009.

[61] Su Ryon Shin, Hojae Bae, Jae Min Cha, Ji Young Mun, Ying-Chieh Chen, Halil Tekin, Hyeongho Shin, Saeed Farshchi, Mehmet R. Dokmeci, Shirley Tang, and Ali Khademhosseini. Carbon nanotube reinforced hybrid microgels as scaffold materials for cell encapsulation. *American Chemical Society Nano*, **6**(1):362–372, 2012.

[62] Benjamin Sierra-martin, Justin A. Frederick, Yesenia Laporte, George Markou, Juan Jose Leitor-Santos, and Alberto Fernandez-Nieves. Determination of the bulk modulus of microgel particles. *Colloid and Polymer Science*, **289**(5-6):721–728, 2011.

[63] Martin J. Snowden, Babur Z. Chowdhry, Brian Vincent, and Gayle E. Morris. Colloidal copolymer microgels of n-isopropylacrylamide and acrylic acid: ph, ionic strength and temperature effects. *Journal of the Chemical Society, Faraday Transactions*, **92**(24):5013–5016, 1996.

[64] Paul J. Steinhardt, David R. Nelson, and Marco Ronchetti. Bond-orientational order in liquids and glasses. *Physical Review B*, **28**(2):784–805, 1983.

[65] Markus Stieger, Walter Richtering, Jan Skov Pedersen, and Peter Linder. Small-angle neutron scattering study of structural changes in temperature sensitive microgel colloids. *Jornal of Chemical Physics*, **120**(13):6197–6206, 2004.

[66] Tharwat Tadros. Colloid aspects of csmetic formulations with particular reference to polymeric surfactants. *Colloids and Interface Science Series, Wiley-VCH Verlag GmbH and Co.*, **4**, 2008.

[67] Tharwat Tadros. Colloids in paints. *Colloids and Interface Science Series, Wiley-VCH Verlag GmbH and Co.*, **6**, 2010.

[68] T. Tanaka and Fillmore D.J. Kinetics of swelling of gels. *Journal of Chemical Physics*, **70**(3):1214–1218, 1979.

[69] Shijun Tang, Zhibing Hu, Zhengdong Cheng, and Jianzhong Wu. Crystallization kinetics of thermosensitive colloids probed by transmission spectroscopy. *Langmuir*, **20**(20):8858–8864, 2004.

[70] Everett Thiele. Equation of state for hard spheres. *The Journal of Chemical Physics*, **39**(2):474–479, 1963.

[71] Rein V. Ulijn, Nurguse Bibi, Vineetha Jayawarna, Paul D. Thornton, Simon J. Todd, Robert J. Mart, Andrew M. Smith, and Julie E Gough. Bioresponsive hydrogels. *Materialstoday*, **10**(4), 2007.

[72] Yanting Wang, S. Teitel, and Christoph Dellago. Melting of icosahedral gold nanoclusters from molecular dynamics simulations. *The Journal of Chemical Physics*, **122**(214722), 2005.

[73] Eric R. Weeks, J. C. Crocker, Andrew C. Levitt, Andrew Schofield, and D. A. Weitz. Three-dimensional direct imaging of structural relaxation near the colloidal glass transition. *Science*, **287**, 2000.

[74] Patrick Wette, Andreas Engelbrecht, Roushdey Salh, Ina Klassen, Dirk Menke, Dieter M Herlach, Stephan V Roth, and Hans Joachim Schope. Copetition between heterogeneous and homogeneous nucleation near a flat wall. *Jornal of Physics: Condesned Matter*, **21**(46):464115, 2009.

[75] Jianzhong Wu, Bo Zhou, and Zhibing Hu. Phase behavior of thermally responsive microgel colloids. *Physical Review Letters*, **90**(4):048304, 2003.

[76] X. Wu, R. H. Pelton, A. E. Hamielec, D. R. Woods, and W. McPhee. The kinetics of poly(n-isopropylacrylamide) microgel latex formation. *Colloid and Polymer Science*, **272**:467–477, 1994.

[77] Hans M. Wyss, Daniel L. Blair, Jeffrey F. Morris, Howard A. Stone, and David A. Weitz. Mechanism for clogging of microchannels. *Physical Review E*, **74**(6), 2006.

[78] Lei Xu, Simon Davies, Andrew B. Schofield, and David A. Weitz. Dynamics of drying in 3d porous media. *Physical Review Letters*, **101**:094502, 2008.

[79] Peter Yunker, Zexin Zhang, Kevin B. Aptowicz, and A. G. Yodh. Irreversible rearrangments, correlated domains, and local structure in aging glasses. *Physical Review Letters*, **103**, 2009.

[80] Zexing Zhang, Ning Xu, Daniel T. N. Chen, Peter Yunker, Ahmed M. Alsayed, Kevin B. Aptowicz, Piotr Habdas, Andrea J. Liu, Sidney R. Nagel, and Arjun G. Yodh. Thermal vestige of the zero-temperature jamming transition. *Nature*, **459**:230–233, 2009.

Appendix A

MATLAB and IDL routines

The following codes are referred to in various points in the thesis. They are preceded by short descriptions to clarify their purpose.

MATLAB codes To rename a series of tiff files...

```
function batch_maker(stem,frames,stacks,outstem)

%rewrite filenames from leica confocal into a form for PLuTARC
%Leica naming format: stem_z#_t#_ch00.tif
%           also other formats for time series or single stack
bname=[stem,'_renamer.bat'];
fid=fopen(bname,'w');
sd=4;
fd=3;
num=0;
for s=1:stacks
   for f=1:frames
       num=num+1;
       %oldfile is the format for the original image filename
       oldfile=[stem,'_',n2s(num,4),'.tif'];
       newfile=[outstem,'_',n2s(f,3),'_',n2s(s,6),'.tif'];
       fprintf(fid,'rename %s %s\n',oldfile,newfile);
   end
end
fclose(fid);
```

```
function [str2]=n2s(k,num)
n=length(num2str(k));
n_of_zeros=num-n;
str1='0';
if n_of_zeros==0
    str2=num2str(k);
else
    for i=1:n_of_zeros-1
        str1= strcat(str1,'0');
    end
    str2=strcat(str1,num2str(k));
end
```

To make stack from a series of tiff images...

```
function make_stack(stem,frames,stacks,outstem)
        num=0;
for s=1:stacks
    stack_name=[outstem,'_',n2s(s,4),'.tif'];
   for f=1:frames
       num=num+1;
       file_name=[stem,'_',n2s(f,3),'_',n2s(s,6),'.tif'];
       image=imread(file_name);
       if f > 1
       imwrite(image,stack_name,'writemode','append');
       else
           imwrite(image,stack_name);
       end
   end
end
```

To calculate mobility of particles as a function of delay time...

```
function Diff = DiffCoef2(tr,timestep,dt)
Length=size(tr(:,1));
length=Length(1,1);


%maxtime=max(tr(:,3));

NumParticle=tr(length,4);

%num_dts=maxtime./timestep;

DiffMat=zeros(NumParticle,5);
```

```
count=1;
countT=1;
nT=1;
k=1;

while count < length
%for n=count:length-1
    id_diff=0;
    n=count;
    t=1;
    while (id_diff == 0) && (count < length)
            id_diff=tr(count+1,4)-tr(count,4);
            timediff = tr(count,3)-tr(n,3);
            if timediff == dt
                %timediff
                t = tr(count-1,3);
                nT=n;
                countT=count;
                k=k+1;
            end
            count=count+1;
    end

    %count, n
    if countT ~= 1
    id=tr(countT,4);
    %t=tr(count-1,3);
    DiffMat(k,1)=id;
    DiffMat(k,2)=tr(countT,1);
    DiffMat(k,3)=tr(countT,2);
    DiffMat(k,4)=(tr(nT,1)-tr(countT,1))^2+(tr(nT,2)-tr(countT,2))^2;
    DiffMat(k,5)=dt*timestep;
    end

end
Diff=DiffMat;
```

To calculate MSD with single-frame delay times (Weeks code calculates for logarithmically spaced delay times)...

```
%Function for calculating MSD for data with random time variable.
function msd = mel_msd(tr,timestep)
Length=size(tr(:,1));
length=Length(1,1);
```

```
%array=[2,3,12,13,14,15,31,32,33,34,35,37,44,45,46,47,48,64,65,68,77];
%dt_array=(array-1)*60;
maxtime=max(tr(:,3));
num_dts=maxtime./timestep;
%Length_dt=size(dt_array);
%length_dt=Length_dt(1,1);
%max_id=max(tr(:,4));
count=0;
dxdy=zeros(num_dts,7);

for m=1:num_dts
    dt=m*timestep;
    num_pts=0;
    for n=1:length-1
        count=n+1;
        id_diff=tr(n+1,4)-tr(n,4);
        while (id_diff == 0) && (count < length)
            delta_t=tr(count,3)-tr(n,3);
        if delta_t == dt
            num_pts=num_pts+1;
            dxdy(m,1)=dxdy(m,1)+(tr(count,1)-tr(n,1));
            dxdy(m,2)=dxdy(m,2)+(tr(count,2)-tr(n,2));
            dxdy(m,3)=dxdy(m,3)+((tr(count,1)-tr(n,1))^2);
            dxdy(m,4)=dxdy(m,4)+((tr(count,2)-tr(n,2))^2);
            dxdy(m,5)=dxdy(m,5)+(((tr(count,1)-tr(n,1))^2)+
            ((tr(count,2)-tr(n,2))^2));
            dxdy(m,6)=num_pts;
            dxdy(m,7)=dt;
        end
        count=count+1;
        id_diff=tr(count,4)-tr(n,4);
        end

    end
   % dxdy(m,[1,5])=dxdy(m,[1,5])/dxdy(m,6);
end
msd=dxdy;
```

To calculate the MSD of single particles...

```
function msd = mel_msd_single(tr,timestep)
Length=size(tr(:,1));
length=Length(1,1);
maxtime=max(tr(:,3));
num_dts=maxtime./timestep;
count=1;
dxdy=zeros(length,4);
```

```
while (count < length-1)
    id_diff=tr(count+1,4)-tr(count,4);
    n=count;
     while (id_diff == 0) && (count < length-1)
         dxdy(count,1)=tr(count+1,3)-tr(n,3);
         dxdy(count,2)=(tr(count+1,1)-tr(n,1));
         dxdy(count,3)=(tr(count+1,2)-tr(n,2));
         dxdy(count,4)=(tr(count+1,1)-tr(n,1))^2+(tr(count+1,2)
                                -tr(n,2))^2;
         dxdy(count,5)= tr(count+1,4);
         count=count+1;
         id_diff=tr(count+1,4)-tr(n,4);
         if (id_diff == 1)
             count = count+1;
         end
     end
end


msd=dxdy;
```

To pick out positions of particles that belong to crystals in a co-existence system....

```
function xtalPos(xyz,cubePos)
k=size(xyz(:,1));
fid1=fopen('XtalPos.txt','w');
count=1;
j=size(cubePos(:));
j=j(1);
for n=1:k
    if count <= j
    L=cubePos(count);
    end
    if (n == L)
    fprintf(fid1,'%2.3f %2.3f %2.3f \n', xyz(n,:));
    count=count+1;
    end
end
fclose(fid1);
end
```

To prepare a script for Aqsis. It takes sorted particle positions and puts in the text at appropriate places...

```
function sorted(xyz,cubePos)
k=size(xyz(:,1));
fid1=fopen('amorophous2.txt','w');
fid2=fopen('crystal2.txt','w');
count=1;
j=size(cubePos(:));
j=j(1);
for n=1:k
    if count <= j
    L=cubePos(count);
    end
    if (n == L)
    fprintf(fid2,'TransformBegin \n');
    fprintf(fid2,'Translate %2.3f %2.3f %2.3f \n', xyz(n,:));
    fprintf(fid2,'ReadArchive "cube.RIB" \n');
    fprintf(fid2,'TransformEnd \n');

    count=count+1;

    else
    fprintf(fid1,'TransformBegin \n');
    fprintf(fid1,'Translate %2.3f %2.3f %2.3f \n', xyz(n,:));
    fprintf(fid1,'Sphere 0.25 -0.25 0.25 360  \n');
    fprintf(fid1,'TransformEnd \n');
    end
end
fclose(fid1);
fclose(fid2);
end
```

To treat crystal coordinates in a unique manner: this takes positions and generates a script for aqsis telling it to render crystals in cubes...

```
function sorted_xtal(xtalPos)

k=size(xtalPos(:,1));
fid2=fopen('crystal_ordered.txt','w');

for n=1:k

fprintf(fid2,'TransformBegin \n');
fprintf(fid2,'Translate %2.3f %2.3f %2.3f \n', xtalPos(n,:));
fprintf(fid2,'ReadArchive "cube.RIB" \n');
fprintf(fid2,'TransformEnd \n');

end
```

```
fclose(fid2);
end
```

For MSD based sorting...

```
function colorcode=crystalfinder(xyz,msd)

%Melaku Muluneh, May 15, 2011
%This program assigns a colorcode to particles based on their MSDs for
%visualizing faster and slower moving particles.

[rows,columns]=size(xyz);
out=zeros(rows,columns);
fl=0.1;
colfl=5;
colcr=25;
t=2;
while t <= rows
    if msd(t,5)==0
        t=t+1;
    else
    out(t,1:3)=xyz(t,1:3);
    m=msd(t,3)/msd(t,5);
        if m < fl
            out(t,4)=colcr;
        else
            out(t,4)=colfl;
        end
         t=t+1;
    end

end
colorcode=out;
```

To calculate the voroni area associated with 2D image sequences. This is actually never directly presented in the thesis.

```
% vorn_area: Calculates the area of the voronoi cells in 2d.
% It cleans up the data by ignoring infinities from edges
%    truncates areas at a=5 micron^2 (not statistically significant).
% Input should be an Nx2 array of N positions - should be in Microns.
%
% Melaku Muluneh
```

```
% 02/12/10

function pos_area=vorn_area(xy)
[v,c]=voronoin(xy);
ncell=length(xy(:,1));
xya=xy;
for k=1:ncell
    X = v(c{k},:);
    if ~isinf(X)
        [K,a]=convhull(v(c{k},1),v(c{k},2));
        xya(k,3)=a;
        if a < 5
            %sometimes a is so big making it difficult to do
            %statistical plot.
            xya(k,3)=a;
        else
            xya(k,3)=0;
        end
    else
        xya(k,3)=0;
    end
end
pos_area = xya;
```

The following are IDL codes. Some are referred to in the thesis.

To bin the colorcoded particle positions for analysis of crystal fraction....

```
function bin_colorcode,xyc

;Melaku Muluneh, May 16, 2011
;Takes data with x,y,t,...,code, bins the code for each t and returns
; binvalues as a function time, t

nbin=Long(max(xyc(2,*)))


dist = dblarr(3,nbin+1)
an=dblarr(1,nbin)
for n = 3L,nbin do begin
w = where(xyc(2,*) eq n)
an=xyc(3,w)
hist=histogram(an,binsize=15)
k=n_elements(hist)

    if k eq 1 then begin
       dist(0,n)=n
```

```
        dist(1,n)=hist(0)
    endif else begin
        dist(0,n)=n
        dist(1,n)=hist(0)
        dist(2,n)=hist(1)
    endelse

endfor
return,dist
end
```

To calculate the 2-point correlation between displacements of particles. The result is briefly included in chapter 7.

```
function dispcorr1, in_plane,max_dr,w1,w2,ninit_t,nfinal_t,nbin

; Calculates the displacement correlation between particles
; from tracked data for a fixed time gap.

; A quasi 2D plane is defined.

; The correlation function in this case is defined
; as the dot product of the displacements of the
;particles for the specified time.

; The average is taken over all particles
; of a fixed distance separation.
; This is normalized by dividing by the average of the
; displacements of all the particles.

;Inputs:

; tr is the file containing info on tracked particles
; that are linked in time

; init_t and final_t specify the start stack and end stack
; respectively

; dz is the interslice separation from imaging

; plane specifies which plane to pic in the z direction
; The bottommost plane is plane=1


;Outputs:
; S is the normalized correlation function.
```

```
;Melaku Muluneh, 05/26/08

ndat=n_elements(in_plane(*,0))
;min_z = min(tr(2,*))
;z = min_z + dz*plane

;w0=where(tr(2,*) ge z-(dz/2) and tr(2,*) le z+(dz/2), nplane)
; pics particles in the quasi 2D

;in_plane=tr(*,w0)


;w1=where(in_plane(ndat-2,*) eq init_t,ninit_t)

;w2=where(in_plane(ndat-2,*) eq final_t,nfinal_t)


binsize=0.2

;nbin = floor(max_dr/binsize)+1

S = dblarr(3,nbin+1)

if ninit_t gt nfinal_t then begin
disp=fltarr(3,ninit_t)
endif else begin
disp=fltarr(3,nfinal_t)
endelse


; Compute the displacement for each particle for the given time jump


for i=0L, ninit_t-1L do begin


    for j=0L, nfinal_t-1L do begin
        ;CON1 = abs(in_plane(2,w1(i))-in_plane(2,w2(j)))
        CON2 = in_plane(ndat-1,w1(i)) - in_plane(ndat-1,w2(j))
        ;pics a position of same ID, i.e. same particle

        if  CON2 eq 0 then begin

         disp(0:1,i) = in_plane(0:1,w2(j))-in_plane(0:1,w1(i))
         disp(2,i) = disp(0,i)^2+disp(1,i)^2 ;+disp(2,i)^2

       endif
    endfor
endfor
```

```
;write_text, disp,'disp.txt'

w3 = where(disp(2,*) ne 0L, ngood)
;eq to 0 can happen if init_t doesn't have a corresponding final_t
; or vice versa.
if ngood eq 0 then begin
    return, S
endif

;disp = disp(*,w3)

if ngood ne 0 then begin

corr=dblarr(4,ninit_t*nfinal_t)

count = 0ull

; Compute the correlation for each pair

for l=0, ninit_t-1 do begin
    for k = 0, nfinal_t-1 do begin
    CON = in_plane(ndat-1,w1(l)) - in_plane(ndat-1,w2(k))

    if CON ne 0 then begin      ;avoid self-correlation
            dot = disp(0,l)*disp(0,k) + disp(1,l)*disp(1,k)
            ;+ disp(2,l)*disp(2,k)
            distsq = sqrt((in_plane(0,w1(l))-in_plane(0,w2(k)))^2 +
            (in_plane(1,w1(l))-in_plane(1,w2(k)))^2)
            ;+ (in_plane(2,w1(l))-in_plane(2,w2(k)))^2)

       corr[0:3,count]=[w1[l],w2[k],dot,distsq]
       count++
     endif
    endfor
endfor



;w3 = where(disp(3,*) ne 0L, ngood)
;disp = disp(*,w3)

w4=where(corr(0,*) ne 0,n)
corr=corr(*,w4)

;write_text,corr,'corr.txt'

avg_dispsq = mean(disp(2,*))

;max_dr=max(tr(2,*),min=min_dr)
```

```
; Bin the data into boxes of size binsize.

for m=0L,nbin do begin
    w5 = where(corr(3,*) ge m*binsize and corr(3,*) lt (m+1)*binsize,nn)

    if nn ne 0 then begin
    ;check for the case where no value exists in the range
        mean_dot = mean(corr(2,w5))/avg_dispsq
        S[0:2,m] = [m*binsize,mean_dot,nn]
    endif

    if nn eq 0 then begin
       S[0,m] = m*binsize
    endif

endfor

;hist = Histogram(corr(3,*),binsize=0.5)

return, S

endif
end
```

To calculate the nearest neighbors of particles....

```
function NNE,tr,r,t,dz,plane

;Finds the indices of nearest neigbours within a given
;radius in the same plane
;Tr is pretracked particle positions
;r is the shell radius for nearest neigbhour calculation
;t is the stack number to pick from the pretracked data
;dz is the interslice separation within a stack
;plane is the slice number counting from bottom of the image

;Melaku Muluneh 05/16/08

w0 = where(tr[0,*] eq t, npos);
pos=tr[1:3,w0]
R = r^2
k=0ULL
rr=0


min_z = min(pos[2,*])
```

```
z = min_z + dz*plane

w1=where(pos[2,*] ge z-dz and pos[2,*] le z+dz, nplane)

in_plane = pos[*,w1]

nn = intarr(2,6*nplane)

for i=0,nplane-1 do begin
     for j = i+1, nplane-1 do begin
             rr = (in_plane[0,i] - in_plane[0,j])^2 +
             (in_plane[1,i] - in_plane[1,j])^2 +
             (in_plane[2,i] - in_plane[2,j])^2
              if rr lt R then begin
                   nn[0:1,k] = [w1[i],w1[j]]
                   k++
              endif
        endfor
endfor

w2 = where(nn[1,*] ne 0)
res = nn[*,w2]

return, res
end
```

To make movies from particle imaging velocimetry files...

```
pro pivmovie1,fname,fname1,disp,nplane,win

; creates a movie from PIV images.
; Melaku Muluneh 03/04/09


a=readtiffstack(fname);
b=[512,512]
for i=0,nplane-1 do begin

piv=epiv(a(*,*,0),a(*,*,i),disp,/nopoly,window=win);

pivplot,piv,charsize=2,spacing=5,scale=2,xrange=[150,350],
          yrange=[150,350],title='PIV';

im=tvrd(/ORDER)

write_tiff, fname1+'_'+'piv_0 to '+ STRTRIM(i,2)+ '.tiff',im
;mpegID = MPEG_OPEN(b)
```

```
;MPEG_PUT, mpegID, IMAGE=im, FRAME=i
;print,i
;MPEG_SAVE, mpegID, FILENAME='fname.mpg'
;MPEG_CLOSE, mpegID

endfor
end
```

To calculate correlations in 2d...

```
function dispcorr2d,tr,dt

max_dx=max(tr(0,*))
max_dy=max(tr(1,*))

max_r = sqrt(max_dx^2+max_dy^2)

binsize=0.2

nbin = floor(max_r/binsize)+1

corr_t = dblarr(3,nbin+1)
corr_z = dblarr(3,nbin+1)

;max_z=max(tr(2,*),min=min_z)

ndat=n_elements(tr(*,0))

max_t=fix(max(tr(ndat-2,*),min=min_t))
 ; min_z = min(tr(2,*))

  i_n=0

    for i=1,max_t do begin

       if i+dt le max_t then begin

        ;w0=where(tr(2,*) ge z-(dz*7) and tr(2,*) le z+(dz*7), nplane)
        ; pics particles in the quasi 2D

        ;quasi_plane=tr(*,w0)

        w_int=where(tr(ndat-2,*) eq i,nint)
```

```
        w_fin=where(tr(ndat-2,*) eq i+dt,nfin)

      if nint ne 0 and nfin ne 0 then begin

         b=dispcorr1(tr,max_r,w_int,w_fin,nint,nfin,nbin)

       if mean(b(2,*)) ne 0 then begin
       ;check to see if b is just the zero matrix or not. If so,
                                          ;don't increament.
         i_n++
         endif
          corr_t=corr_t+b
      endif
     endif
    endfor
    if i_n ne 0 then begin  ;Make sure there's correlations
    corr_t(1,*)=corr_t(1,*)/i_n
    corr_z(0,*)=b(0,*)
    endif
        corr_z(1,*)=corr_t(1,*)
        corr_z(2,*)=corr_t(2,*)
;endfor
;corr_z(1,*) = corr_z(1,*)/slices
return, corr_z
end
```

Appendix B

Rendering script

The following is an example aqsis script used to render the data.

```
FrameBegin 1
Display "Series26_FromTop2.tif" "file" "rgba"
Format 700 700 1
ShadingRate 1
Projection "perspective" "fov" [30]
FrameAspectRatio 1.5
Clipping 0.1 300


#Default distant headlight
LightSource "ambientlight" 2 "intensity" 1

# Camera transformation
Translate 3 2 15

WorldBegin


Rotate 80 0 0 0
Rotate 180 0 0 1.0
Scale 0.5 0.5 0.5
AttributeBegin


    Color [1.0 0.2 0.0]
    Opacity [0.5 0.5 0.5]
    Surface "plastic" "color specularcolor" [ 1 1 1 ]
        "float Ka" [ 0.7 ] "float Kd" [ 0.7 ]
        "float Ks" [ 0.900 ] "float roughness" [ 0.1 ]
TransformBegin
```

```
Translate 0.13525 5.74872 0.65570
Sphere 0.45 −0.45 0.45 360
TransformEnd
TransformBegin
Translate 0.14252 1.77732 2.57667
Sphere 0.45 −0.45 0.45 360
TransformEnd
TransformBegin
Translate 0.18882 13.97127 1.91778
Sphere 0.45 −0.45 0.45 360
TransformEnd
TransformBegin
Translate 0.20014 2.61831 2.87582
Sphere 0.45 −0.45 0.45 360
TransformEnd
.
.
.

{A lot more points go here}
.
.
.
TransformBegin
Translate 14.51695 4.96335 0.54313
Sphere 0.45 −0.45 0.45 360
TransformEnd
TransformBegin
Translate 14.54479 3.06350 0.41717
Sphere 0.45 −0.45 0.45 360
TransformEnd


AttributeEnd
AttributeBegin

Color [0.0 0.0 1.0]


    Opacity [1.0 1.0 1.0]
    Surface "plastic" "color specularcolor" [ 1 1 1 ]
        "float Ka" [ 0.7 ] "float Kd" [ 0.7 ]
        "float Ks" [ 0.900 ] "float roughness" [ 0.1 ]

TransformBegin
Translate 10.019 7.935 0.451
ReadArchive "cube.RIB"
TransformEnd
TransformBegin
Translate 9.906 9.326 0.473
```

```
ReadArchive "cube.RIB"
TransformEnd
.
.
.

{A lot more points go here}
.
.
.
TransformBegin
Translate 9.343 7.232 0.634
ReadArchive "cube.RIB"
TransformEnd
TransformBegin
Translate 7.106 4.948 0.638
ReadArchive "cube.RIB"
TransformEnd

AttributeEnd



AttributeBegin

Color [1 0.0 0.0]


    Opacity [1 1 1]
    Surface "plastic" "color specularcolor" [ 1 1 1 ]
        "float Ka" [ 0.7 ] "float Kd" [ 0.7 ]
        "float Ks" [ 0.900 ] "float roughness" [ 0.1 ]
TransformBegin
Translate 10.565 9.520 1.389
ReadArchive "cube.RIB"
TransformEnd
TransformBegin
Translate 11.960 8.246 1.393
ReadArchive "cube.RIB"
TransformEnd
.
.
.
{A lot more points go here}
.
.
.
TransformBegin
Translate 10.279 10.767 1.762
ReadArchive "cube.RIB"
```

```
TransformEnd
TransformBegin
Translate 11.226 8.929 1.762
ReadArchive "cube.RIB"
TransformEnd
TransformBegin
Translate 10.681 6.834 1.762
ReadArchive "cube.RIB"
TransformEnd

AttributeEnd



AttributeBegin


Color [0 1 0]


    Opacity [1 1 1]
    Surface "plastic" "color specularcolor" [ 1 1 1 ]
        "float Ka" [ 0.7 ] "float Kd" [ 0.7 ]
        "float Ks" [ 0.900 ] "float roughness" [ 0.1 ]
TransformBegin
Translate 5.166 5.222 2.233
ReadArchive "cube.RIB"
TransformEnd
TransformBegin
Translate 10.699 7.657 2.254
ReadArchive "cube.RIB"
TransformEnd
.
.
.

TransformBegin
Translate 6.107 5.245 2.896
ReadArchive "cube.RIB"
TransformEnd

AttributeEnd



AttributeBegin

Color [2.0 0.5 1.0]
```

```
    Opacity [0.5 0.5 0.5]
    Surface "plastic" "color specularcolor" [ 1 1 1 ]
        "float Ka" [ 0.7 ] "float Kd" [ 0.7 ]
        "float Ks" [ 0.900 ] "float roughness" [ 0.1 ]
TransformBegin
Translate 12.072 9.391 3.145
ReadArchive "cube.RIB"
TransformEnd
TransformBegin
Translate 9.571 10.200 3.172
ReadArchive "cube.RIB"
TransformEnd
.
.
.
TransformBegin
Translate 9.361 8.173 3.346
ReadArchive "cube.RIB"
TransformEnd
TransformBegin
Translate 8.608 8.636 3.354
ReadArchive "cube.RIB"
TransformEnd


AttributeEnd


#If one needs bouding box
#AttributeBegin

#Color [0.5 0.5 0.5]
#Translate 7 1 4
#Rotate 90 0.0 1.0 0.0

#Curves "linear" [2] "nonperiodic" "P"
    [−6 −6 −6 −6 −6 6] "constantwidth" [0.05]
#Curves "linear" [2] "nonperiodic" "P"
    [−6 −6 −6 6 −6 −6] "constantwidth" [0.05]
#Curves "linear" [2] "nonperiodic" "P"
    [6 6 6 −6 6 6] "constantwidth" [0.05]
#Curves "linear" [2] "nonperiodic" "P"
    [6 6 6 6 −6 6] "constantwidth" [0.05]
#Curves "linear" [2] "nonperiodic" "P"
    [6 6 6 6 6 −6] "constantwidth" [0.05]
#Curves "linear" [2] "nonperiodic" "P"
    [6 −6 6 −6 −6 6] "constantwidth" [0.05]
#Curves "linear" [2] "nonperiodic" "P"
    [6 −6 6 6 −6 −6] "constantwidth" [0.05]
#Curves "linear" [2] "nonperiodic" "P"
```

```
    [−6 6 6 −6 −6 6] "constantwidth" [0.05]
#Curves "linear" [2] "nonperiodic" "P"
    [6 6 −6 6 −6 −6] "constantwidth" [0.05]
#Curves "linear" [2] "nonperiodic" "P"
    [6 6 −6 −6 6 −6] "constantwidth" [0.05]
#Curves "linear" [2] "nonperiodic" "P"
    [−6 −6 −6 −6 6 −6] "constantwidth" [0.05]
#Curves "linear" [2] "nonperiodic" "P"
    [−6 6 6 −6 6 −6] "constantwidth" [0.05]
#AttributeEnd

WorldEnd

FrameEnd
```

A cube is defined separately.

```
#generates the faces of the cube and puts them together.

PointsPolygons
[4 4 4 4 4 4]
[2 3 1 0 4 5 3 2 6 7 5 4 0 1 7 6 3 5 7 1 4 2 0 6]
"P" [
−0.35 −0.35 0.35
0.35 −0.35 0.35
−0.35 0.35 0.35
0.35 0.35 0.35
−0.35 0.35 −0.35
0.35 0.35 −0.35
−0.35 −0.35 −0.35
0.35 −0.35 −0.35
]
```